

710425

3109

31127

TR 3110

Coal Fires in Northwest China

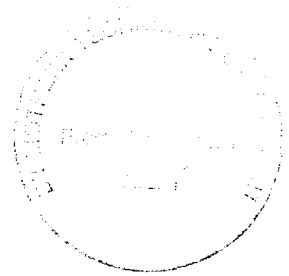
Detection, Monitoring, and Prediction Using Remote Sensing Data

PROEFSCHRIFT

ter verkrijging van de graad van doctor
aan de Technische Universiteit Delft,
op gezag van de Rector Magnificus Prof. ir. K. F. Wakker,
in het openbaar te verdedigen ten overstaan van een commissie,
door het College voor Promoties aangewezen,
op maandag 6 april 1998 te 10:30 uur

door

ZHANG, Xiangmin
Master of Science in Geology
Geboren te Yuanshi, Hebei Province, China



Dit proefschrift is goedgekeurd door de promotor:

Prof. dr. S. B. Kroonenberg

Toegevoegd promotor: Prof. dr. J. L. van Genderen (ITC)

Samenstelling promotiecommissie:

Rector Magnificus, voorzitter

Prof. dr. S. B. Kroonenberg

Prof. dr. J. L. van Genderen

Prof. dr. M. A. Reuter

Prof. dr. A. P. Cracknell

Prof. dr. A. G. Fabbri

Prof. dr. J. Bodechtel

Prof. dr. R. A. P. Klees

Technische Universiteit Delft, Promotor

ITC, Enschede, toegevoegd promotor

Technische Universiteit Delft

University of Dundee, United Kingdom

ITC, Enschede

University of Munich, Germany

Technische Universiteit Delft

ISBN 90-6164-144-6

ITC Publication Number 58

Dedication

**to my parents
and to Junying and Wenzhi**

ABSTRACT

Coal fires in China occur within a region that stretches over 5,000 km east-west and 750 km north-south. These fires cause an economic and environmental threat by making a significant contribution to the global CO₂ budget. The studies made in this thesis can be divided into two parts. Part one is based on field work and laboratory analysis that includes the dating of the paleo coal fires; part two concerns remote sensing applications for the active coal fires.

In part one it is shown that over 85% of the burnt rock recognized in the remote sensing imagery in NW China is of Pleistocene age. Several age groups of burnt rock have also been recognized: (1) Beigou burnt rocks, deeply weathered and unconformably overlain by a Pliocene-Early Quaternary alluvial fan, now deeply dissected and situated over 200 m above the Toutunhe River; (2) Middle Pleistocene Qianshuihe-Louzhuangzi burnt rocks, situated above the highest (90 m) terraces of the Toutunhe River; (3) Late Pleistocene Gangou burnt rocks, which are unconformably overlain by gravel of the 70 m terrace of the Toutunhe River and incorporate burnt terrace gravel, which cannot be older than the 90 m level; (4) Holocene Zaoyuan paleo coal fires baking the gravels of the lowest terrace (younger than group 3); and (5) active coal fires and related burnt rocks. These data indicate that coal fires existed one million years ago.

Part two studies the active coal fires by means of thermal infrared remote sensing data from both airborne and satellite borne sensors.

The physical basis of thermal infrared remote sensing for the detection and measurement of coal fires is addressed in order to understand: 1) the characteristics of the thermal infrared data in respect to the spatial, spectral, and radiometric resolution for the detection of coal fires; 2) the methods for surface temperature retrieval and related problems; and 3) other important aspects of the data such as the season and time of data acquisition.

In mountainous areas uneven solar heating is the main source of confusion when detecting coal-fire-induced thermal anomalies by the use of daytime thermal infrared remote sensing data. The solar heating has been modeled using a Digital Elevation Model (DEM), together with the azimuth and

altitude angle of the sun at the time when the remote sensing data are collected. This simulated image is used for the thermal remote sensing data to suppress the thermal anomalies of slopes facing the sun and to enhance the coal fire areas.

On the basis of the method of converting the radiance from thermal remote sensing data into radiant temperature, a quantitative method has been developed to evaluate the capability of Landsat TM thermal data for the detection of sub-pixel coal fires with respect to their sizes and temperatures. This method can also be used for the temperature estimation of coal fire areas of sub-pixel size, with the knowledge of the fire size being provided by airborne thermal scanner data or field survey data.

Night-time airborne thermal scanner imagery acquired in the 8-12.5 μm wavelength region of the electromagnetic spectrum clearly shows detailed low-amplitude thermal anomalies caused by underground coal fires, that are saturated at medium (20 $^{\circ}\text{C}$ above the background) and high-amplitude (above 120 $^{\circ}\text{C}$) thermal anomaly areas. Daytime thermal infrared data acquired in the 3-5 μm wavelength region provide information about spectrally reflected solar radiation and radiation from high-amplitude surface thermal anomalies of the underground coal fires. To reduce the effects of spectrally reflected solar radiation, the data acquired in the 0.61-0.69 μm wavelength region were used to subtract the 3-5 μm data. This new image shows the enhanced high-amplitude thermal anomalies of the underground coal fires. In the daytime 8-12.5 μm image, thermal anomalies represent not only underground coal fires, but also solar heating of non-burning coal seams and black shale with higher emissivity. Integrated information of the thermal anomalies of the underground coal fires were displayed in a single image. On the basis of the spatial patterns of the thermal anomalies of the underground coal fires, spreading models were set up through field observations, thus the spreading direction of underground coal fires are inferred. Comparing the daytime and night-time 8-12.5 μm data, the solar heated coal seams were detected as areas with a high risk probability of coal fires occurring in the future because the temperatures measured in the field were close to the critical point of the spontaneous combustion of coal.

Based on multi-sensor data fusion techniques, a hierarchical methodology for the detection and monitoring of coal fires has been developed. The low

spatial resolution satellite thermal infrared data such as NOAA-AVHRR (1.1km), ERS-1-ATRS (1.1 km), and RESURS-1 data (600 m) are used to detect possible fire areas. To see if these areas are actually coal fire areas, the higher spatial resolution satellite data from Landsat-5 TM (120 m) are used. In the near future, data from Landsat-7 ETM+ (60m) and EOS-AM1 ASTER (90 m) (multi-spectral thermal data) will also be used. The next step is to design a flight campaign to obtain the airborne remote sensing data. The methodology is based on fusing a variety of satellite-based image types (optical, thermal, microwave) together with airborne data (optical and thermal infrared) with ancillary data sources such as geological and topographic maps, etc. Three data fusion techniques, namely the pixel-based, feature-based, and decision-based fusion have been used. The fusion results of the remote sensing data are also presented.

SAMENVATTING

Steenkoolbranden in China komen voor in een groot gebied van 5000 km breed (E-W) en 750 km lang (N-S). Zij vormen niet alleen een economische schadepost maar ook een gevaar voor het milieu, vanwege hun niet onaanzienlijke aandeel in de mondiale CO₂ uitstoot. In dit proefschrift worden twee aspecten van de steenkoolbranden in China behandeld. In het eerste deel komen de herkenning en de datering van vroegere (fossiele) steenkoolbranden aan de orde, op grond van veldgegevens en laboratoriumonderzoek zoals paleomagnetische analyse. Het tweede deel van het proefschrift behandelt de toepassing van remote sensing technieken voor het opsporen en volgen van actieve steenkoolbranden en het voorspellen van nieuwe brandhaarden.

In het stroomgebied van de Toutunhe rivier in NW China kunnen gesteenten die tengevolge van koolbranden zijn verbrand in remote sensingbeelden spectraal worden herkend. Het overgrote deel daarvan (85%) betreft echter geen actieve branden, maar is van Pleistocene ouderdom. Er zijn verschillende leeftijdsgroepen herkend op grond van de hoogteligging en paleomagnetisch onderzoek: (1) de Beigou groep van verbrande gesteenten zijn diep verweerd en discordant bedekt door Pliocene tot vroeg-Kwartaire puinwaaierafzettingen, die zelf weer diep versneden zijn en zich nu 200m boven de Toutunhe rivier bevinden; (2) de Midden-Pleistocene Qianshuihe-Louzhuangzi verbrande gesteenten bevinden zich boven de hoogste terrassen (90 m) van de Toutunhe rivier; (3) de Laat-Pleistocene Gangou verbrande gesteenten worden discordant bedekt door een laag grind van het 70 m terras van de Toutunhe rivier, maar zijn vermengd met verbrand terrasgrind, dat niet ouder kan zijn dan dat van het 90 m niveau; (4) de Holocene Zaoyuan verbrande gesteenten bevinden zich in het laagterras van de Toutunhe; (5) Recente verbrande gesteenten gerelateerd aan actieve steenkoolbranden. Deze gegevens wijzen erop dat spontane steenkoolbranden al sinds meer dan een miljoen jaar geleden optreden.

Het tweede deel van het proefschrift behandelt het onderzoek naar actieve steenkoolbranden met behulp van thermisch infrarood remote sensing gegevens verkregen door sensoren aan boord van vliegtuigen en satellieten.

De fysische grondslagen van de thermisch-infrarood remote sensing voor het detecteren en meten van steenkoolbranden worden uiteengezet met als doel: 1) het begrijpen van de kenmerken van de thermische infrarood gegevens met betrekking tot de ruimtelijke, spectrale en radiometrische resolutie voor detectie van steenkoolbranden; 2) het begrijpen van de methoden voor het bepalen van oppervlakte temperatuur en verwante problemen; 3) andere belangrijke aspecten van de gegevens zoals het seizoen en de tijd van gegevensverwerving.

In een bergachtige omgeving is de ongelijkmatige verwarming door de zon de belangrijkste complicatie bij het detecteren van door steenkoolbranden veroorzaakte thermische anomalieën in overdag verkregen thermisch infrarood remote sensing data. De verwarming door de zon werd gemodelleerd met behulp van een Digitaal Terrein Model (Digital Elevation Model, DEM), samen met het azimuth en de hoogte van de hoek van de zon op het tijdstip van opname van de remote sensing gegevens. Het gesimuleerde beeld werd vervolgens gebruikt om de thermische anomalieën op de zonbeschenen hellingen in de thermisch remote sensing gegevens te onderdrukken en om de gebieden met steenkoolbranden naar voren te halen.

Door middel van het omzetten van de radiantie van thermische remote sensing data naar stralingstemperatuur, is een kwantitatieve methode ontwikkeld om na te gaan hoe de omvang en de temperatuur van sub-pixel steenkoolbranden in Landsat TM thermische data kunnen worden gedetecteerd. Deze methode kan ook gebruikt worden voor het schatten van de temperatuur van steenkoolbranden van sub-pixel grootte, als de omvang van de brand bekend is uit airborne thermische scanner gegevens of uit veldonderzoek.

's Nachts gevlogen thermische scanneropnamen in het 8 -12.5 μm golflengtegebied van het electromagnetisch spectrum laten duidelijk gedetailleerde laag-amplitude thermische anomalieën zien, veroorzaakt door ondergrondse steenkoolbranden. In middel-amplitude (20°C boven de achtergrond) en hoog-amplitude (boven 120° C) thermisch anomale gebieden zijn deze anomalieën verzadigd. Overdag verkregen infraroodopnamen in het 3-5 μm golflengtegebied geven zowel informatie over de spectraal gereflecteerde zonnestraling als over de straling afkomstig van hoge-intensiteit thermische oppervlakteanomalieën van de

steenkoolbranden. Om de effecten van de spectraal gereflecteerde zonnestraling te reduceren zijn de gegevens in het 0.61-0.69 μm golflengtegebied afgetrokken van de 3-5 μm data. Het aldus verkregen beeld laat de hoog-amplitude thermische anomalieën van de ondergrondse steenkool branden versterkt zien. Thermische anomalieën in de 8-12.5 μm dagopname geven niet alleen ondergrondse steenkoolbranden aan, maar ook niet-brandende, maar door de zon sterk verhitte dunne steenkoollagen en zwarte schalies met hogere emissiviteit. De geïntegreerde informatie van de thermische anomalieën van de ondergrondse steenkoolbranden is uiteindelijk gecombineerd in één beeld.

Door de ruimtelijke patronen van de thermische anomalieën te combineren met de in het veld verkregen informatie over de verspreidingsmodellen van de ondergrondse steenkoolbranden, kon de voortplantingsrichting van de ondergrondse steenkoolbranden worden afgeleid. Door de overdag en 's nachts verkregen 8-12.5 μm gegevens met elkaar te vergelijken konden de door de zon verhitte koollagen en schalies worden aangemerkt als gebieden met een verhoogd risico op steenkoolbranden in de toekomst, omdat de in het veld gemeten temperaturen daarvan dichtbij de kritische temperatuur voor het spontaan ontbranden van steenkool liggen.

Gebaseerd op multi-sensor data fusie technieken, is een hiërarchische methode voor detectie en monitoren van de steenkool branden ontwikkeld. De laag ruimtelijke satelliet infra rood data, zoals NOAA-AVHRR (1.1 Km), ERS-1-ATRS (1.1 Km) en RESURS-1 data (600 m) zijn gebruikt om mogelijke steenkool branden te ontdekken. Om te zien of deze gebieden werkelijk steenkool branden herbergen de hogere ruimtelijke resolutie satelliet data van de Landsat-5 TM (120 m) en in de nabije toekomst de Landsat-7 ETM+ (60 m) en de EOS-AM1 ASTER multi spectraal thermische data (90 m) zijn gebruikt. De volgende stap is het opzetten van een vlucht schema voor het verkrijgen van de luchtopnamen. De methodologie is gebaseerd op het fuseren van verschillende typen van satelliet opnamen (optisch, thermisch en microgolven) samen met luchtopnamen (optisch en infra rood) en andere informatie bronnen zoals geologische en topografische kaarten, enz. Drie data fusie technieken, nl pixel-based, feature-based en decision based fusie zijn gebruikt en de resultaten van de remote sensing fusie worden gepresenteerd.

那些珍贵的煤碳资源
并不是我们继承祖先的遗产
而是我们借用子孙的财富

摘要

中国北方煤田煤层自燃是中国五大地质灾害之一。煤层自燃不仅造成巨大的煤碳资源损失,同时也造成严重的区域性和全球性环境问题。本论文的研究包括二部分。第一部分研究中国新疆头屯河地区第四纪古烧变岩时代测定和燃烧规律。第二部分研究使用热红外遥感技术对正在燃烧区的探测、测量、监测和预测。研究内容大部分已发表在国际杂志或国际会议论文集上。

论文共分七章,第一章为总序论,介绍本文研究的目的、方法及前人工作的文献研究。

论文的第一部分即第二章,主要涉及古火区的研究。根据彩红外航空遥感图像解译、野外地质调查以及实验室古地磁测量,中国新疆头屯河地区烧变岩可以划分为五个时代: 1) 北沟烧变岩,现分布于高出头屯河200米处,该烧变岩被上新世-早更新世洪积扇沉积覆盖; 2) 浅水河-楼庄子烧变岩,分布于高出头屯河最高阶地以上,部分为分布于头屯河最高阶地上的中更新沉积所覆盖; 3) 干沟-六工烧变岩,其上有两层阶地沉积覆盖,下层沉积被古煤火烘烤,上层形成头屯河70米阶地的晚更新世沉积层未被烘烤; 4) 枣园烧变岩,该烧变岩形成于全新世,覆盖于其上的第一级与第二级阶地沉积均被烘烤; 5) 克拉扎烧变岩,为现代烧变岩并与克拉扎活火区相关。该研究证明此区烧变岩85%形成于更新世。

第二部分即第三章至第七章为研究重点,研究利用卫星及航空热红外遥感数据,采用地表日照升温模型、热红外次像元计算分析方法及遥感数据融合技术,对活火区进行探测、测量、监测及预测。

其中的第三章介绍热红外遥感的物理基础。侧重热红外传感器的的工作波段,遥感数据的空间分辨率与煤火探测的关

系, 利用热红外遥感数据计算地表温度的原理与方法。同时分析了卫星热红外数据获取的时间及季节性影响与煤火探测的关系。

在地表起伏较大的煤火区, 利用日航陆地卫星热红外数据对煤火探测的最大困难是由日照引起的地面不均匀热增温。为此, 论文的第四章研究利用数字高程模型, 卫星过境时太阳高度角和方位角等参数对地表日照升温进行数学模拟。通过比较模拟的日照热增温图像和日航陆地卫星热红外数据, 由地形引起的不均匀地面热增温得到了纠正, 因而突出了火区信息。

由于大部分火点的空间范围不及陆地卫星热红外数据的地表分辨率单元的大小($120\text{米} \times 120\text{米}$), 所以对煤火的探测必须考虑卫星数据对次象元大小热源的探测能力。第五章研究陆地卫星热红外数据对次象元煤火探测能力的物理原理和数学方法, 并给出了陆地卫星热红外数据对煤火探测能力的图表结果。

论文的第六章研究利用多时相航空遥感数据, 采用遥感数据融合技术探测不同强度的煤火火源。在分析经过融合产生的热图像上热异常空间特征的基础上, 指出了煤火的扩展方向。结合日航、夜航热红外扫描 $8-12.5$ 微米数据, 预测了将来有可能发火的煤层露头区。本章使用了四种不同时相、不同波段的航空数据: 1) 夜航热红外扫描 $8-12.5$ 微米数据; 2) 日航热红外扫描 $8-12.5$ 微米数据; 3) 日航热红外扫描 $3-5$ 微米数据; 4) 日航可见光 $0.61-0.69$ 微米数据。夜航热红外扫描 $8-12.5$ 微米数据可以最大限度地探测低温热异常区。日航热红外扫描 $8-12.5$ 微米数据被用来探测中温热异常区及由太阳照射而急剧升温的煤层露头区。据热红外辐射规律, 日航热红外扫描 $3-5$ 微米数据可以用来探测煤火高温热异常, 但是这些异常常常被地表的高反射区干扰, 所以日航可见光 $0.61-0.69$ 微米数据被用来去除这些影响。利用数据融合技术, 这些不同强度的煤火区被结合在同一影像上。从小而强的热异常到大而低的热异常通常指示地下煤火的扩展方向。一些从日航热红外扫描 $8-12.5$ 微米数据上提取的热异常并无对应的夜航热异常, 这些地区是由于太阳照射而急剧升温的煤层露头区。野外地表测温证明这些地区

煤层温度已非常接近煤层自燃的临界值,因此也是预测的未来煤火发生区。

最后,第七章讨论基于遥感数据融合技术,利用低分辨率卫星数据,高分辨率卫星数据及航空数据的三层煤火监测系统流程。给出了象元融合、影像特征融合及信息决策融合技术用于煤火探测的方法和结果。对即将发射的新一代陆地卫星(Landsat-7)增强专题制图仪(ETM+)数据,地球观测卫星(EOS)上先进航天热辐射仪(ASTER)数据对煤火监测的应用前景进行了评价。

ACKNOWLEDGMENTS

I would like to thank all the persons who contributed to this thesis in one way or the other. Without their help this thesis could not have been realized.

First of all I would like to thank Prof. Dr. Salomon B. Kroonenberg for his willingness to act as my promoter. His constant enthusiasm and confidence was a very important factor in helping me to complete this research. His guidance over the last three and half years was most appreciated by his leading me in the right direction. In addition, the joint field work with him in 1995 was a most fruitful and unforgettable experience. His "right to the point" comments were most beneficial to my studies. Secondly I would like to thank Prof. Dr. John L. van Genderen of the ITC for having given me the opportunity to study for my Ph.D under his supervision in the Netherlands. His constructive criticism was most useful to my research.

Thanks are also due to Prof. Guan Haiyan, the former deputy-director of the Aerophotogrammetry & Remote Sensing Bureau of China Coal (ARSC) for his constant support of my research and the organization of the field work. His encouragement and help inspired me to carry out and complete the research.

Three field campaigns were carried out during 1994, 1995, and 1996, and Dr. Tan Yongjie's help is highly appreciated for the enthusiastic organization of each of the field work periods. He always found the way to overcome the difficulties we met in the field. Mr. Kang Gaofeng, Mr. Lei Xuewu, Mr. Wu Junhu, Ms. Zhang Xiaoxia, and Ms. Yang Hong are also thanked for their help during the field work campaigns of 1994 and 1995.

Mr. Zhang Ting'an is thanked for permits assigning for the collection of the relevant geological and remote sensing data in ARSC. Mr. Zhang Jianzhong is thanked for the help during the field work of 1995 to collect the Quaternary geological data from the Geographical Institute of Xinjiang.

Dr. B. Koopmans is thanked for his contribution to the field work of 1994 and the valuable discussions on the topic of my research in its early stage.

Mr. Wan Yuqing, Mr. Mao Yaobao, Mr. Kang Gaofeng, Mr. Peng Wenxiang, and Mr. Ma Heping, the visiting scientists at ITC from ARSC who were all working on the "Environmental Monitoring of Spontaneous Combustion in the North China Coalfields" project, are thanked for the valuable discussions and help on many aspects of the research.

Craig Cassells and Rudi Gens, my Ph.D colleagues, are thanked for the stimulating discussions and the friendship shared through the years. I would like to thank Dr. Zoltan Vekerdy, Dr. Anupma Prakash and Mr. Guan Feng, who are working on the project of Development and Implementation of a Coal Fire Monitoring and Fighting System in China, for their help on the field data processing, ILWIS, and the discussions on coal fires. Mr. Boudewijn van Veen and Mr. Helios W. Jellema are thanked for the first draft translation of the Dutch Summary. I also would like to thank Dr. Elizabeth Kusters for her help and support. I am grateful to the secretariat of the Department of Earth Resources Surveys for their help.

Many persons reviewed parts of my thesis. Their critical comments and advice are highly appreciated: Dr. Paul van Dijk (Chapter 1), Dr. Karl-Heinz Wolf (Abstract, Chapters 1 & 2), Prof. A. P. Cracknell (Chapter 5) and Dr. A. Prakash (Chapter 5).

The paleomagnetism analysis was carried out at Paleomagnetic Laboratory "Fort Hoofddijk" of Utecht University. I would like to thank Mr. Ton van Hoof for hosting me and processing the samples.

Dr. Hogné Jungner of Helsinki University is thanked for his cooperation in trying to date the burnt rocks with TL. Ir. Chr. Maugenest is thanked for his literature research on *Palaeoloxodon*.

This research is part of a project funded by the European Commission under Research Contract No. CII*-CT93-0008(DG XII), by ITC and by ARSC. Their financial supports are gratefully acknowledged.

Finally I would like to express my deep gratitude to my wife Junying and to my parents for their patience and moral support.

LIST OF FIGURES

- Figure 1-1 Location of coal fires in North China. The box marked A is the place where the three test areas mentioned in this thesis are located. Box B is the Ningxia test area. Source: KYK, No. 8 page 29, 1995.
- Figure 2-1 Geological map of study area with distribution of burnt rocks and active coal fires.
- Figure 2-2 Distribution of burnt rocks and river terraces.
- Figure 2-3 Cross-section of Toutunhe River terraces and burnt rock occurrences.
- Figure 2-4 Qianshuihe burnt rock profile.
- Figure 2-5 Gangou burnt rock profile.
- Figure 2-6 Geomagnetic polarity time scale of the late Pliocene to Holocene according to Lourens et al. (1996). Black (white) blocks denote periods with normal (reversed) directions of the geomagnetic field. J: Jaramillo; CM: Cobb Mountain; O: Olduvai; R: Reunion. Vertical lines represent the age estimates based on stratigraphy.
- Figure 2-7 Examples of alternating field demagnetisation diagrams for samples of the burnt rock groups from the Xinjiang region, showing their normal polarity. Closed (open) symbols represent the projection of the NRM vector end-points on the horizontal (vertical) plane, respectively; values represent alternating fields in mT. Int = initial NRM intensity.
- Figure 2-8 Example showing a typical thermomagnetic analysis of burnt rocks from the Gangou group, clearly indicating the presence of metallic iron ($T_c = 770^\circ\text{C}$). Minor inflection points around 440°C , 580°C and 640°C suggest the presence of a magnetic spinel phase, magnetite, and maghemite, respectively.
- Figure 2-9 Proportion of the areas covered by fossil burnt rocks and active coal fires, as derived from remote sensing imagery.
- Figure 3-1 Atmospheric absorption of the wavelength range 0 to $15\ \mu\text{m}$. Note the presence of atmospheric windows in the thermal regions 3 to $5\ \mu\text{m}$ and 8-14 μm .

List of Figures

- Figure 3-2 Spectral distribution of energy radiation from blackbodies of various temperatures.
- Figure 3-3 Field temperature measurement at 2:00 pm August 17, 1995 of coal fire 143a along dip direction.
- Figure 3-4 Field temperature measurement at 5:30 am August 22, 1995 along road near Sidaogou above underground part of coal fire 143b.
- Figure 3-5 Diurnal temperature curves of typical objects in coal fire area.
- Figure 3-6 Surface coal fires recognized from Landsat-TM band 7 image.
- Figure 3-7 Surface coal fires recognized from Landsat-TM band 5 image.
-
- Figure 4-1 The reflectance of the main rocks in the test area.
- Figure 4-2 The surrounding pixels of pixel d.
- Figure 4-3 Digital elevation model (DEM) of area of the Kelazha anticline. The brightness indicates the elevation.
- Figure 4-4 Three-dimension topography perspective view of Kelazha area from the Southeast direction.
- Figure 4-5 Geological map of Kelazha area.
- Figure 4-6 The simulated solar heating image. The brightness of the image represents the incident radiation from the sun with respect to the azimuth and altitude angles and the topography.
- Figure 4-7 Geometrically corrected Landsat-TM image acquired on September 14, 1994, which covers the same areas as Figure 4-5 and Figure 4-6.
- Figure 4-8 The resultant image of subtracting the simulated one from Landsat-TM band 6. Note the coal fire areas have been enhanced.
- Figure 4-9 The geometrically corrected airborne night time thermal infrared image scanned on July 30, 1992, which was merged from two flight lines. The white spots on the image are the fires which were proved by the field work.
- Figure 4-10 Temperature curves of three main rocks from the test area.
- Figure 4-11 Two pixels and altitude values of their surrounding pixels. On (a) sunshine begins at 5:50 in the morning. On (b) sunshine begins at 8:35.
- Figure 4-12 Altitude and azimuth angle of the sun as a function of time.

- Figure 5-1 A coal fire partially occupies an area of IFOV of Landsat Thematic Mapper thermal channel.
- Figure 5-2 Portion and temperature of a coal fire which causes a minimum increase from background. The pixel values with and without a coal fire are assumed as 89 and 88 respectively. Every point in the solid line represents one combination of temperature and size of a coal fire partially occupying an IFOV area.
- Figure 5-3 Portion and temperature of coal fires which cause thermal anomalies (DN=91/ dash line, DN=94/ solid line) from the background (DN=88).
- Figure 5-4 Along-strike temperature survey of coal fire 137 (measured from 2:00 to 4:00 pm on 16 August 1995).
- Figure 6-1 Geological map of study area.
- Figure 6-2a Deepening model of coal fire.
- Figure 6-2b Deepening model of coal fire connected with underground mining tunnels.
- Figure 6-3 Lateral spreading model of coal fire.
- Figure 6-4 Field measurement of temperature profile of coal fires No. 141, 142 and 143 (measured at noon time of 17 August 1995).
- Figure 6-5a Mosaic of night-time thermal infrared scanner data of 8-12.5 μm (band 6). The white areas show the thermal anomalies caused by underground coal fires.
- Figure 6-5b Daytime thermal infrared scanner data of 8-12.5 μm (band 6). The white areas, which are smaller than those in Figure 6-5a are due to the higher setting of BB temperatures showing the thermal anomalies caused by underground coal fires.
- Figure 6-5c Daytime thermal infrared scanner data of 3-5 μm (band 5).
- Figure 6-5d Visible band image of 0.63-0.69 μm (band 3).
- Figure 6-5e Image generated by subtracting band 3 from band 5 with stretch processing.
- Figure 6-5f Integrated image of night-time and daytime band 6 data, band 5 and band 3 data.
- Figure 6-6 Scatter map of daytime band 3 and band 5 data.

-
- Figure 6-7 Sub-image of Figure 6-5f showing coal fires No. 141, 142, and 143, and the location of the profiles.
- Figure 6-8 Profile derived from night-time thermal image of Figure 6-2a. The thick line represents the DN values in the night-time thermal data. The thin line represents the field temperature measurement showed in Figure 6-4.
- Figure 6-9 Profiles derived from Figure 6-7. The thick line indicates the types of thermal anomalies. The thin line indicates the field temperature measurements shown in Figure 6-4.
- Figure 6-10 Field temperature measurement along coal seam and black shale in the north flank of the Kelazha anticline (measured at 14:00-16:00 August 16, 1995).
-
- Figure 7-1 Extract from a color infrared aerial photograph of an underground coal fire area, taken 7th August, 1992. Note the distinctive color of the burnt rock (yellowish orange color). Immediately adjacent to the central area of burnt rock an extensive area of land subsidence can be seen, indicated by the long parallel cracks in the land surface.
- Figure 7-2 Night-time thermal infrared image acquired by the Landsat-TM over the Kelazha anticline coal fire area in Xinjiang region on 07/04/1995. The image has been color coded and density sliced. The areas in bright red indicate the location of underground coal fires.
- Figure 7-3a Land subsidence occurring as a result of underground coal fires. The cracks are typically 20 centimeters to several meters wide, up to hundreds of meters long, and 10-20 meters in depth. The process is illustrated in figure 3b.
- Figure 7-3b Land subsidence caused by a sub-surface coal fire. Once the coal seam starts to combust where it outcrops, the coal layer slowly burns out, and the commonly 10-20 meter thick coal layer is reduced to a few centimeters of ash. The overburden collapses, causing extensive cracking and opening of fissures through which a fresh oxygen supply can reach the coal seam, which burns deeper and deeper with successive collapse of caprock and overburden.
- Figure 7-4 Pixel-based image fusion for detection of underground coal fires.

List of Figures

- Figure 7-5 Feature-based data fusion for detection of underground coal fires.
- Figure 7-6 Decision-based information fusion for detection of underground coal fires.
- Figure 7-7a Fused optical-thermal image of an underground coal fire in northwest China. Note that the image highlights the underground fire areas, whilst maintaining the excellent spatial structural details inherent in the optical data.
- Figure 7-7b Color composite SPOT band 3, 2, 1 with red, green, and blue.
- Figure 7-8a Feature-based image fusion for the detection of the coal fires with respect to the thermal anomalies from the thermal infrared image and the cracks from the color infrared photograph.
- Figure 7-8b Airborne thermal infrared image data draped over and co-registered with the DEM to create a 3-D perspective view. Such products assist in the study of underground coal fires as they show precisely the influence of slope, aspect, altitude, etc. on the distribution of the coal fires. This particular view is looking in an east-northeast direction.
- Figure 7-9 Decision-based image fusion for the detection of different intensive coal fires. The red areas represent the most intensive coal fire areas which are derived from the 3-5 μm data. The green areas represent the mid-amplitude coal fire areas derived from the daytime thermal infrared data of 8-12.5 μm . The white areas are the low-amplitude coal fires derived from the night time thermal infrared data of 8-12.5 μm data. The blue areas are the intensively solar heated areas.
- Figure 7-10 A three-level Multi-Sensor Data Fusion System to study location, size, depth etc. of underground coal fires for monitoring and management purposes.

LIST OF TABLES

- Table 1-1 Remote sensing data used for this study.
- Table 3-1 The calibration factors for the temperature calculation.
(*from Markham & Barker, 1986).
- Table 3-2 The pixel values in TM band 7, data received on November 8, 1995.
- Table 3-3 The pixel values in TM band 5, data received on November 8, 1995.
- Table 3-4 Temperature (°C) and areas(m²) of coal fires derived from band 7 and band 5 data using dual-band method.
- Table 7-1 Table showing the result and benefits of multi-sensor data fusion for the detection of underground coal fires.

LIST OF ACRONYMS

ARSC	Aerophotogrammetry and Remote Sensing Bureau of China Coal (at Xi'an, China)
ASTER	Advanced Spaceborne Thermal Emission and Reflection Radiometer (sensor on board EOS-AM1)
ATSR	Along-Track Scanning Radiometer
AVHRR	Advanced Very High Resolution Radiometer
BB1	lower Black Body reference temperature
BB2	higher Black Body reference temperature
BRSC	Beijing Remote Sensing Cooperation (at Beijing, China)
CCT	Computer Compatible Type
ChRM	Characteristic Remanent Magnetization
DEM	Digital Elevation Model
DN	Digital Number
EOS	Earth Observing System (property of NASA)
EOS-AM1	Earth Observing System-Morning
ESA	European Space Agency
ERS-1	European Remote Sensing Satellite
ETM+	Enhanced Thematic Mapper plus (on board of Landsat-7)
IFOV	Instantaneous Field Of View
ILWIS	the Integrated Land and Water Information System
InSAR	Interferometric Synthetic Aperture Radar
IR	Infrared
ITC	International Institute for Aerospace Survey and Earth Sciences
NOAA	National Oceanic and Atmospheric Administration (U.S.)
NASA	National Aeronautics and Space Administration (U.S.)
SAR	Synthetic Aperture Radar
SPOT	Système Probatoire d' Observation de La Terre
SWIR	Short Wave Infrared
TM	Thematic Mapper
TIR	Thermal Infrared
TRM	Thermomagnetic Remanent Magnetization

TABLE OF CONTENTS

ABSTRACT.....	i
SAMENVATTING.....	iv
SUMMARY IN CHINESE	vii
ACKNOWLEDGMENTS.....	x
LIST OF FIGURES.....	xii
LIST OF TABLES.....	xvii
LIST OF ACRONYMS.....	xviii
TABLE OF CONTENTS.....	xix
CHAPTER 1: GENERAL INTRODUCTION	1
1.1 BACKGROUND.....	1
1.1.1 COAL FIRES.....	1
1.1.2 SPONTANEOUS COMBUSTION OF COAL.....	2
1.1.3 COAL FIRE REMOTE SENSING.	3
1.2 AIMS OF THIS RESEARCH.....	4
1.3 RESEARCH APPROACHES	5
1.4 INTRODUCTION TO THE STUDY AREAS	6
1.5 OUTLINE OF THE THESIS.....	9
1.6 PUBLICATIONS.....	10
PART ONE: PALEO COAL FIRES IN NORTHWEST CHINA	13
CHAPTER 2: PLEISTOCENE COAL FIRES IN XINJIANG, NORTHWEST CHINA	15
2.1 INTRODUCTION	16
2.2 GEOLOGICAL SETTING	16
2.3 REMOTE SENSING DATA.	17

Table of Contents

2.4 FIELD CHARACTERISTICS OF BURNT ROCKS	18
2.5 PALEO COAL FIRES AND RIVER TERRACES	22
2.5.1 BEIGOU BURNT ROCKS.....	22
2.5.2 QIANSHUIHE-LOUZHUANGZI BURNT ROCKS	22
2.5.3 GANGOU-LIUGONG BURNT ROCKS.....	23
2.5.4 ZAOYUAN BURNT ROCKS.....	24
2.5.5 KELAZHA BURNT ROCKS.....	24
2.6 AGE OF THE PALEO COAL FIRES.....	25
2.6.1 QUATERNARY STRATIGRAPHY.....	25
2.6.2 PALEOMAGNETISM	27
2.6.3 THERMOLUMINESCENCE.....	28
2.6.4 CORRELATION WITH DATA FROM NEARBY VALLEYS.....	28
2.6.5 MODELLING USING UPLIFT RATES AND GLOBAL CLIMATE CHANGE AS INPUT VARIABLES.....	29
2.7 DISCUSSION	29
2.8 CONCLUSIONS.....	33
PART TWO: ACTIVE COAL FIRES IN NORTHWEST CHINA.....	35
CHAPTER 3: SWIR AND TIR REMOTE SENSING –SOME CONSIDERATIONS FOR THE COAL FIRE STUDY	37
3.1 INTRODUCTION	37
3.2 THERMAL INFRARED REMOTE SENSING DATA	38
3.2.1 THERMAL INFRARED REMOTE SENSING AND ATMOSPHERIC WINDOWS	38
3.2.2 WIEN’S DISPLACEMENT LAW AND COAL FIRE DETECTION.....	39
3.2.3 AVAILABLE THERMAL INFRARED DATA FROM SATELLITE BORNE AND AIRBORNE SENSORS.....	41
3.2.3.1 NOAA-AVHRR data.....	42
3.2.3.2 Landsat-5 TM band 6 thermal data and airborne thermal data	43
3.3 THERMAL ANOMALIES –SOURCES AND THE INFLUENCING FACTORS	44
3.3.1 SURFACE ENERGY BUDGET AND ATMOSPHERIC CORRECTION	44
3.3.2 SOLAR HEATING AND THE TIME AND SEASON OF THE THERMAL REMOTE SENSING DATA.....	44
3.4 LANDSAT-5 TM SWIR DATA AND SURFACE COAL FIRE TEMPERATURE AND SIZE MEASUREMENT	46
3.4.1 PHYSICAL FOUNDATION FOR TEMPERATURE DERIVATION FROM TIR AND SWIR DATA.....	46

Table of Contents

3.4.2 DUAL-BAND TEMPERATURE CALCULATION BY USING LANDSAT-5 TM BAND 5 AND BAND 7 DATA.....	47
3.4.3 THE SPECTRAL AND SPATIAL RESOLUTION OF REMOTE SENSING DATA CONCERNING MEASUREMENT OF THE TEMPERATURE AND SIZE OF THE COAL FIRES	51
3.5 CONCLUSIONS.....	52
CHAPTER 4: SOLAR HEATING SIMULATION FOR THE DETECTION OF COAL FIRES.....	53
4.1 INTRODUCTION	53
4.2 THE METHODOLOGY TO REDUCE THE UNEVEN SOLAR HEATING EFFECT.....	54
4.2.1 THE SOLAR RADIANCE REACHING THE GROUND SURFACE	54
4.2.2 SURFACE RADIANCE FROM SUN WITH RESPECT TO A DEM	56
4.2.3 CALCULATING THE ALTITUDE ANGLE (α) AND AZIMUTH ANGLE (α_s) OF THE SUN.....	57
4.2.4 CALCULATING THE SLOPE ANGLE (τ) AND ASPECT ANGLE (α_N).....	58
4.2.5 EXTRACTION OF THE THERMAL ANOMALIES FROM TM BAND 6 DATA BY SIMULATING THE RADIANCE IMAGE	59
4.3 APPLICATION OF THE METHOD.....	59
4.4 RESULTS.....	62
4.5 DISCUSSION	63
4.5.1 THE EFFECT OF SOLAR HEATING HISTORY	63
4.5.2 THE PRECISION OF THE DEM.....	64
4.5.3 OTHER EFFECTS	64
4.6 CONCLUSIONS.....	65
CHAPTER 5: SUB-PIXEL COAL FIRE DETECTION AND SURFACE TEMPERATURE MEASUREMENT FROM LANDSAT-5 TM BAND 6 DATA WITH RESPECT TO THE SPATIAL RESOLUTION	67
5.1 INTRODUCTION	67
5.2 DETECTION OF COAL FIRES.	68
5.3 METHOD.	69
5.3.1 RADIANCE COVERSION AND TEMPERATURE DERIVATION FROM TM 6 DATA.....	69
5.3.2 CONCEPT OF SUB-PIXEL DETECTION.....	71
5.4 RESULTS	73

Table of Contents

5.4.1 CAPABILITY FOR DETECTION OF A SUB-PIXEL COAL FIRE.....	73
5.4.1.1 Case 1. Sensitivity of Landsat-5 TM band 6 data for the detection of coal fires	74
5.4.1.2 Case 2. A practical detection.	75
5.4.2 CALCULATION OF HIGH TEMPERATURE COAL FIRES WITH SUB-PIXEL SIZE BY TM BAND 6 DATA.....	76
5.5 CONCLUSIONS.....	79
CHAPTER 6: SPATIAL ANALYSIS OF THERMAL ANOMALIES FROM AIRBORNE MULTI-SPECTRAL SCANNER DATA	81
6.1 INTRODUCTION.....	82
6.2 FIELD DATA	83
6.2.1 COAL FIRE SPREADING MODELS	84
6.2.2 FIELD THERMAL SURVEY.....	85
6.2.3 AIRBORNE THERMAL DATA.....	87
6.3 IMAGE PROCESSING.....	88
6.3.1 GEO-REGISTRATION.....	89
6.3.2 ADJUSTMENT OF DAYTIME BAND 5 DATA	89
6.3.3 THRESHOLDING.....	91
6.3.4 INTEGRATION.....	91
6.4 RESULTS AND DISCUSSION.....	92
6.4.1 THERMAL ANOMALIES FROM DIFFERENT DATA	92
6.4.2 THERMAL ANOMALIES DETECTED ONLY BY DAY TIME BAND 6 DATA OF 8-12.5 μm AND THE PREDICTION OF THE NEW COAL FIRES	93
6.5 CONCLUSIONS.....	99
CHAPTER 7: MULTI-SENSOR DATA FUSION FOR THE COAL FIRE MONITORING.....	101
7.1 INTRODUCTION	101
7.2 REMOTE SENSING DATA USED FOR ANALYSIS OF UNDERGROUND COAL FIRES.....	103
7.2.1 AERIAL PHOTOGRAPHY.....	103
7.2.2 AIRBORNE THERMAL INFRARED DATA	105
7.2.3 HIGH RESOLUTION OPTICAL SATELLITE DATA.....	105
7.2.4 SATELLITE THERMAL INFRARED DATA.....	106
7.2.5 SATELLITE BASED MICROWAVE DATA	108
7.3 MULTI-SENSOR DATA FUSION.....	109

Table of Contents

7.3.1 PIXEL-BASED DATA FUSION	111
7.3.2 FEATURE-BASED DATA FUSION	111
7.3.3 DECISION-BASED DATA FUSION	112
7.4 CONCLUSIONS.....	119
REFERENCES.....	123
CURRICULUM VITAE.....	135

CHAPTER 1

General Introduction

1.1 Background

1.1.1 Coal fires

China is the largest coal producer and consumer in the world. In 1996, its production of coal was 1380 million tons and 75% of China's primary energy consumption came from coal (Fan, 1997). For the foreseeable future, coal will still remain China's major source of energy. However, each year coal fires destroy from 10-20 million (ARSC, 1993; BRSC 1993; Guan *et al.*, 1996) to 200 million tons of coal resources (Rozema *et al.*, 1993; Cassells and van Genderen, 1995). These coal fires occur from NW to NE China in a belt stretching 5,000 km east-west and 750 km in a north-south direction (Guan, 1984, 1989). Nearly every coal field in North China, where 90% of China's coal resources are concentrated, suffers from scattered, localized, or clustered coal fires. The direct economic loss due to the burning of the coal resources is estimated at 1 to 2 billion RMB, and the indirect loss because of unreachable coal resources is 10 billion RMB.

In addition, coal fires are a major source of pollution both locally and globally. In 1992 the estimated amount of CO₂ released by coal fires in China was about 2-3% of the amount of the total world CO₂ output in that year (Cassells and van Genderen 1995). Coal fires also emit some noxious gases such as SO₂, H₂S, NO, CO, etc. Other problems caused by coal fires include: 1) Blockage and devaluation of coal resources in the seam below, above, and around the coal fires; 2) Damage to coal mining infrastructures; 3) Land subsidence and land slides are also the consequences of coal fires; 4) Parching the vegetation of the surface and damage to the ecological system; 5) Risk to surface structures such as railway lines, roads, oil pipelines etc.; and 6) Hazardous working conditions for coal miners.

The coal fire problem has recently been listed in the Chinese "21st-Century Agenda" as one of the five most serious geological hazards in 1994 (Guan, *et al.*, 1996).

Coal fires can be classified into 4 groups according to the place of occurrence:

- 1) Underground mine fire
- 2) Coal seam fire (coal field fire)
- 3) Coal refuse fire
- 4) Coal-stack fire

Underground mine fires, restricted to the mines, are detectable by remote sensing techniques only if they are less than 30 meters in depth (Greene et al., 1969) in areas where there are no cracks or fractures to lead the underground heat to the surface. This study mainly concentrated on coal seam fires (coal field fires). In this thesis a coal fire is defined, in most cases, as a coal seam fire or a coal field fire according to the Chinese terminology. Coal field fires normally start from the spontaneous combustion of a coal seam at the outcrop of the coal seams or at a shallow depth until the ground water is reached and then spread along both directions of the strike and dip of the coal seam. They can also develop from underground coal mine fires spreading to the surface.

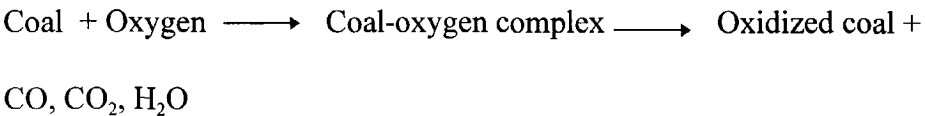
1.1.2 Spontaneous combustion of coal

There are several ways coal fires can be ignited; these include forest fires (Bustin and Mathews, 1982, 1985), lightning (Guan, et al., 1996), man-made fires, and most importantly, spontaneous combustion. Spontaneous combustion of coal occurs due to the accumulation of heat liberated from the interaction of oxygen in air with coal in ambient temperature. This interaction with oxygen is chiefly due to the oxidation of carbonaceous matter in coal. There are several theories of spontaneous combustion; the most important are the Pyrite Theory, Bacterium Theory, Phenol Theory; Electro-Chemical Theory, and the Coal-Oxygen Complex Theory (Ramlu, 1991). The generally accepted theory at present is the Coal-Oxygen Complexes Theory. According to this theory, the following stages are involved :

Stage I. An initial physical adsorption of oxygen; this only plays a major role below 0°C.

Stage II. Chemical adsorption (chemisorption) leading to the formation of the coal-oxygen complexes.

Stage III. Chemical reactions leading to the break down of the less stable coal-oxygen complexes, often resulting in the formation of gaseous products such as CO, CO₂, H₂O.



At and beyond some elevated temperature between 50° C and 100° C, the oxidation rate accelerates greatly due to a sustained exothermic reaction and ultimately produces flaming combustion or ignition. The critical or threshold temperature, usually 60° C to 85° C, depends on the nature of the coal, and in particular its moisture content thus identifying the limit of low-adiabatic conditions. Above the critical temperature the process of oxidation becomes self-sufficient.

Several important factors influence spontaneous combustion. One such factor is the nature of the coal, including its rank (Zhang & Tang, 1994), contents of volatile ash, oxygen (Banerjee, 1985), moisture (Sondreal & Ellman), pyrite, methane (Vinogradova et al., 1972), and petrography. Other important factors are the porosity of the coal seam, initial temperature, and evaporation/condensation of moisture (Schmal, 1987).

1.1.3 Coal fire remote sensing

In May 1963, HRB-Singer Inc. was invited to test the feasibility of detecting and locating coal refuse fires at Scranton, Pennsylvania (U.S.) with its RECONOFAX Infrared Reconnaissance System (Slavecki, 1964). That was the first documented study of remote sensing applications for coal fire study. Coal fires in coal refuses can be clearly recognized in thermal infrared imagery. In 1971-1972, Ellyett and Fleming studied coal field fires in the Burning Mountain in Australia using an airborne optical-mechanical-scanner operating in the infrared wavelengths. Since the 1980s, China and India, both suffering greatly from coal fire problems, started airborne remote

sensing investigations on coal fires also. In 1982-1984, ARSC took a flight campaign in Taiyuan Xishan, Shanxi, China. Multispectral scanner data, dual band thermal infrared scanner data (3-5 μm and 8-12.5 μm), and color infrared aerial photographs were taken for the study of coal fires (Guan, 1984; Li, 1985). The burnt rocks can be easily detected in color infrared photographs. In 1986, the Remote Sensing Center of the Chinese Ministry of Geology and Mineral Resources made a test in Rujigou, Ningxia (Huang, et al., 1991). The sensor they used was the Dual Channel Daedalus DS-1230 Thermal Scanner. In 1992, ARSC made another attempt in Xinjiang for further study using a Chinese-made Hangding-40 Airborne Multispectral Scanner. In cooperation with Russia, India started remote sensing research of coal fires in the Jharia coal field of Bihar State using airborne remote sensing data for coal fire mapping during 1984-1987 (Bhattacharya, et al., 1991). Since late 1980s, satellite thermal data were used for coal fire studies (Guan, 1989; Huang, et al., 1991; Chen, 1992; Bhattacharya, et al., 1991; Mansor, et al., 1995, Prakash, et al., 1995a, 1995b). During this decade, researchers also started to use short wavelength remote sensing such as band 7 and band 5 of TM data for the detection of high extensive hot sources and surface coal fires (Reddy, et al., 1993; Prakash, et al., 1997). GIS techniques were adopted recently for coal fire monitoring by Chinese scientists (Wan and Zhang, et al., 1996a, 1996b).

1.2 Aims of this research

“Environmental Monitoring of Spontaneous Combustion in the North China Coal Fields” sponsored by the European Commission under contract No. CII*-CT93-0008, is a joint research project between the International Institute for Aerospace Survey and Earth Sciences (ITC) in Enschede, the Netherlands, and the Aerophotogrammetry and Remote Sensing Bureau of China Coal (ARSC) in Xi'an, China. It aims to set up a methodology for the efficient detection, measurement, and monitoring of the coal fires by means of remote sensing data and the setting up of a GIS monitoring system for regular monitoring of coal fires in the northern part of China. The author's research aims to contribute to this project at a basic level by obtaining a better understanding of the phenomena by: (1) researching the evolution of the paleo-coal fires, (2) by methodology studies, and (3) on detection techniques by using remote sensing data. In addition, this thesis intends to answer the following questions:

- 1) How old are the paleo-coal fires in Xinjiang? (Chapter 2)
- 2) How can the spatial and spectral resolution of the remote sensing data influence the coal fire study? (Chapter 3)
- 3) How can the influence of solar heating effects on Landsat TM thermal data be reduced? (Chapter 4)
- 4) How can one evaluate the capability of a sensor with a certain spatial resolution for coal fire detection in terms of the size and temperature of the coal fire? (Chapter 5)
- 5) How can airborne data be used to distinguish different kinds of fires, measure the spreading directions, and predict the future high-risk coal fire areas? (Chapter 6)
- 6) What should a general detection and monitoring procedure based on remote sensing techniques contain? (Chapter 7)

1.3 Research Approaches

For this research, three accessible test areas at Toutunhe, Xishan, and Sangong-Dahuangshan were chosen. These test areas are located at the northern side of the Tianshan mountains close to Urumqi, the capital city of Xinjiang Uygur Autonomous region in N.W. China. Within these areas, burnt rocks (most of them the result of paleo coal fires) and active coal fires are widespread. The test areas are in a semi arid zone with very sparse vegetation coverage. They are geologically located in the transition belts of the Tianshan Foldbelt and the Jungger Basin.

Field research was carried out in Xinjiang during 1994 from the 21st of September to the 1st of November, and in 1995 from the 6th of August to the 18th of September. A further field work period was carried out in another coal fire area in Ningxia Hui Autonomous Region during the period between the 15th of August and the 22nd of September 1996 to compare the situation to that in Xinjiang and to see how far the techniques and models developed in the Xinjiang test areas could be applied to other coal fire areas. The burnt rocks and their relationships with the terraces were observed in the Toutunhe area and samples of burnt rocks were collected for paleomagnetic examination. The studies in Chapter two are mainly based on this field work data and on laboratory results. The surface temperature of the active coal fires were measured by using a Japanese-made portable pyroelectric infrared thermal radiometer. This served as

ground truth data for the remote sensing analysis and for the spatial resolution considerations of various thermal remote sensing data.

Space and airborne remote sensing data covering the test areas were collected. They are listed in Table 1-1. All these data are in digital form (except the color infrared aerial photographs) in order for image processing to be carried out. Remote sensing data fusion techniques have been used for the analysis of the different aspects of the coal fires in the imagery (Chapter 6 and Chapter 7). GIS techniques were used for coal fire analysis in Chapter 4 by generating a DEM and calculating the relative heating of solar radiation.

1.4 Introduction to the study area

Among the three test areas, the Toutunhe and Xishan study areas are situated about 30 km southwest of Urumqi, the capital of Xinjiang, in the transition zone of the Tianshan Foldbelt and the Junggar Basin at an altitude between 1000 and 1400m. They are crossed by the Toutunhe and Xiaoquanzi River, respectively.

The core of the E-W trending Tianshan Foldbelt consists of pre-Mesozoic basement rocks (Bureau 1993). On the northern side of Tianshan, Mesozoic and Cenozoic sedimentary rocks have been detached from the underlying pre-Mesozoic rocks and are folded into three zones of E-W trending anticlines and synclines. The first southernmost row of folds involves mainly Jurassic and Cretaceous and was formed at the end of Cretaceous due to the Yanshan orogenic phase. The second and third rows of the folds include the Neogene system and lower Pleistocene. The Kelazha anticline in the study area is situated in the first row, with Jurassic strata forming the core of the folds. Unfolded Pliocene sediments unconformably cover the Jurassic and Cretaceous rocks.

The main coal-bearing strata that have burnt out belong to the Middle Jurassic Xishanyao Group, which consists of fresh-water deltaic sediments including mudstone, siltstone, sandstone, and coal layers (Bureau, 1993; Schneider, 1996). Out of these, 2-11 layers are considered mineable. The coal layers are concentrated in the lower parts of the Xishanyao Group with

Table 1-1. Remote sensing data used for this study

Platform and sensor	Spectral bands	Spatial resolution	Day or night acquisition	Dates of acquisition
Airborne MSS	Band 3: 0.61 – 0.69 μm	~7 m	day	9/8/92
	Band 5: 3.0 – 5.0 μm	~7 m	day	9/8/92
	Band 6: 8.0 – 12.5 μm	~7 m	day	9/8/92
	Band 6: 8.0 – 12.5 μm	~7 m	night	30/7/92
Airborne RC-10 camera (C.I.R)	Blue: 0.5-0.6 μm Green: 0.6-0.76 μm Red: 0.76-0.8 μm	~1 m	day	9/8/92
SPOT	Band 1: 0.5-0.59 μm	20 m	day	7/11/1988
	Band 2: 0.6-0.68 μm			
	Band 3: 0.79-0.89 μm			
Landsat-TM	Band 1: 0.42-0.52 μm	30 m	day	20/1/89 3/6/90 2/8/90 13/9/94 14/9/94
	Band 2: 0.53-0.60 μm			
	Band 3: 0.63-0.69 μm			
	Band 4: 0.76-0.90 μm			
	Band 5: 1.55 – 1.75 μm	30 m		
	Band 7: 2.08 – 2.35 μm	30m		
	Band 6: 10.4 – 12.5 μm	120 m		
ERS-1-ATSR	10.0 and 11.0 μm bands	1.0 km	day and night	22/3/95 (cloudy) 31/3/95 (cloudy) 7/4/95 (clear) 25/5/95 (cloudy)
ERS-1-ATSR	10.0 and 11.0 μm bands	1.0 km	day and night	5/4/94, 13/4/94, 15/4/94, 15/4/94, 13/4/95, 14/4/95, 14/4/95, 4/5/95, 19/5/95, 5/6/95, 23/6/95, 7/7/95, 28/7/95, 5/8/95, 13/8/95

Table 1-1 (Continued)

Platform and sensor	Spectral bands	Spatial resolution	Day or night acquisition	Dates of acquisition
NOAA-AVHRR	Band 3: 3.55 – 3.93 μm	1.1 km	day	29/1/94, 30/1/94 26/2/94,
	Band 4: 10.3 – 11.3 μm			25/3/94 26/3/94 30/9/94
	Band 5: 11.3 – 12.5 μm			10/10/94 14/10/94

thickness varying from 1 to 27 m. The lowest mineable layer is called the Dacao coal layer with a constant thickness of 15-17 m.

The folded Jurassic coal-bearing strata have been incised by the Toutunhe river and its tributaries as a result of Cenozoic uplift. The interplay of tectonic uplift and cyclic sedimentation caused by glaciations in the Tianshan mountains and interglacial dissection led to the formation of a flight of at least six river terraces in the valleys (Molnar *et al.*, 1993).

The third test area at Sangong-Dahuangshan is situated about 90 km east of Urumqi. The geographical, geological, and coal fire characteristics are very similar to those in the other test areas. The surface coal fires are only observed in the third test area (Chapter 3). The coal-bearing strata, composed of Lower Jurassic Badaowan Group and Middle Jurassic Xishanyao Group, are folded into a syncline. The SPOT satellite data are only available for this test area.

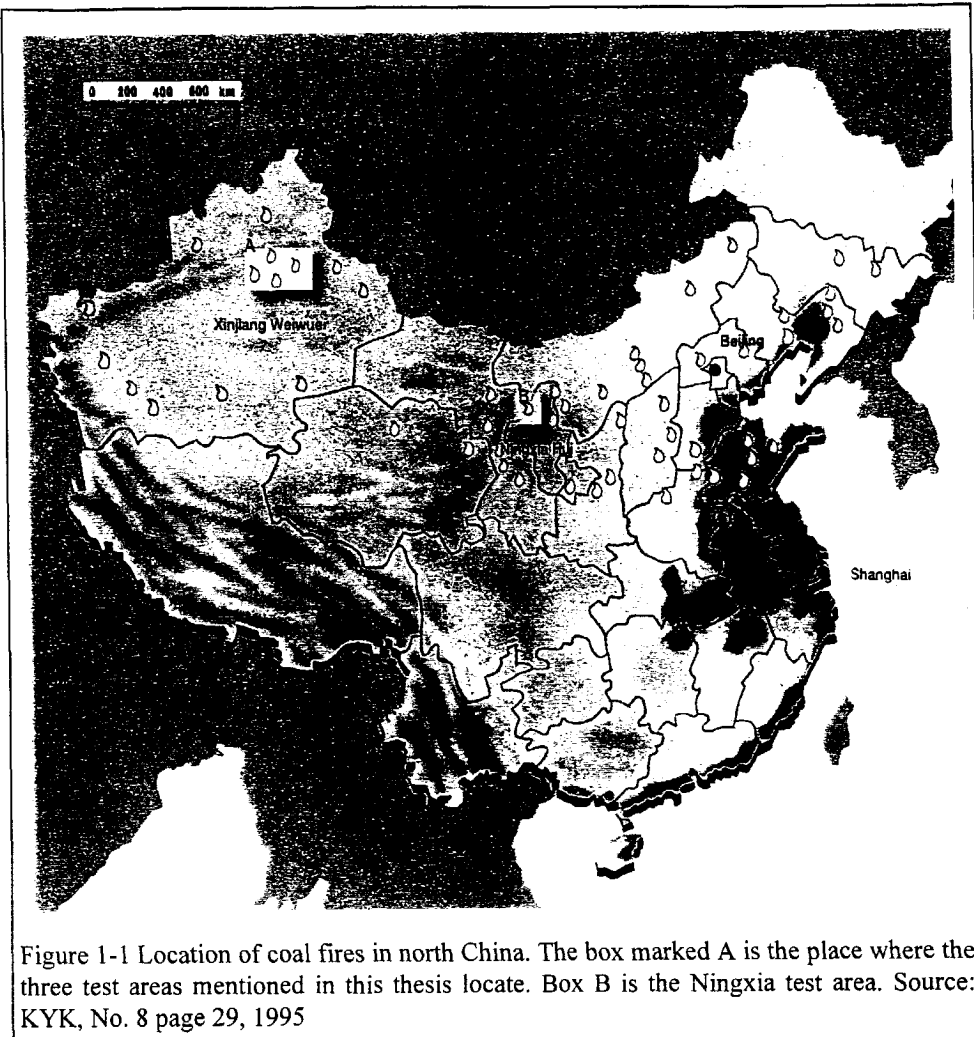


Figure 1-1 Location of coal fires in north China. The box marked A is the place where the three test areas mentioned in this thesis locate. Box B is the Ningxia test area. Source: KYK, No. 8 page 29, 1995

1.5 Outline of the thesis

The thesis is divided into two parts. The first part deals with the paleo coal fires by dating their ages on the basis of field data and laboratory examination; the second part studies the active coal fires by using remote sensing techniques.

In Chapter 2, the evolution of the paleo coal fires in Toutunhe and Xinjiang areas are studied. Several age groups of burnt rock have been recognized

and their relationships with the river terraces will be discussed. The causes of the paleo coal fires are addressed, and the areas of coal fires with different ages have been dated.

In Chapter 3, the physical basis of thermal infrared remote sensing for the detection and measurement of coal fires are addressed with an emphasis on the spatial, spectral, and radiometric resolution.

In Chapter 4, a method to reduce the effect of solar heating, the main factor of confusion when investigating the thermal anomalies of coal fires, is discussed with the help of a DEM.

In Chapter 5, as the coal fires normally occupy only part of one pixel of the Landsat TM thermal channel data, the capability of sub pixel coal fire detection is addressed.

In Chapter 6, the airborne data from different wavelengths acquired at different times are studied to analyze the spatial thermal characteristics of the coal fires. Spreading direction and different types of coal fires are studied.

Chapter 7 presents, based on multi-sensor data fusion techniques, a hierarchical methodology for detection and monitoring of the coal fires.

1.6 Publications

Chapters 2 through 7 were or will be published as separate papers with some modifications. The full literature references to these are given below.

Chapter 2

Zhang, X. M., Kroonenberg S. B. and Boer C. B. de., 1998, Pleistocene coal fires in Xinjiang, northwest China, *Terra Nova -The European Journal of Geosciences* (submitted).

Chapter 3

- Zhang, X. M, Koopmans, B. N., and Wan, Y., 1995, Detection of spontaneous combustion of coal in northern China, using thermal remote sensing data. *Proceedings of International Space Congress*, Bremen, Germany, May 23-25th, 1995, pp 2-10.
- Genderen, J. L. van., Cassells, C.J. S., and Zhang, X. M., 1996, The synergistic use of remotely sensed data for the detection of underground coal fires. *International Archives of Photogrammetry and Remote Sensing*, vol. xxxi, part 7, Vienna, 9-19 July, 1996.
- Cassells, C. J. S., Genderen, J. L. van and Zhang X. M., 1996, Detection and measuring underground coal fires by remote sensing - *Proc. 8th Australasian Remote Sensing Conference*, Canberra, March, 1996: vol 2, 90-101.

Chapter 4

- Wan, Y. Q and Zhang, X. M., 1996, Using a DTM to reduce the effect of solar rediance on Landsat TM thermal IR images and detection coal fires, *Asian-pacific Remote Sensing and GIS Journal*, Volume 8, Number 2, p 65-72.

Chapter 5

- Zhang, X. M., Genderen, J. L. van and Kroonenberg S. B., 1997, A method to evaluate the capability of Landsat-5 TM band 6 data for sub-pixel coal fire detection, *International Journal of Remote Sensing*, Vol. 18, No. 15, 3279-3288.

Chapter 6

- Zhang, X. M., Genderen, J. L. van and Kroonenberg S. B., 1998, Spatial analysis of thermal anomalies by airborne multi-spectral scanner data, *International Journal of Remote Sensing* (submitted).

Chapter 7

- Zhang, X. M., Cassells, C., and Genderen J. L. van., 1998, Multi-sensor data fusion for the detection of underground coal fires, *Geologie & Mijnbouw*, Vol 77 (in press).

PART ONE:

**PALEO COAL FIRES IN
NORTHWEST CHINA**

CHAPTER 2

Pleistocene Coal Fires in Xinjiang, Northwest China^{*}

ABSTRACT

Coal fires in China are not only an economic threat but also an environmental one because of their significant contributions to the global CO₂ budget. This study shows that over 85% of the burnt rock recognized in remote sensing imagery in NW China is of Pleistocene age. Several age groups of burnt rock have been recognized: (1) Beigou burnt rocks, deeply weathered and unconformably overlain by an Pliocene-Early Quaternary alluvial fan and now deeply dissected and situated over 200 m above the Toutunhe River; (2) Middle Pleistocene Qianshuihe-Louzhuangzi burnt rocks, situated above the highest (90 m) terraces of the Toutunhe River. The terrace sediments which cover the burnt rocks are unbaked; (3) Late Pleistocene Gangou burnt rocks which are unconformably overlain by gravel of the 70 m terrace of the Toutunhe River incorporate burnt terrace gravel which cannot be older than the 90 m level; (4) Holocene Zaoyuan paleo coal fires baking the gravels of the lowest terrace are still younger than group 3; and (5) active coal fires and related burnt rocks.

Spontaneous combustion of coal fires is related to the creation of favorable outcrops by deformation, uplift, and unroofing by erosion. Groups (1) and (2) are mainly related to deformation and uplift, and groups (3) and (4) to interglacial dissection of (fluvio) glacial terrace sediment at moderate uplift rates (around 0.1 mm/y). The increase in the area of active coal fires compared with the paleo coal fire area of group 3 and 4 is mainly due to unplanned mining.

^{*}This chapter has been submitted for publication as:

Xiangmin Zhang, Salomon B. Kroonenberg and Cor B. de Boer, 1998, Pleistocene Coal Fires in Xinjiang, Northwest China. *TERRA NOVA* The European Journal of Geosciences, (submitted).

2.1 Introduction

Coal fires are one of the most serious environmental and economic problems in China. Estimates of annual losses by coal fires in China range from about 10-20 million tons (ARSC 1993, BRSC 1993; Guan *et al.*, 1996) to 200 million tons (Rozema *et al.*, 1993; Cassells and Genderen, 1995). Apart from a national problem, coal fires have a global dimension as well; in 1992 the estimated amount of the CO₂ released by coal fires in China was about 2-3% of the amount of the total world CO₂ output in that year (Cassells and Genderen 1995). Therefore, early detection, monitoring, and prevention of coal fires is a high-priority task. At present, the joint project "Environmental Monitoring of Spontaneous Combustion in the Northern China Coalfields," sponsored by the European Commission, is being carried out by the International Institute for Aerospace Survey and Earth Sciences (ITC) and Aerophotogrammetry and Remote Sensing of China Coal (ARSC). Remote sensing is especially suitable as it enables rapid assessment of coal fires over large areas. Various kinds of remote sensing techniques are being used for the detection, measurement, and monitoring of active coal fires in Xinjiang Autonomous region, Northwest China. In night-time thermal IR imagery, active coal fires can be detected easily (Cassells and Genderen, 1995; Zhang *et al.*, 1995, 1996), while in the visible and reflective IR part of the spectrum burnt rocks can be recognized by their special reflection in airborne and spaceborne imagery. However, field studies have shown that many areas underlain by burnt rocks do not show thermal anomalies in the imagery or in the field. The data presented in this paper show that many areas of burnt rocks were formed far back in the Pleistocene. Coal fires are not only environmental and economic hazards caused by mining, but also natural geological phenomena. The areal extent of active coal fires might therefore become overestimated if only spectral characteristics of burnt rocks are used.

2.2 Geological setting

The Toutunhe study area is situated 30 km southwest of Urumqi, the capital of Xinjiang, in the transition zone of the Tianshan mountain range and the Junggar basin at an altitude between 1000 and 1400m. It is crossed by the Toutunhe River fed and by the glaciers of the Tianshan mountain and by its tributaries, the Qianshuihe, Gangou, and Haojiagou (Figure 2-1).

The core of the E-W trending Tianshan Mountain range consists of pre-Mesozoic basement rocks. (Bureau, 1993; Carroll *et al.*, 1995; Peng and Zhang, 1989) On the northern side of Tianshan, Mesozoic, and Cenozoic sedimentary rocks have been detached from the underlying pre-Mesozoic rocks and folded into three rows of E-W trending anticlines and synclines. The first, southernmost row of folds involve mainly the Jurassic and Cretaceous and were formed at the end of the Cretaceous period due to the Yanshan orogenic phase. The second and third rows of the folds include the Neogene system and lower Pleistocene. The Kelazha anticline in the study area is situated in the first row, with Jurassic strata forming the core of the folds. Unfolded Pliocene sediments unconformably cover the Jurassic and Cretaceous rocks.

The main coal-bearing strata that have burnt out belong to the Middle Jurassic Xishanyao Group, which consists of fresh-water deltaic sediments including mudstone, siltstone, sandstone, and coal layers (Bureau, 1993; Schneider, 1996). Out of these, 2-11 layers are considered mineable. The coal layers are concentrated in the lower parts of the Xishanyao Group with a thickness varying from 1 to 27 m. The lowest mineable layer is called Dacao coal layer with a constant thickness of 15-17 m.

The folded Jurassic coal-bearing strata have been incised by the Toutunhe River and its tributaries as a result of Cenozoic mountain building. The interplay of tectonic uplift and cyclic sedimentation caused by glaciation in the Tianshan mountains and interglacial dissection led to the formation of a flight of at least six river terraces in the valley (Figure 2-2, 2-3) (Qiao, 1981; cf. Molnar *et al.*, 1993). These play an important role in establishing the age of the paleo-coal fires. The uppermost ones are situated about 90 m above the river, the lowermost one about 15 m above present river level. The other terraces are situated between these with a regular space interval of about 10-15 m. Most of the terraces are cut into bedrock and capped by 1-3 m of coarse gravel.

2.3 Remote sensing data

In order to map the extent of present-day and fossil coal fires in the Liuhuanggou area remote sensing data have been studied prior to field work. They mainly include airborne thermal infrared scanner data (night-time) and

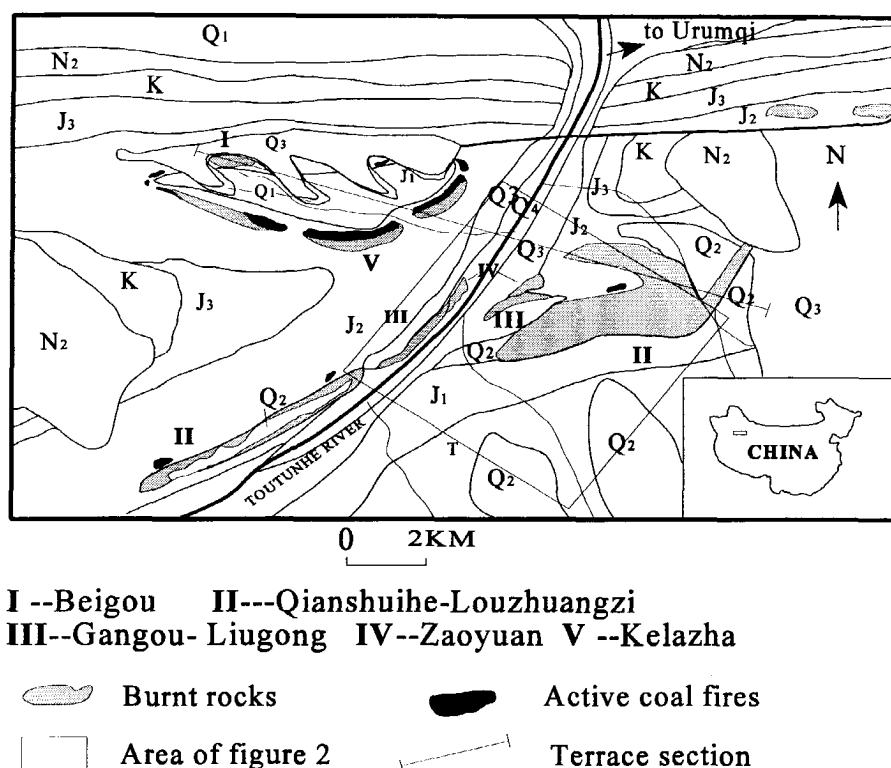


Figure 2-1: Geological map of study area with distribution of burnt rocks and active coal fires

color infrared stereophotographs. The thermal data were acquired on the 30th of July 1992 at a wavelength of 8-12 μm . Present-day active coal fires in the study area can be easily detected, thus the area of the active coal fires was calculated to be compared with the areas of different age groups of paleo-coal fires (see below). The color infrared stereo photographs, acquired on the 7th of August 1992 at a scale of 1:25,000, have proven to be very useful for the recognition of burnt rocks and their outcrop conditions.

2.4 Field characteristics of burnt rocks

Under natural conditions a coal fire can start wherever a coal seam outcrops near the surface. Natural exposure of coal seams can be caused by such processes as faulting, folding and denudation, or valley incision by streams. Once exposed, spontaneous combustion can start, as this is an exothermic oxidation process as soon as a certain threshold temperature is surpassed

(Banerjee, 1985). Under natural conditions the threshold temperature can be exceeded by forest fires, lightning, and by sun heating of favorably exposed coal seams. What happens during and after a coal fire is best appreciated at the outcrops of burnt rocks where the coal fire has ended a long time ago.

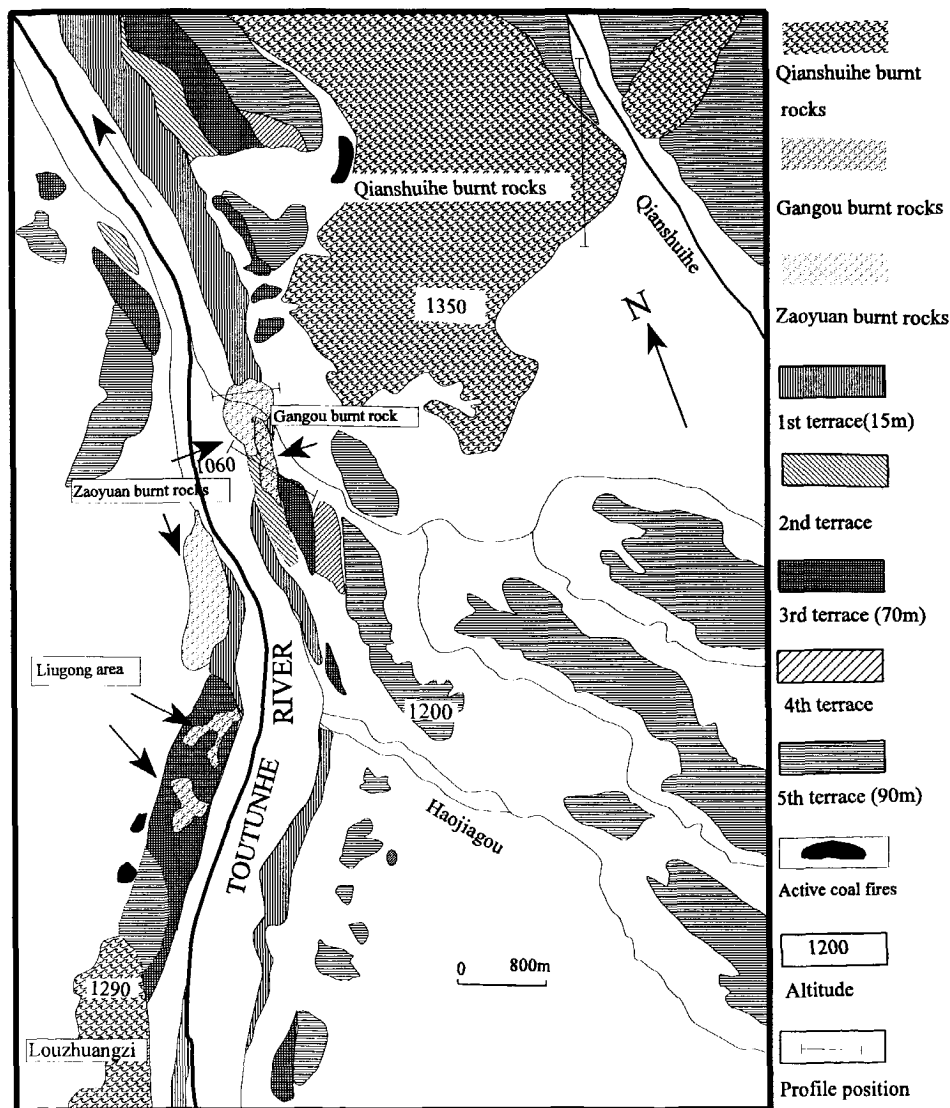


Figure 2-2: Distribution of burnt rocks and river terraces

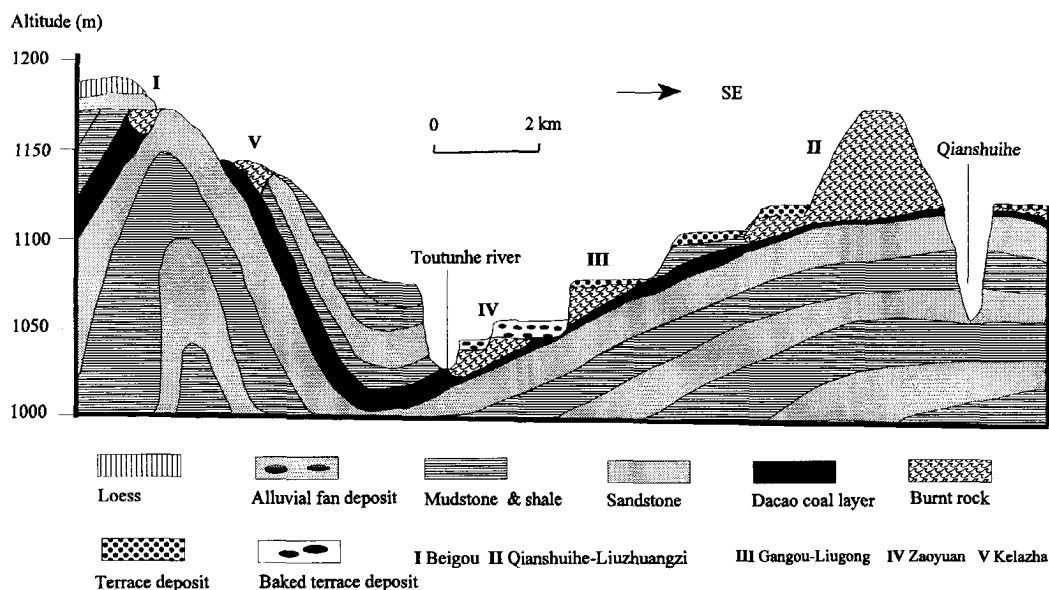


Figure 2-3: Cross-section of Toutunhe River terraces and burnt rock occurrences

Burnt rock (pyrometamorphosed rock) is a general term for thermally metamorphic rocks originating from the heating of overlying rocks by the burning of coal seams. Burnt rocks can be classified according to characteristics such as color, texture and structure, and metamorphic temperatures (Guan, 1963). In a face-slope exposure of slightly dipping burnt rocks in a cuesta such as the Qianshuihe outcrop, (Figure 2-4) a characteristic profile is developed. At the bottom, there are the unburnt rocks underlying the coal seams. Nearing the contact with the burnt coal seam, the rocks gradually get a baked appearance, as is obvious in mudstones from the brick-red color, ceramic character and sound, and sometimes a characteristic mm-sized six-sided columnar structure (chopstick rock) caused by shrinkage joints disposed in a sheaf-like fashion, not unlike jointing in basaltic lava flows. These have been baked at temperatures between 500-800°C (Guan H., pers. comm). At the very outcrop where ignition started, the red baking of underlying mudstones may be absent, probably because enough heat could be released into the air. But as soon as the fire propagates inward, red-baked rocks appear. This is seen in outcrops cut perpendicular to the strike of the coal seam. Elsewhere, the

presence of a characteristic hardened Kaolin layer (baked underclay) seems to have acted as an insulator, thus protecting the underlying rocks from baking. Sandstones appear less affected by baking alone. Iron concretions occurring in sandstone and mudstone become slightly magnetic as a result of baking. The coal seam itself has been reduced to a thin ash layer of only a few centimeters in thickness, often rich in gypsum. Above the ash layer the roof of the coal seam has usually collapsed, resulting in a breccia-like structure. As the temperature of coal fires usually increases as a result of a better supply of oxygen, these rocks also become partially molten. Between the partly molten fragments of collapsed roof rocks, often a dark vesicular glassy matrix is found, sometimes with micro-flow structures as in ropy lavas. These rocks have attained temperatures between 1000-1200°C, based on mineralogical evidence. Locally occurring completely molten scoria-like rocks may have attained temperatures between 1500-2100° (Guan, H., pers. comm.). Loess overlying burnt rock may have been baked to brick-like substances. The maximum thickness of the burnt rocks in the study area of Qianshuihe, Louzhuangzi is about 100-150 m.

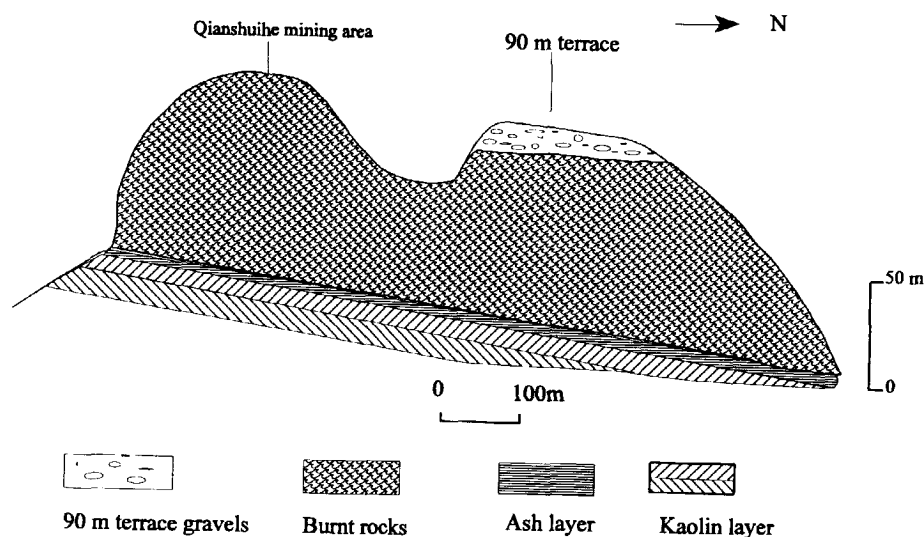


Figure 2-4: Qianshuihe burnt rock profile

2.5 Paleo-coal fires and river terraces

The outcrop conditions of the paleo-coal fires in the Liuhuanggou area are intimately related to the development of different river terraces (Figure 2-3). This is understandable, as dissection by the river exposes new coal seams to the air. Five age groups of burnt rocks have been recognized in this area based on their relationship with the terraces.

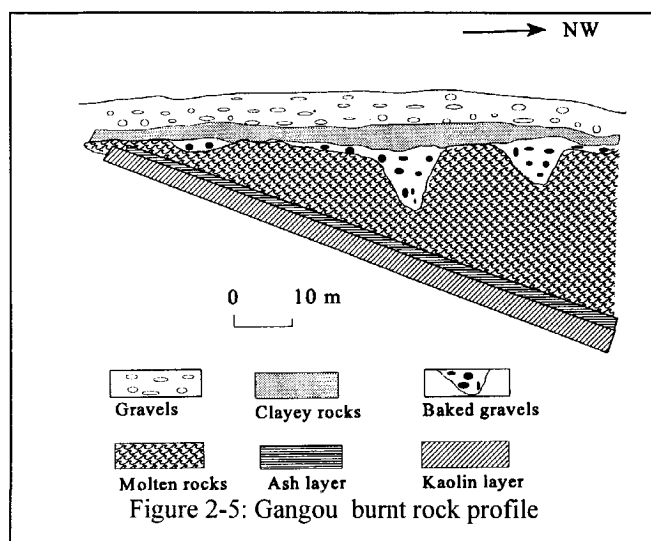
2.5.1 Beigou burnt rocks

The morphologically oldest burnt rocks are found at the Beigou outcrop along the northern flank of the anticline at an altitude of 1240 m. Here steeply dipping E-W trending Middle Jurassic rocks have been dissected by the S-flowing Beigou tributary of the Toutunhe River down to a depth of more than 200 m. However, before dissection a thin alluvial fan was deposited on the horizontally eroded surface of the Jurassic rocks. Dissected remains of this fan are still visible on each interfluvium between the individual branches of the Beigou River. Moreover, the interfluviums are partly covered with loess, especially on their eastern sides. At the contact of the steeply dipping Jurassic rocks and the overlying horizontal fan deposits, remains of a coal fire were detected (Figure 2-3). No confusion is possible with the reddened Jurassic rocks themselves (Schneider, 1996) because the burnt rocks show the characteristic chop-stick structure and are magnetically anomalous. The burnt rocks have been truncated by unbaked horizontal gravelly alluvial fan deposits, suggesting that the coal fire took place in the flat pediment before deposition of the fan, and, for that matter, far before dissection started.

2.5.2 Qianshuihe-Louzhuangzi burnt rocks

In the Qianshuihe area in the eastern part of the study area (Figure 2-1), a folding of the Jurassic strata into a small anticline and a syncline brought the Dacao coal seam close to the surface. Where dissection brought the coal seam in contact with the air, a classic profile of baked and molten rock developed as described above (Figure 2-4). The molten scoriaceous breccias on top are about 20 m in thickness. Underneath the burnt Dacao coal layer there is a baked kaolin ('porcellanite') layer, possibly of volcanic ash origin, which is being mined by a local steel factory as refractory material for the

furnaces. On the north side of the hills the burnt rocks are covered by unbaked gravels of the 90 m terrace. To the SE of the 90 m terrace remains the burnt rocks crop out on top of hills that project above the highest terrace level of the river, and no Quaternary sediments cover them. This means the paleo-coal fires should be older than the 90 meter terrace because the burnt-out seam below the gravel and on top of the hill is the same, though burning at the latter site could have started earlier.



A similar situation is found in the southwestern part of the area near Louzhuangzi along the western side of the Toutunhe River. Several hills capped with burnt rocks occur above the highest terrace, while at the northern side of the hill burnt rocks are covered by unbaked terrace

gravel belonging to the same terrace level as that covering the Qianshuihe burnt rocks. On top of the coarse gravels there is a loess layer. This suggests that the Qianshuihe and Louzhuangzi burnt rocks belong to the same age group. The total thickness of burnt rocks in both areas is 100-150 m.

2.5.3 Gangou-Liugong burnt rocks.

Along the lowermost reach of the Gangou tributary of Toutunhe River, burnt rocks, molten breccias, and small lava-like glassy flows are overlain by unbaked gravel of the 70 m terrace of the Toutunhe River (Figure 2-5). The molten rocks are 15-20 m thick, and are related to the same Dacao coal layer underlain by the kaolin layer. The pebbles of the 70m terrace do not show any sign of baking, but within the molten collapsed roof of the coal seam strongly deformed, molten, and baked pebbles have been found, which must be derived from an older cover of terrace gravel deposited prior to the coal fire and incorporated into the breccia by collapse of the roof during the

coal fire. As the next higher terrace upslope from the Gangou profile is the 90 m terrace, the age of this coal fire is bracketed probably between the age of the 70 m and 90 m terraces. As the coal seam probably started to burn soon after the exposure, the age of the burnt rocks represents the time of downcutting into the bed rocks.

We found similar burnt rocks at the Liugong site at the west side of Toutunhe River. The aggradational terrace sediments are undisturbed by the paleo-coal fires. Also, the contact relationship clearly shows the burnt rocks are older than the 70 m terrace. The sediments on top of the Gangou-Liugong burnt rocks 70 meters above present river bed are among the thickest terrace sediments in the area.

2.5.4 Zaoyuan burnt rocks

Zaoyuan burnt rocks adjacent to the Gangou burnt rocks lie on the first and second terrace of Toutunhe River (Figure 2-5). The pebbles on top of the burnt rocks were completely baked, and even partially molten. On the top of the baked pebbles there are no aggradational sediments. On the stereo color infrared photographs these burnt rocks can be easily recognized. In the west side of the Toutunhe River, the same burnt rocks can also be found. The first and second terraces are composed of eroded bed rocks and a thin layer of pebbles.

2.5.5 Kelazha burnt rocks

The Kelazha burnt rocks are directly related to the active coal fires, as detected by thermal IR imagery and by field reconnaissance. These burnt rocks occur above, around, or close to the active coal fires. They differ in a number of aspects from the paleo-coal fires. No complete sections can be seen, as most fires are raging below the ground surface. This probably explains the scarcity of molten rocks. Most characteristic are differences in surface mineralogy as related to temperatures at the vents, as measured with the thermal radiometer in the field (cf. Zhang *et al.*, 1995). On a horizontal surface, coal fire vents below 80-90° have a halo around them consisting of tarry substances mixed with sulfur. Between 90-120° the halo consists of native sulfur alone, while above 120°, above the sublimation point of sulfur, white linings of salmiac can be found. None of these materials have been

found in paleo-coal fires. The color of the recent Kelazha burnt rocks is lighter than the burnt rocks from paleo-coal fires.

2.6 Age of the paleo coal fires

From the field occurrences of the burnt rocks, five age groups have been distinguished (cf. Figure 2-3): (1) Beigou: older than the alluvial fan at 200 m above the Toutunhe River; (2) Qianshuihe-Louzhuangzi: older than the 90m terrace; (3) Gangou: age between those of the 90 and 70 m terrace levels. (4) Zaoyuan: first and second terrace levels; and (5) Kelazha: recent. Establishing the absolute age of these paleo-coal fire groups has proceeded along different lines:

2.6.1 Quaternary stratigraphy

The stratigraphy and age of the river terrace deposits in the Toutunhe area are closely related to glaciation and deglaciation in the adjacent Tianshan Mountains. A general age classification spanning the whole Quaternary has been obtained (Qiao, 1981; Bureau, 1993) mainly by correlation with morainic stages in the upper reaches of the Toutunhe Rivers (Bo, 1981a, 1981b; Qiao, 1981, Hong, et al., 1981). Unfortunately these data are not yet supported by an absolute chronology, and dating old moraines is notoriously tricky.

According to these data, the Beigou alluvial fan could be a Late Pliocene or Early Pleistocene (Q1 high terrace, in Chinese terminology, 0.7-2 Ma). These deposits might correspond to the Xiyu formation where abundant Late Pliocene fauna has been found to be generally associated with the inception of glaciation (Qiao, 1981; Molnar *et al.*, 1993).

The Qianshuihe and Louzhuangzi 90 m terraces are fluvio-glacial, and of Middle Pleistocene age, (Q2, 0.7-0.1 Ma). The only published 'age' control is the find of *Palaeoloxodon*, a fossil elephant (now generally included in the genus *Elephas*; Nilsson, 1983) in the Middle Pleistocene gravels at Yaomuoshan about 15 km east of the study area (Qiao, 1981). The Gangou 70 m fluvio-glacial terrace is estimated by Qiao (1981) to be Late Pleistocene (Q3, 100-10 ka), and the Zaoyuan and Kelazha coal fires are probably

Holocene (Q4, <10 ka). Loess deposits in this area are generally held to be Late Pleistocene in age.

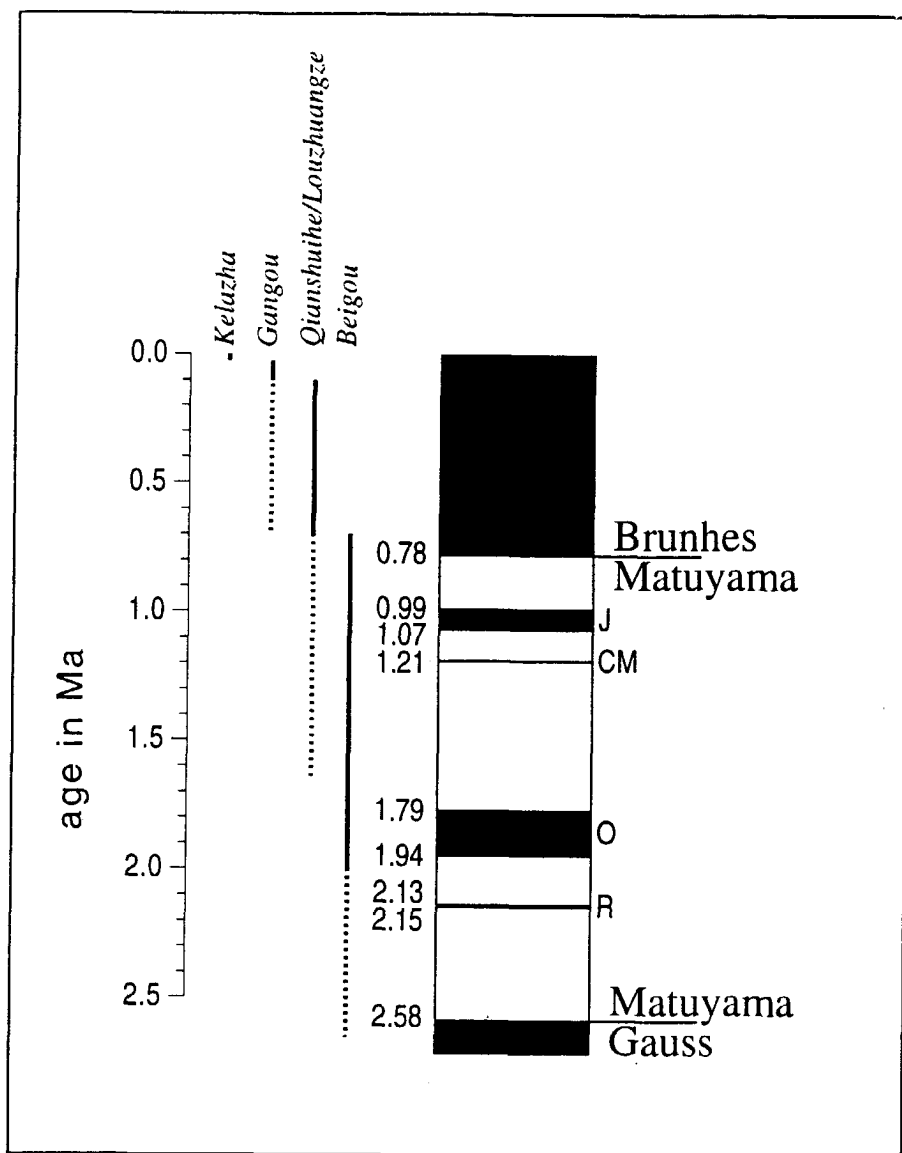


Figure 2-6: Geomagnetic polarity time scale of the late Pliocene to Holocene according to Lourens et al. (1996). Black (white) blocks denote periods with normal (reversed) directions of the geomagnetic field. J: Jaramillo; CM: Cobb Mountain; O: Olduvai; R: Reunion. Vertical lines represent the age estimates based on stratigraphy.

2.6.2 Paleomagnetism

Paleomagnetic measurements were carried out on rock samples collected in the field to constrain the age estimates of the coal fires magnetostratigraphically. The characteristic remanent magnetization (ChRM) of the samples was determined to obtain their magnetic polarity. The magnetic polarity pattern of the burnt rocks can then be correlated to the geomagnetic polarity time scale (Figure 2-6) based on irregular reversals of the earth magnetic field. This method has been used successfully in dating porcellanites from the North Bohemian Coal Basins (Tyráček, 1994).

Ten oriented hand samples were taken in the field; two samples from each of the Beigou, Qianshuihe-Louzhuangzi and Kelazha groups, and four samples from the Gangou-Liugong group. From each hand sample, one core (diameter of 25 mm) was drilled in the laboratory and several specimens with a length of 22 mm were cut from each core. At least one of the specimens was stepwise demagnetized with alternating fields.

All cores showed normal ChRM directions (Figure 2-7). The directions of the ChRM in these burnt rocks could be caused by a thermomagnetic remanent magnetization (TRM) acquired at the time of final cooling. The pyrometamorphosed rocks of the Xinjiang region, in particular the breccious types on top of the burnt coal seams show field evidence of having reached temperatures well above 770°C, i.e. higher than the Curie points (T_C) of all magnetic minerals. On cooling below their T_C , magnetic minerals acquire a magnetization parallel to the ambient geomagnetic field. If the measured remanence is indeed a primary TRM, it implies that the sampled rocks all cooled during a normal period of the geomagnetic field. On the basis of the general stratigraphy outlined above, normal directions of the ChRM are expected for the samples from the Holocene (<10 ka) Kelazha group and the middle to late Pleistocene (0.7-0.01 Ma) Gangou-Liugong group, because these groups of burnt rocks are younger than the beginning of the last normal polarity interval (Brunhes Chron: 0-0.780 Ma). The normal polarities of the relatively older Qianshuihe-Louzhuangzi and Beigou groups yield various options for their paleomagnetic age: slightly younger than 0.780 Ma (beginning of the normal Brunhes Chron), between 0.990 and 1.070 Ma (Jaramillo subchron) or at 1.21 Ma (Cobb Mountain cryptochron). Older options for the burnt rocks from the Beigou group are the normal

polarity intervals during the late Pliocene: Olduvai subchron (1.785 and 1.942 Ma); Reunion subchron (2.129-2.149 Ma) and the end of the normal Gauss Chron ≥ 2.582 Ma (Lourens *et al.*, 1996).

The significance of these paleomagnetic datings at the end of the coal fires, however, must be regarded with some caution. Trace amounts of native iron ($T_C = 770^\circ\text{C}$), especially in the Kelazha and Gangou-Liugong samples, were detected during thermomagnetic runs on a Curie balance (Figure 2-8; De Boer *et al.*, 1997). A remanence carried by metallic iron is magnetically not very stable, and thus the observed magnetization is more likely caused by viscous resetting. Viscous magnetization's conform to new field conditions in a relatively short time, up to about 10,000 years. This suggests that the measured normal directions of the ChRM were acquired recently instead of representing a primary TRM. Moreover, native iron is thermodynamically metastable, and usually progressively oxidizes to magnetite (Fe_3O_4), maghemite ($\gamma\text{-Fe}_2\text{O}_3$), and hematite ($\alpha\text{-Fe}_2\text{O}_3$). Since the much more stable ChRM of the older Qianshuihe-Louzhuangzi and Beigou groups is carried by these iron oxides, they may have recorded oxidation during a normal polarity interval any time after burning, rather than expressing a primary TRM.

2.6.3 Thermoluminescence

Three samples of burnt rocks were studied in the laboratory at the University of Helsinki to determine their suitability for TL dating. However, it appeared that the rocks contained very little quartz and feldspar, and moreover probably had lost their TL signal as a result of too high temperatures (Hogne Jungner, pers. comm).

2.6.4 Correlation with data from nearby valleys

Deformed river terraces across growing anticlines in the nearby Kuitun He and Qiurgou He valleys have been dated by Molnar *et al.* (1993). The lowermost terrace of the Kuitun He River at 25 ± 10 m has a Late Glacial - Early Holocene (22-8 ka) ^{10}Be exposure age, whereas one sample from the next higher terrace at 150 ± 20 m yielded a 180 ka ^{10}Be exposure age. This is consistent with deposition of one major terrace each 100 ka glacial-interglacial cycle (Molnar *et al.*, 1993). However, the spacings between

these terraces and those in the Toutunhe River are difficult to compare because uplift rates in the growing anticlines in the Kuitun He and Qiurgou He valleys are estimated to be at least ten times higher as outside them (see below).

2.6.5 Modeling using uplift rates and global climate change as input variable.

Molnar *et al.* (1993) argues that the cyclicity in terrace deposition and dissection is probably tuned to the 100 ka cyclicity of global climate change. This has been tested in several modeling studies on terrace formation (Boll *et al.*, 1988; Veldkamp and Vermeulen, 1989; Veldkamp, 1992). Under favorable conditions of discharge and sediment supply as controlled by the glacial-interglacial cyclicity, river terraces can form under moderate uplift rates. Optimum uplift rates for formation and preservation of 100 ka terrace cycles are around 0.1 mm/y. At lower uplift rates, aggradation exceeds erosion, and no terrain steps are made; at uplift rates higher than that, terraces are ephemeral features likely to be eroded away during the dissectional phases. Taking this into account, and based on the Plio-Pleistocene age of the Beigou terrace at 200 m, terrace steps at 10 m intervals would indeed coincide with the major 100 ka global climate cycles. It would imply as well that the 70 m Gangou/Liugong terraces are around 700 ka old, i.e. considerably older than traditionally considered in Chinese Quaternary stratigraphy (Qiao, 1981).

2.7 Discussion

While still considerable uncertainty exists about the precise age of the coal fires, it is evident that coal fires were a common natural phenomenon throughout the Pleistocene, and probably even in the late Pliocene. Their intimate link with river terraces suggests a relation with the dissectional phases in the glacial-interglacial climate cycle, as only dissection can expose new coal seams to the air leading to spontaneous combustion.

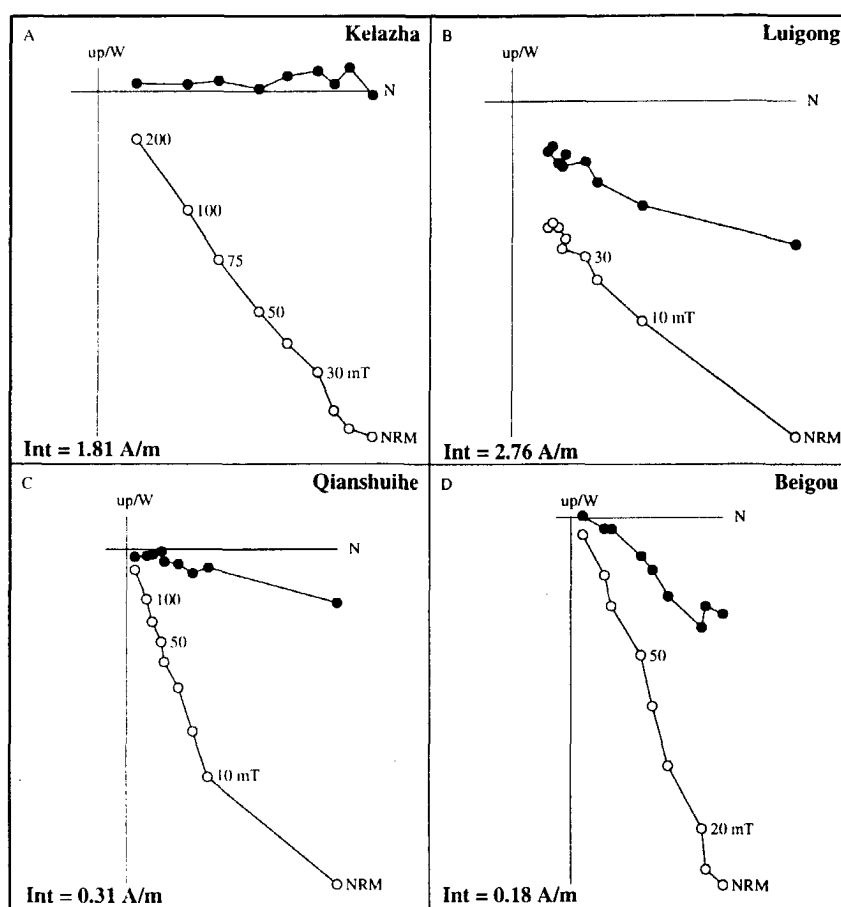


Figure 2-7: Examples of alternating field demagnetization diagrams for samples of the burnt rock groups from the Xinjiang region, showing their normal polarity. Closed (open) symbols represent the projection of the NRM vector end-points on the horizontal (vertical) plane, respectively; values represent alternating fields in mT. Int = initial NRM intensity.

The cyclicity of aggradation and dissection in river valleys upstream from base level is usually governed by variation in sediment output and discharge. In unglaciated terrain's, glacial aridity leads to disappearance of

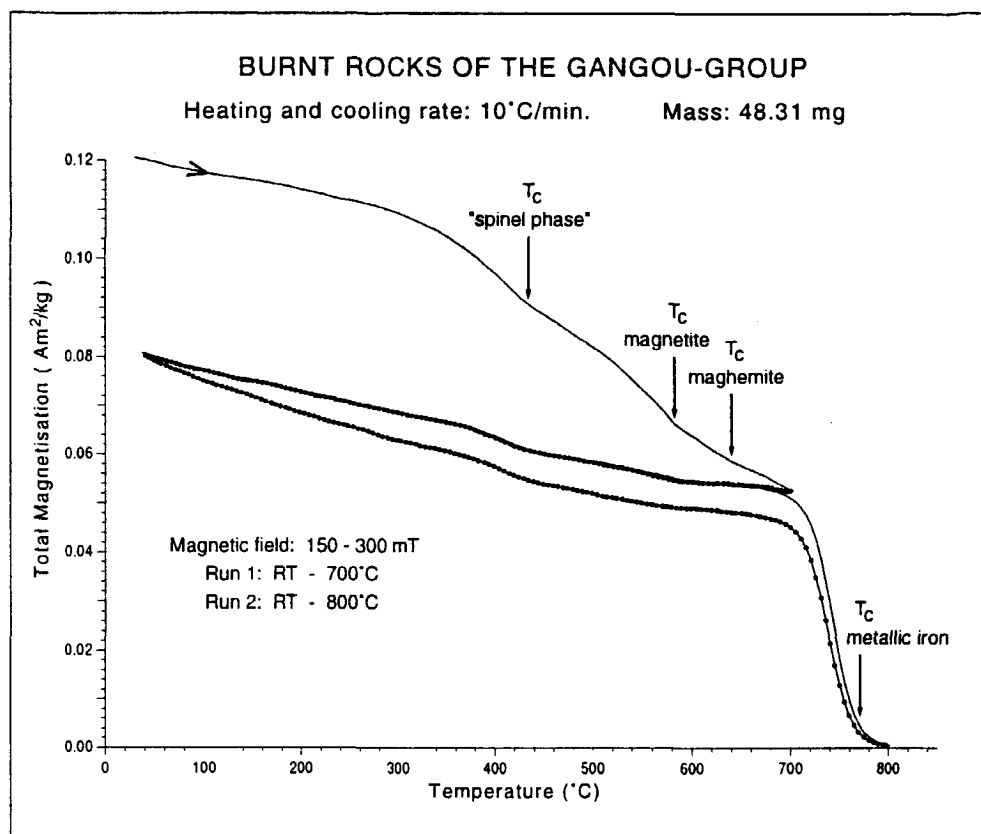


Figure 2-8: Example showing a typical thermomagnetic analysis of burnt rocks from the Gangou group, clearly indicating the presence of metallic iron ($T_c = 770^\circ\text{C}$). Minor inflection points around 440°C , 580°C and 640°C suggest the presence of a magnetic spinel phase, magnetite, and maghemite, respectively.

the protective vegetation cover along slopes, enabling torrential runoff to transport large quantities of unconsolidated sediments towards the river. This leads to aggradation, even under moderate uplift regimes (Veldkamp,

1992). Interglacial moister climates stabilize the slopes and increase discharge of the rivers. Both effects, diminishing load and increasing discharge, lead to marked dissection. This is initially very rapid, as vertical erosion has to compensate for both glacial and interglacial uplift.

In river valleys that drain glaciated terrain, the effect of glacial drainage is superimposed upon this. At maximum glaciation, sediment output is probably limited to seasonal melting, and dissection is unlikely to occur. Rapid deglaciation can lead to massive sediment fluxes, however, which are out of phase with the sedimentation - dissection cycle in unglaciated terrain. Therefore, interglacial dissection might start later than in non-glaciated terrain. On the other hand, if the unroofing of coal seams occurs during interglacial moist climates, spontaneous combustion might be less likely to occur. More precise dating is necessary to resolve this question.

Another problem is how to explain that a burnt-out coal seam can be covered again by gravel, as is the case especially in the Gangou-Liugong exposures. The normal case is that a flood plain, abandoned by the river during dissection, is suspended above the flood plain forever because the dissection had to compensate for glacial uplift as well. The only way to accomplish that, is that burning and collapse of the coal layer causes such a big depression in the river bank, that in a next phase of aggradation the river channel is diverted into it. As the Dacao coal seam is 20 m thick, and the altitude difference between two consecutive terraces is only 10-15 m, diversion into the collapsed roof seems to be plausible. Finally, it is interesting to see whether the amount of coal fires has increased with time (Figure 2-9). The areas of burnt rocks can be calculated from the color infrared photographs. Active coal fire area can be detected from thermal infrared scanner data by their thermal anomalies. The Qianshuihe-Louzhuangzi burnt rocks caused by the regional uplift related to the faulting and folding are the most extensive ones, followed by the Gangou and Zaoyuan coal fires governed by river terrace evolution and climate changes. Active coal fires have a considerable extent in spite of their recent age.

2.8 Conclusions

(1). Spontaneous combustion of coal seams is a natural phenomenon which has occurred repeatedly during the recent geological past. It can occur at any site where deformation, uplift, and dissection lead to exposure of coal to the air. Spontaneous coal fires are especially likely to occur during interglacial dissection of river valleys.

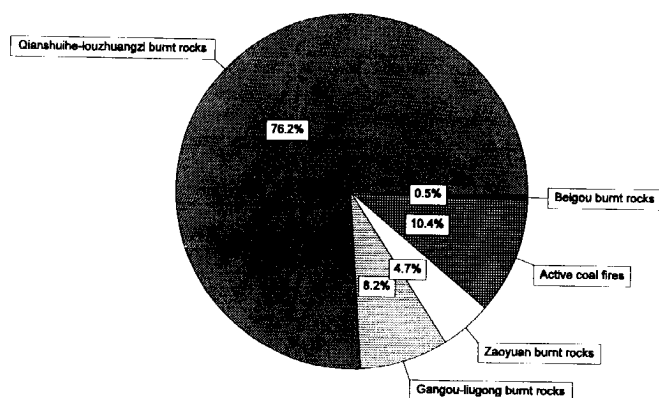


Figure 2-9: Proportion of the areas covered by fossil burnt rocks and active coal fires, as derived from remote sensing imagery.

(2). A large part of burnt rocks identified in remote sensing imagery and field data in NW China appears to be of Pleistocene age. Establishing the contribution of coal fires to the global CO_2 budget should be done on the basis of a combining of remote sensing image, including thermal IR data, and field data, not on the basis of the occurrence of burnt rocks alone.

PART TWO:

ACTIVE COAL FIRES IN NORTHWEST CHINA

CHAPTER 3

SWIR and TIR Remote Sensing --- Some Considerations for the Coal Fire Study*

ABSTRACT

The physical basis of thermal infrared remote sensing for the detection and measurement of coal fires is addressed in order to understand: 1) the characteristics of the thermal infrared data in respect to the spatial, spectral, and radiometric resolution for the detection of coal fires; 2) the methods for surface temperature retrieval and related problems; and 3) other important aspect of the data such as the season and time of data acquisition.

3.1 Introduction

As active coal fires raise the surface temperature, thermal anomalies can be detected by means of thermal infrared remote sensing data. In this chapter, the physical basis of the thermal infrared remote sensing for the detection and measurement of the coal fires is addressed. The characteristics of the thermal infrared data with respect to spatial, spectral, and radiometric resolution are discussed for the detection of coal fires. Also discussed are methods for surface temperature retrieval, the variables of season and time, and other relevant problems.

* This chapter has been published as:

Zhang, X. M., Koopmans, B. N., and Wan, Y., 1995, Detection of spontaneous combustion of coal in Northern China, using thermal remote sensing data. Environmental Assessment of Geological Hazards, Space Congress, Bremen, Germany, May 24-25th, 1995, pp 2-10, Published by European Space Report, Munich, Germany.

Genderen, J. L. van, Cassells, C. J. S., and Zhang, X. M. 1996, The synergistic use of remote sensed data for the detection of underground coal fires - International Archives of Photogrammetry and Remote Sensing, vol. XXXI, part 7: 722-727.

Cassells, C. J. S., Genderen, J. L. van, and Zhang, X. M., 1996, Detection and measuring underground coal fires by remote sensing. Proc. 8th Australian Remote Sensing Conference, Canberra, March, 1996. 90-101

3.2 Thermal infrared remote sensing data

Generally speaking, there are three models for remote sensing (Lillesand and Kiefer, 1994). Depending on the wavelengths of the energy and the purpose of the study, remote sensing can take one of the three basic models. The first class of remote sensing instruments generate their own energy and record the reflection of that energy from the earth's surface; these are the active sensors, such as imaging radar. The second model, similar to our everyday experience, is to record the reflection of the solar radiation from the earth's surface. This form of remote sensing mainly uses energy in the visible and near infrared portion of the spectrum. The third model for remote sensing is to record the radiation emitted from the earth's surface. This emitted energy is strongest in the thermal infrared spectrum. The emitted energy from the earth's surface is mainly derived from short-wave energy from the sun that has been absorbed (solar heating) and then re-radiated at a longer wavelength (the thermal infrared wavelength). Other sources of emitted radiation may be from geothermal energy, heat from steam pipes, power plants, buildings, forest fires, and coal fires. Hence a thermal image, different to the visible and near infrared photograph, show the surface radiant temperature. This is why coal fires can be detected by thermal infrared remote sensing data. However, the emitted radiation received by the sensor is a combination of surface temperatures, surface thermal properties and atmospheric effects.

3.2.1 Thermal infrared remote sensing and atmospheric windows

The atmosphere has an effect on the intensity and spectral composition of the energy recorded by a thermal system. Atmospheric windows influence the selection of the optimum spectral bands within which to measure thermal energy signals (as shown in Figure 3-1). Two windows within the thermal infrared wavelength spectra are in the 3-5 μm and the 8-14 μm range. A number of thermal detectors have been designed to work within these two atmospheric windows. Because a narrow absorption range occurs from 9-10 μm , which is caused by the ozone layer at the top of the earth's atmosphere, satellite thermal IR systems such as TM avoid this absorption range.

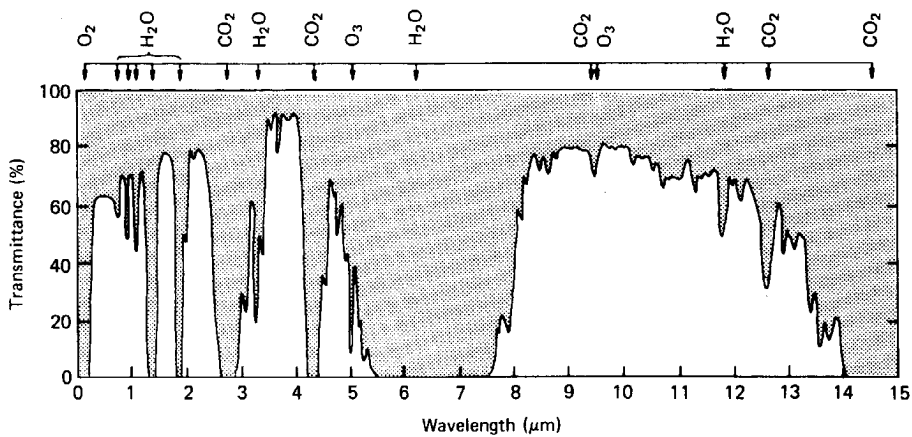


Figure 3-1. Atmospheric absorption of the wavelength range 0 to 15 μm . Note the presence of atmospheric windows in the thermal regions 3 to 5 μm and 8-14 μm (from Lillesand and Kiefer 1994)

Within a given window, the atmosphere intervening between a thermal sensor and ground can increase or decrease the apparent level of radiation coming from the ground. Atmospheric absorption and scattering (attenuated radiance) tend to make the signals from ground objects appear to be colder than they are, and the atmospheric emission(path radiance) tends to make ground objects appear warmer than they are (Lillesand and Kiefer, 1994).

3.2.2 Wien's Displacement Law and coal fire detection

Wien's Displacement Law specifies the relationship between the wavelength of radiation at which radiance is at a maximum, and the absolute temperature (K).

$$\lambda_m = A/T \quad (3-1)$$

where

λ_m = wavelength of maximum spectral radiant exitance, μm

A = 2898 $\mu\text{m K}$

T = temperature, K

When objects become hotter, the wavelength of maximum emittance shifts to shorter wavelengths (Figure 3-2). According to this law, the sensor working within the 3-5 μm window is very sensitive for the detection of objects with temperatures 600 K and above. The sensors working within the 8-14 μm wavelength spectrum are sensible for the detection of objects with a temperature of 300 K.

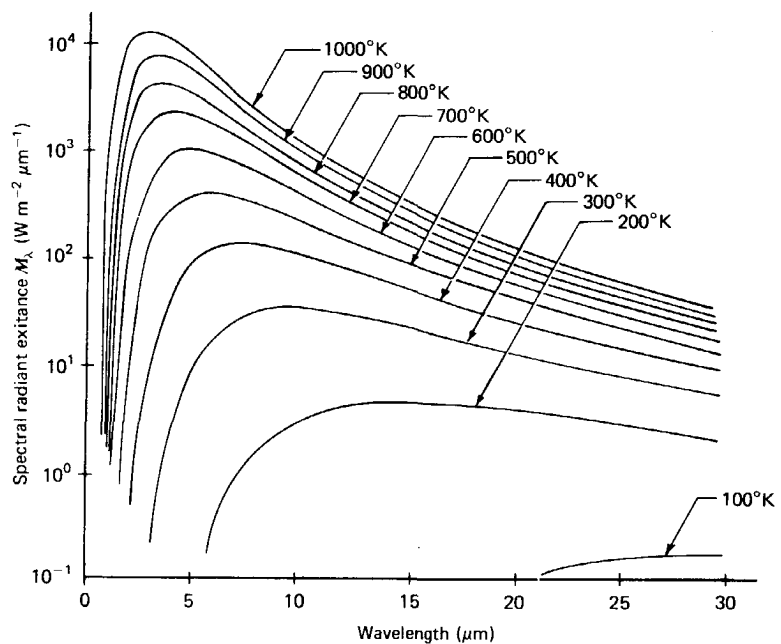


Figure 3-2. Spectral distribution of energy radiation from blackbodies of various temperatures(from Lillesand and Kiefer 1994).

Field temperature measurements have proven that surface and shallow coal fires and the cracked areas above underground coal fires have temperatures above 600 K (Figure 3-3). Underground coal fires usually have surface temperatures around 300 K (Figure 3-4).

Sensors acquiring data from the 3 to 5 μm wave band are more suitable to detect shallow coal fires and the cracked areas above underground coal fires which usually cause intense thermal anomalies. Data from the 8 to 14 μm thermal wavelength region can be used to detect the thermal anomalies caused by the underground coal fires.

A combination of the two sets of data acquired from the two atmospheric windows make it possible to analyze the spatial thermal pattern of the coal fires. In chapter 6, the details of the methods used to analyze the spatial thermal pattern are discussed, including the results by using the 3-5 μm data and 8-14 μm airborne thermal data.

The surface coal fires can cause a great increase of radiance in the Landsat TM band 7 (2.08-2.35 μm) and band 5 (1.55-1.75 μm) working within the SWIR wavelength (see section 5 of this chapter).

3.2.3 Available thermal infrared data from satellite borne and airborne scanners

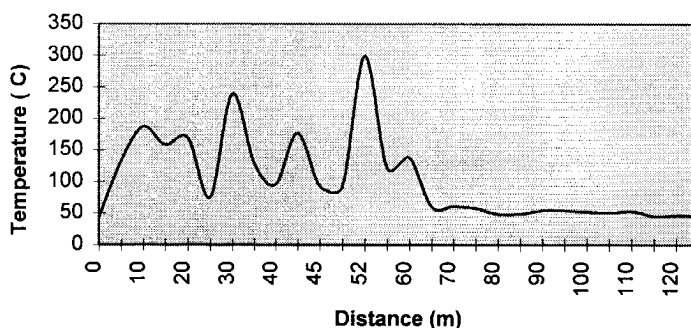


Figure 3-3: Field temperature measurement at 2:00 pm August 17, 1995 of coal fire 143a along dip direction.

Thermal images can be classified according to their working wavelength bands of the sensors into two groups:

1). The sensors are working at 3-5 μm atmospheric window such as NOAA-AVHRR band 3, ERS-1-ATSR-1 band 2, and airborne thermal infrared scanners.

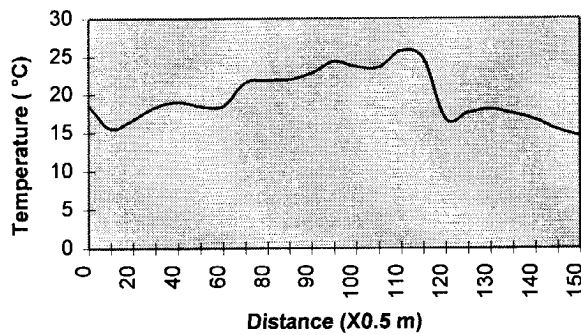


Figure 3-4: Field temperature measurement at 5:30 am August 22, 1995 along road near Sidaogou above underground part of coal fire 143b.

2). The sensors which are working within 8-14 μm atmospheric window including Landsat-TM band 6, NOAA-AVHRR band 4, band 5, ATSR-1 band 3, band 4, and airborne thermal infrared scanners.

As a narrow absorption range occurs from 9-10 μm which is caused by the ozone layer at the top of the earth's atmosphere. Satellite thermal IR systems such as TM avoid this absorption range. Airborne thermal scanner systems working below the ozone layer can work in the whole range from 8 to 14 μm (8-12.5 μm in our case).

3.2.3.1 NOAA-AVHRR data

The Advanced Very High Resolution Radiometer (AVHRR) was designed for meteorological observation. It is quantized to 10-bit radiation resolution

in all channels to allow precise temperature determinations. The channel configurations are: 0.58-0.68 (channel 1); 0.725-1.1 (channel 2); 3.55-3.93 (channel 3);10.3-11.3 (channel 4);and 11.4-12.4 (channel 5). Channels 4 and 5 are used for atmospheric correction for sea surface temperature measurements using the split window method. Channel 3 has been used for detection of forest fires, volcanoes, and industrial heat sources. Mansor et al. (1994) reported the utility of NOAA AVHRR data from Channel 3 for the detection of coal fires in the Jharia coal field, India. According to their work, there exists a good contrast between the coal fire area and its surroundings. Channels 4 and 5 do not show any thermal anomalies. Within our three test areas, we could find several hot spots in Channel 3 data acquired on the 10th, 13th, and 14th of October, 1994. The hottest spot occupying 2 pixels has been observed in Landsat TM band 7 data acquired on the 13th of September 1994. This hot spot is located about 10 km north of the Kelazha area downstream from the Toutunhe River. From ancillary data we know the hot spot is caused by a steel plant. Field work in 1994 also proved the extensive heat source is from the Bayi steel plant in the town of Toutunhe. In the NOAA AVHRR data from band 3 we observed the same hot spot. But in the Kelazha coal fire area in the first test area, no coal fires can be clearly distinguished from the surroundings. The remaining hot spots in the third test area of Sangonghe-Dahuangshan observed in the NOAA data have been proved to be the open fires from caking ovens, whilst in the coal seam areas there were no significant thermal contrast observed on channel 3 data. In the channel 4 and 5 data no thermal anomalies of coal fire can be detected. This study shows that the spatial resolution of NOAA AVHRR data is too low to detect coal fires in our study areas. The study of the ERS-ATSR data which have a similar spatial resolution (1x1 km) gave similar results to the AVHRR data.

3.2.3.2 Landsat-5 TM band 6 thermal data and airborne thermal data

Landsat-5 TM band 6 data are the main thermal data from a satellite-borne sensor with a relatively high spatial resolution (120 m). The capability of the Landsat-TM thermal data and the temperature calculation are studied in Chapter 5.

The Characteristics of the airborne data and their use for the study of coal fires are addressed in Chapter 6.

3.3 Thermal anomalies—sources and influencing factors

3.3.1 Surface energy budget and atmospheric correction

It is known from field work carried out in 1994 and 1995 that there are four possible causes of thermal anomalies within the study areas. These are: coal fires, solar heating of the ground, abnormal geothermal fluxes, and human activities. Anomalous geothermal flux is a very small effect and can generally be neglected. Heat sources such as power stations and steel-works can produce significant hot spots but their positions are usually well-known. Thermal anomalies due to solar heating of the ground are not so readily identifiable and are the most significant source of confusion of fire and non-fire thermal anomalies in the study areas.

To obtain the land surface temperature from satellite data with some reliability and accuracy, it is necessary to apply corrections to the brightness temperatures for atmospheric effects and the emissivity of the land surface. According to Bartolucci et al. (1988) under clear atmospheric conditions, the atmospherically attenuated target radiance is compensated by path radiance emitted by the atmospheric constituents. The atmospheric correction, however, can not improve the detection of the coal fire for the enhancement of the contrast of the thermal anomalies between the coal fire area and the background areas. This is not surprising because an atmospheric correction does not enhance the contrast.

3.3.2 Solar heating and the time and season of the thermal remote sensing data

Diurnal temperature curves (Figure 3-5) show that at predawn time (about 6:00, local solar time) objects have the lowest temperature and coal fire areas usually have a relatively stable higher temperature. So, remote sensing data received at predawn or after the sunset are more valuable for coal fire detection because of the significant temperature contrast between the fire areas and the background areas. The variations in the curves of the diurnal

temperatures of materials also show the different thermal properties of the different objects. Soil and coal have a low heat inertia and a greater diurnal variation of surface temperature than rocks. Watson (1975) has shown that in the forenoon (09.00-10.00h) and afternoon (about 16.00h), there is no differential effect owing to thermal inertia on surface temperature. Therefore, these timings of thermal cross-over for Landsat possess the potential for detecting geothermal areas of anomalous heat gain/loss.

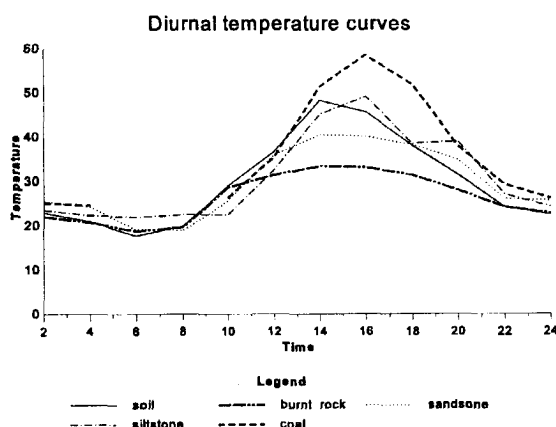


Figure 3-5 Diurnal Temperature curves of typical objects in coal fire area

The topographic influence on solar heating is a key factor which influences the image brightness in rugged terrain. The uneven solar heating is the most important source that causes confusion with coal fires. A pre-dawn (night-time) design of an airborne flight or acquiring the night-time satellite data can by-pass the solar heating problem. For the daytime thermal data, a map of solar illumination created according to the DTM and the sun position at the time of Landsat acquisition is used for the adjustment of the thermal data. Then the fire areas become more prominent. The details of the method for the correction of the daytime thermal data are studied in chapter 4. The comparison of two scenes of daytime TM band 6 data acquired in June and September show a greater contrast for June data than for the September data due to the overall higher temperatures during the latter month. Hence data acquired during the summer season should be avoided.

3.4 Landsat-5 TM SWIR data and surface coal fire temperature and size measurement

3.4.1 Physical foundation for the temperature derivation from the TIR and SWIR data

Planck's equation relates spectral radiance L_λ and temperature

$$L_\lambda = \frac{\epsilon c_1 \lambda^{-5}}{\pi \left[\exp \left(\frac{c_2}{\lambda T} \right) - 1 \right]} \quad (3-2)$$

where $C_1 = 3.742 \times 10^{-16} \text{ Wm}^2$, $C_2 = 0.0144 \text{ mK}$, $\lambda =$ wavelength in m, $\epsilon =$ emissivity and $T =$ temperature in K. Equation can be rearranged to give

$$T = \frac{c_2 \lambda^{-1}}{\ln \left[\left(\frac{\epsilon c_1 \lambda^{-5}}{\pi L_\lambda} \right) + 1 \right]} \quad (3-3)$$

let

$$K_1 = \frac{\epsilon c_1 \lambda^{-5}}{\pi} \quad (3-4)$$

$$K_2 = \frac{C_2}{\lambda} \quad (3-5)$$

then , equation become:

$$T = \frac{K_2}{\ln \left(\frac{K_1}{L_\lambda} + 1 \right)} \quad (3-6)$$

For blackbody ($\epsilon=1$), the K_1 and K_2 values are listed in Table 3-1 by assigning the λ as the midpoint in the band pass of band 5, band 7, and band 6 using equations (3-4) and (3-5). Care should be taken, as the

effective wavelength depends on both the filter transmission characteristics of each sensor and the radiant temperature of the surface. However, the uncertainties of pixel-integrated temperature is less than 10 K (Rothery et al., 1988, Oppenheimer et al. 1993).

Table 3-1: The calibration factors for the temperature calculation. (*from Barker etc. 1986)

	TM band 5	TM band 7	TM band 6	Units
Central wavelength	1.65×10^6	2.215×10^6	11.45×10^6	m
K_1	973845.28	223401.30	60.776*	$\text{mWcm}^{-2}\text{sr}^{-1}\mu\text{m}^{-1}$
K_2	8727.27	6501.13	1260.56*	K

3.4.2 Dual-band temperature calculation by using Landsat-5 TM band 5 and band 7 data

The TM SWIR data from band 7 and band 5 covers the wavelength range of 2.08-2.35 and 1.55-1.75 μm respectively. Some high temperature surface fires can even cause the greatest increase of radiance on the imagery of bands 7 and 5. Due to the different response of the radiation for a sub-pixel, the pixel-integrated brightness temperatures derived from band 7 and band 5 are different. The size and temperature of the coal fires which usually cover only sub-pixel areas can be retrieved by the so called dual-band method.

Unlike the thermal infrared region of the spectrum where there is negligible reflected solar radiation and measured radiance is virtually all thermal in origin, thermal radiance at shorter wavelengths is combined (in daytime data) with solar radiance which has been reflected by the surface and scattered by the atmosphere. To correct it, the neighbor non-thermal pixels are used to subtract from the thermal anomaly pixels.

Spectral radiance measured by the sensor can be converted to a pixel brightness temperature using the inverse of Plank's formula. Since this temperature will be an integral of all the temperature sources which occupy the pixel, this will give a pixel-integrated temperature. For surfaces where temperatures are fairly uniform over large areas, pixel-integrated temperatures approximate the true surface temperature.

Table 3-2. The pixel values in TM band 7 , data received on November 8, 1995

	1410	1411	1412	1413	1414	1415	1416	1417	1418	1419 (Col. No.)
Line No.										
370	35	32	23	23	22	19	20	21	20	18
371	25	16	23	16	19	24	26	25	20	21
372	27	31	15	17	39	53	28	20	17	20
373	29	36	0	75	246	245	65	12	17	17
374	31	31	39	168	187	58	25	22	17	19
375	32	37	29	10	229	162	21	17	18	19
376	35	41	36	29	87	71	24	20	18	20
377	34	39	36	36	25	25	23	20	18	23
378	45	43	36	26	23	23	21	19	22	23
379	47	48	41	27	23	22	23	20	21	24

However, in areas of coal fires uniform temperatures are unlikely. Instead, temperatures will vary greatly over a small area. For example, a 30m by 30m pixel will contain a variety of temperature sources and the resulting pixel-integrated temperature will be meaningless since it will fail to identify the true variation in surface temperature.

In the areas of surface fires and shallow fires with open cracks, the thermal surface occupying the pixel will be made up of two distinct components: a hot fire or crack with a component of molten rocks at temperature T_f occupying portion P of the pixel, and a cool background component at temperature T_b occupying the remaining portion of the pixel $(1-P)$.

Using the dual-band method proposed by Dozier (1981) and Matson and Dozier (1981), the temperature and size of the two sub-pixel heat sources can be calculated. If any one of the three parameters T_f , T_b , or P is known, then the method allows the remaining two parameters to be calculated by graphical or numerical solution by the following simultaneous equations:

Table 3-3. The pixel values in TM band 5, data received on November 8, 1995

	1410	1411	1412	1413	1414	1415	1416	1417	1418	1419 (Col. No.)
Line No.										
370	52	46	32	28	31	30	31	43	40	38
371	52	48	32	24	30	32	33	38	38	38
372	56	23	34	26	23	24	34	31	33	32
373	42	39	47	50	115	100	33	26	28	34
374	42	50	33	94	97	40	30	33	25	31
375	45	45	49	37	100	89	36	38	20	28
376	46	46	58	49	58	54	39	38	32	31
377	45	52	64	53	43	34	36	38	32	29
378	48	58	63	51	39	37	34	37	32	33
379	75	78	69	59	38	37	39	39	32	32

Table 3-4. Temperature (°C) and areas(m²) of coal fires derived from band 7 and band 5 data using dual-band method.

	1411	1412	1413	1414	1415	1416 (Col. No.)
Line No.						
370						
371						
372						
373				838/1.74	716/3.5	
374			880/0.9	842/1.23		
375				751/2.61	840/1.08	
376				602/2.25		
377						
378						

$$Li = P Li(Tf)+(1-P)Li(Tb) \tag{3-7}$$

$$Lj = P Lj(Tf)+(1-P)Lj(Tb) \tag{3-8}$$

where Li and Lj are the at-satellite spectral radiance in Channels i and j (if atmospheric attenuation can be ignored), *P* is the portion of the pixel occupied by the fire or hot cracks. Li(Tf) and Lj(Tb) are the spectral

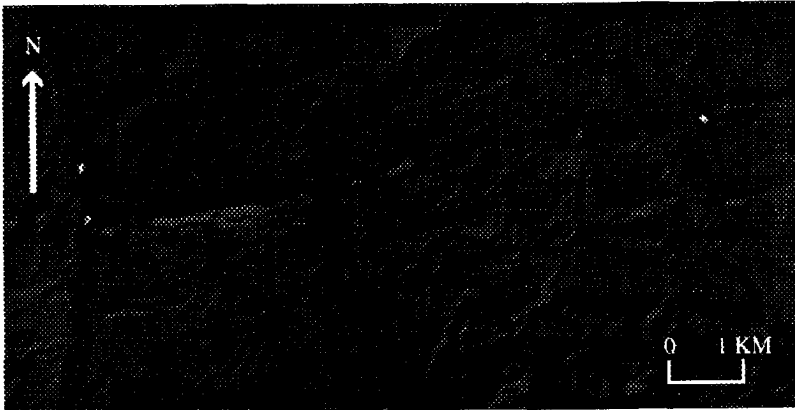


Figure 3-6. Surface coal fires recognized from Landsat-TM band 7 image.

radiance for the fire and crack areas in channel i and j , and $L_i(T_b)$ and $L_j(T_b)$ are the spectral radiance for the background in channel i and j .

By using the SWIR data of band 7 and band 5 we can calculate the size and temperature of the coal fire and crack areas. The formulas become:

$$L5 = PL5(T_f) + (1 - P)L5(T_b) \quad (3-9)$$

$$L7 = PL7(T_f) + (1 - P)L7(T_b) \quad (3-10)$$

In the third test area of Sangonghe-Dahuangshan area, four surface coal fires are observed in band 7, and three of them are observed in band 5 data (Figure 3-6 and Figure 3-7). The Landsat data were acquired on November 8, 1995. In the band 7 data coal fires are bigger and clearer. Figure 3-6 and Figure 3-7 show the different spectral response of the thermal radiance.

Table 3-2 and 3-3 list the DNs of a subimage from Landsat TM band 7 and band 5. The bold pixels are thought to be the coal fire area. Twenty-six was subtracted from each pixel value in table 2 to reduce the reflectance of the solar radiation. While in Table 3-3, 44 was subtracted. Table 3-4 provides the calculation results which show the sub-pixel temperatures of the surface coal fires and the portions of the coal fires. The thermal radiometers used during the field work were limited to a temperatures of 300 °C. The sizes of the coal fires calculated from the dual-band method fit the field measurements quite well.

3.4.3 The spectral and spatial resolutions of remote sensing data concerning measurement of the temperature and size of the coal fires.

In the known coal fire areas, based on field observation data, there are two main factors which cause the size of coal fires in the remote sensing imagery to be exaggerated; these are the sub-pixel coal fires and the optical blurring phenomena. When the area of coal fires are delineated by the threshold method, an area of a full-pixel is taken as the real size of the coal fire. The small fires only occupying a portion of the pixel are therefore exaggerated. Thermal imagery from Landsat-TM band 6 (120×120m) usually exaggerates the true areas. On the other hand, the coarseness of the spatial unit conceal small fires at the same time.

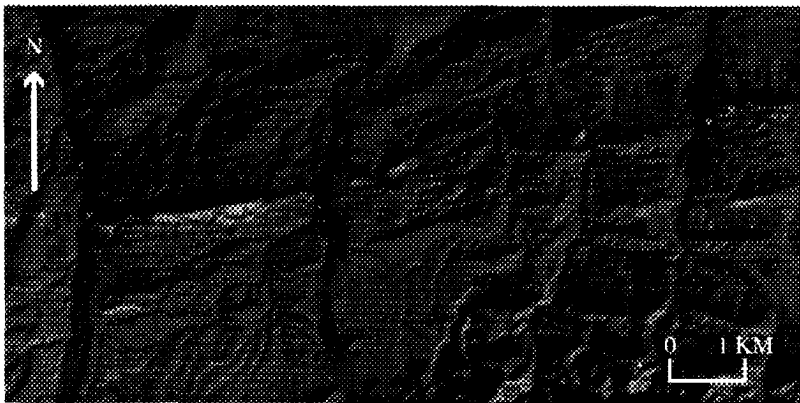


Figure 3-7. Surface coal fires recognized from Landsat-TM band 5 image

As the hot spots contribute greatly to radiance in band 7 and 5 imagery, a small fraction of a coal fire can cause a great increase in the radiance of the whole pixel and make it resemble a coal fire.

Although the normal size of a Landsat TM band 1-5 and band 7 pixel is 30 m by 30 m, the area of terrain over which the radiance is collected to produce each image pixel is actually somewhat larger (33-46m) because of

the optical characteristics of the system (Rothery et al., 1988). It is a reasonable approximation to assume that the area sampled by a TM "30 m" pixel is actually about 40 m across. The centers of the adjacent pixels are 30 m apart, and there is a 10 m wide zone in between from where adjacent pixels are both sensitive to radiance. Overlap of IFOVs of adjacent pixels and the temporary downscan damage seen in most band 5 and 7 data are likely to result in an overestimation of the size of the anomalies. For the 120m pixel from band 6, the effective instantaneous field of view appears to be about 140m across. The optical blurring phenomena then exaggerates the fire areas in band 6 data also.

3.5 Conclusions

- 1). Uneven solar heating is the most important source for the confusion of the coal fires in daytime thermal infrared imagery. A correction for uneven solar heating is necessary.
- 2). Landsat-TM band 7 and 5 data are useful for the detection of surface coal fires. The dual-band method can be adopted for the temperature estimation of sub-pixel size surface coal fires.
- 3). NOAA AVHRR data with 1km×1km spatial resolution is too coarse for coal fire detection and hence not a practical data set for coal fire monitoring.

CHAPTER 4

Solar Heating Simulation for the Detection of Coal Fires *

ABSTRACT

In the mountainous areas, uneven solar heating is the main source of confusion for the coal-fire induced thermal anomalies for daytime thermal infrared remote sensing data. The solar heating was modeled by using a Digital Elevation Model (DEM) which takes into account the azimuth and altitude angle of the sun and the passing time of Landsat. This simulated image was used for the thermal remote sensing data to suppress the thermal anomalies of slopes facing the sun and to enhance the coal fire areas.

4. 1 Introduction

Detection is the first step for the measurement, monitoring, and extinguishing of coal fires. Daytime Landsat TM thermal data of band 6 are increasingly being used for the detection and monitoring of the coal fires. One of the main problems, however, is solar heating. The topographic effect of it causes uneven solar heating and makes detection difficult. Justice et al. (1981) defined the topographic effect as the variation in radiance from inclined surface compared to radiance from a horizontal surface as a function of the orientation of the surfaces relative to the light source and the sensor position. The topographic effect on the Landsat TM and MSS reflective data of rugged terrain has been studied by several authors (Holben and Justice 1979, 1981, Kawata et al. 1988). Several studies have demonstrated that the need to consider topographic variations when undertaking Land cover classification for areas of mountainous terrain (Anuta 1976, Strahler et al. 1978, 1979).

* This chapter has been published as:

Wan Y. Q and Zhang X. M, 1996, Using a DEM to reduce the effect of solar heating on Landsat TM thermal IR images and detection coal fires, Asian-Pacific Remote Sensing and GIS Journal, Vol 8, Number 2, 65-72.

The phenomenon of topographic effect in a daytime thermal infrared image are similar to those in a reflective spectral band image and is dependent on the irradiance upon a land surface for a given incident solar radiation. The topographic effect, however, influences the thermal infrared remote sensing data and reflective data differently (Ricotta and Avena, 1997). For the thermal infrared data, the land surface receives the solar radiation in the short-wave region (raising surface temperature) and then emits it in the long-wave region. A slope facing the sun receives more solar radiation and is therefore brighter and warmer than a shaded slope. As a result, the illuminated slope appears brighter in both reflective spectral and thermal images (Liu and Moore, 1997). Although the use of night-time TM day or airborne data can easily bypass this problem, daytime thermal data, especially from Landsat TM, are used because of lower cost and easier availability.

A Digital Elevation Model (DEM) was used to module the uneven solar heating and to generate a simulated solar heating image. Combining the simulated solar heating image and the daytime Landsat TM thermal data, the thermal anomalies caused by the coal fires were enhanced. These results were confirmed by the night-time airborne thermal infrared data.

4. 2 The methodology to reduce the uneven solar heating effect

The method presented in this chapter consists of three steps: (a) modeling the relative intensity of solar radiance for each pixel (120m×120 m) of the image using a digital elevation model; (b) simulating a solar heating image; and (c) adjusting the day time Landsat TM thermal data with the simulated image.

4.2.1 The solar radiance reaching the ground surface Ground heat radiance

For the TM band 6 data, the pixel values depend on the atmospherically attenuated thermal radiance of the ground surface. Radiance is a function of surface temperature, unknown surface spectral emissivity, and absorption and emission of the atmosphere (Yang et al., 1988). The spectral radiance $L_{\lambda T}^{BB}$ ($\text{wm}^{-2} \text{sr} \mu\text{m}^{-1}$) for a perfect blackbody at a constant temperature T can be calculated with Planck's law:

$$L_{\lambda T}^{BB} = C1 / \{\lambda^5 (e^{C2/\lambda T} - 1)\} \quad (4-1)$$

where

$$C1 = 2\pi h c^2 = 3.7415 \times 10^{-16} \text{ (wm}^2\text{μm}^{-1}\text{)},$$

$$C2 = hc/K = 1.43879 \times 10^4 \text{ (μm K)}.$$

The radiance $L_{\lambda T}^{GB}$ for a grey body is modified by the spectral emissivity $\epsilon_{\lambda T}$

$$L_{\lambda T}^{GB} = \epsilon_{\lambda T} L_{\lambda T}^{BB} \quad (4-2)$$

The radiance recorded by the sensor on Landsat is comprised of the following three components:

$$L_{\lambda} = \tau_{\lambda} L_{\lambda T}^{GB} + \tau_{\lambda} r_{\lambda} L_{\lambda d} + L_{\lambda u} \quad (4-3)$$

where

$L_{\lambda d}$ is the downward radiance from the sky to the ground surface of a ground object.

r_{λ} is the reflectance of the surface.

$L_{\lambda u}$ is the upward radiance due to the self-emission of the atmosphere.

τ_{λ} is the atmospheric transmission.

In a small area such as our study area in Toutunhe, the $L_{\lambda d}$, $L_{\lambda u}$, and τ_{λ} are the same. For Landsat TM band 6 pixel, it covers an area of $120\text{m} \times 120\text{m}$ at ground. Within this area, the reflectance's are different due to the inhomogeneous ground covers. So for each pixel, the r_{λ} in Equation 4-3 may be different. However, the $L_{\lambda d}$ is very small when comparing the $L_{\lambda T}^{GB}$. The first item in Equation 4-3 is the most important one for the detection of the coal fires.

Under similar environmental conditions of ground absorptivity, thermal inertia, soil moisture, wind strength and direction, terrain slope and aspect, the thermal radiance should be the same. At any given point, taking the temperature at a non-coal fire area as $T1$, the temperature at a coal fire area as $T2$ and using the equation in 4-3, the difference in thermal radiance caused by a coal fire is:

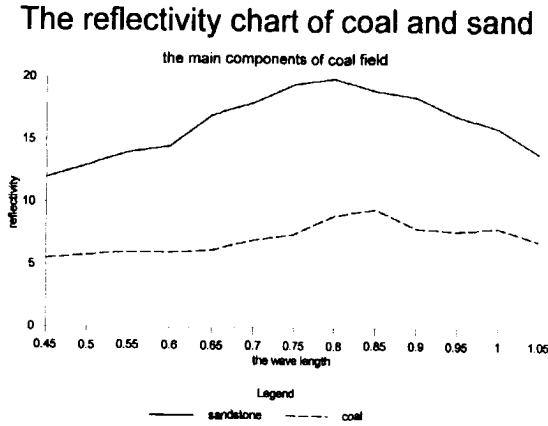


Figure 4-1 The reflectance of the main rocks in the test area.

$$\Delta L_{\lambda} = \tau_{\lambda} L_{\lambda T2}^{GB} - \tau_{\lambda} L_{\lambda T1}^{GB} > 0 \quad (4-4)$$

To detect a coal fire it is necessary to find an area with higher ΔL_{λ} . Temperature T1 during daytime depends on solar radiance. Uneven solar heating due to topography variations is the most important factor that causes confusion when interpreting coal fires from the remote sensing data. With DEM, the relative solar heating intensity can be calculated.

4.2.2 Surface radiance from sun with respect to a DEM

Solar radiance on the ground surface depends on the terrain undulation and the sun's position. If the sunlight is perpendicular to a surface, more luminance reaches the surface. Dave and Bernstein (1982) and Yang et al. (1988) pointed out that changes in luminance over a terrain is a function of terrain slope and azimuth and altitude angle of the sun. Supposing that solar radiance is $L_{\lambda s}$ over the ground and the incidence angle is θ , then on a flat surface the radiance $L'_{\lambda s}$ is:

$$L'_{\lambda s} = L_{\lambda s} \cos \theta \quad (4-5)$$

If $\theta = 0^\circ$, then the surface has direct sunlight and the strongest solar radiance, thus $L'_{\lambda s} = L_{\lambda s}$. When θ is 90° , then $L'_{\lambda s} = 0$, and no radiance is reaching the surface. θ is a function of terrain undulation and zenith and azimuth angles

of the sun. With a digital terrain model, $\cos\theta$ can be calculated with the following formula (Yang Kai et al., 1988):

$$\cos\theta = \sin\theta_z \sin\tau \cos(\alpha_s - \alpha_n) + \cos\theta_z \cos\tau \quad (4-6)$$

where θ_z is the zenith angle of the sun. If we calculate the altitude angle (α), then:

$$\theta_z = 90^\circ - \alpha \quad (4-7)$$

where α_s is the azimuth angle of the sun;

τ is the slope angle at a given ground location and

α_n is the aspect angle at that ground location. Both τ and α_n can be derived from the digital terrain model.

4.2.3 Calculating the altitude angle (α) and azimuth angle (α_s) of the sun

The sun's position is determined by two terms, altitude (α) and azimuth (α_s), both of which vary as a function of time of day (Rees, 1990). Let ϕ be the latitude (measured north of the equator), Δ the longitude (measured east of the Greenwich Meridian), and D the number of days (counted from 1 January of every year), then:

$$\alpha = \sin^{-1} \{ \sin\delta \sin\phi + \cos\delta \cos\phi \cos H \} \quad (4-8)$$

$$\alpha_s = \cos^{-1} \{ (\sin\delta - \sin\phi \sin\alpha) / (\cos\phi \cos\alpha) \} \quad (4-9)$$

where δ is the sun's declination, approximately expressed as:

$$\delta = \sin^{-1} \{ 0.3987 \sin(0.986[D-80]) \} \quad (4-10)$$

and H is the hour angle, expressed as:

$$H = 15T - 180 + \Delta + E \quad (4-11)$$

The equation of time expresses the difference in position between the true sun and the fictitious mean sun which appears to move uniformly across the sky. It is given as:

$$E=2.47\sin\{1.97(D-80)\}-1.92\sin\{0.986(D-3)\} \quad (4-12)$$

All the angles mentioned, with the exception of E, (a trigonometrical ambiguity occurs when calculating the inverse Cosine in equation 4-9) should be expressed in degrees. It is resolved by noting that A and H have the same sign.

4.2.4 Calculating the slope angle (τ) and aspect angle(α_n)

The slope angle (τ) and the aspect angle (α_n) at a given ground location depends on terrain slope and aspect. These angles can be calculated using values from the surrounding digital terrain model pixels which have the same size as those of the TM images. With the adjacent terrain elevation values of pixel of d (Figure 4-2), τ and α_n can be calculated as:

d1	d2	d3
d4	d	d5
d6	d7	d8

Figure 4-2. Numbering of pixels surrounding d

$$\tan \tau = \sqrt{\left[\frac{N_x}{N_z}\right]^2 + \left[\frac{N_y}{N_z}\right]^2} \quad (4-13)$$

$$\tan \alpha_n = (N_x/N_z)/(N_y/N_z) \quad (4-14)$$

where

$$N_x/N_z = \{[d1+d4+d6]-[d3+d5+d7]\}/2R \quad (4-15)$$

$$N_y/N_z = \{[d6+d7+d8]-[d1+d2+d3]\}/2R \quad (4-16)$$

d1, d2, d3, d4, d5, d6, d7, d8 indicate the elevation value of the eight neighboring pixels, and R indicates the resolution of the DEM.

4.2.5 Extraction of thermal anomalies from TM band 6 by simulating the radiance image

To simulate a radiance image with the DEM, we can use the following formula:

$$L_{\lambda T1}^{GB} = k1 \cdot L_{\lambda s}' \quad (4-17)$$

$k1$ is a constant affected by albedo, thermal inertia, moisture, wind, and atmosphere. It is not feasible to measure $k1$ for every point in a vast area and therefore it is assigned a constant value. This will cause errors, but the simulated image can still show us the comparative difference of radiance.

TM band 6 was taken as $L_{\lambda T2}^{GB}$, and $k1$ set at 255 because pixel values in TM band 6 vary from 0 to 255. Using the equation 4-4 we can produce a thermal radiance image showing anomalies.

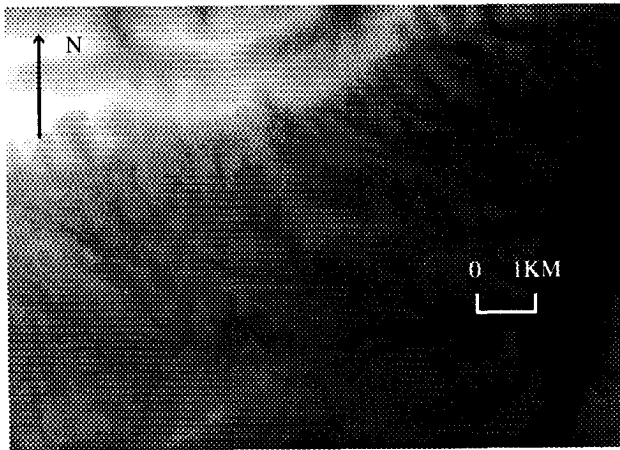


Figure 4-3 Digital elevation model (DEM) of area of the Kelazha anticline. The brightness indicates the elevation.

4.3 Application of the method

In order to test the results, we selected a mountainous area of Kelazha anticline, within the first test area of Toutunhe, where the coal fires are quite large. There are two advantages to this, one is to determine whether the simulated thermal infrared radiance

image is useful and the other is to check whether the coal fires can be distinguished on a Landsat TM thermal infrared images. The test area extends from latitude $43^{\circ} 40'$ to $43^{\circ} 48'$ and longitudes $87^{\circ} 06'$ to $87^{\circ} 14'$. The difference in elevation from the highest to the lowest point is about 800m. The digital elevation map of the test area is displayed in Figure 4-3. The highest points are located northwest of the area with the main sloping

direction towards the southeast. A three-dimensional view of the test area is provided in Figure 4-4.

Most of the area is covered by bare-rocks.

Field investigations show that the main components of the coal measure strata are Jurassic sandstone and siltstone with light grey and dark grey tones.

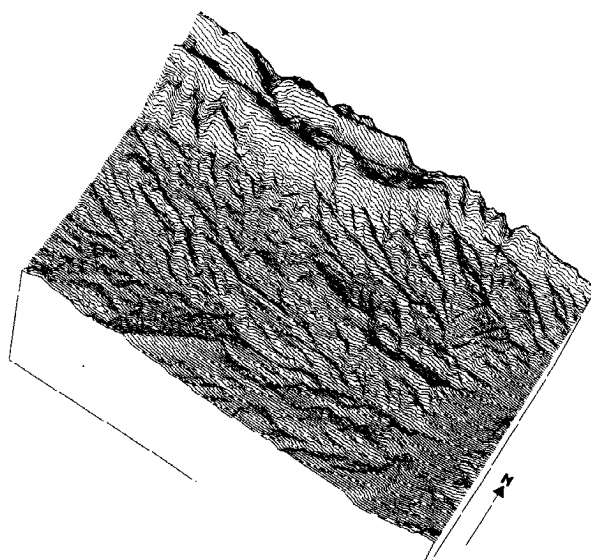


Figure 4-4 Three-dimension topography perspective view of Kelazha area from Southeast direction

An interpretive map of the test areas showing the distribution of geological units and structures is shown in Figure 4-5. Coal fires are located in both wings of the Kelazha anticline. In the legend of the map, F1 represents extinguished coal fire areas where the caprock and the bedrock were baked, and F2 means active coal fires.

The TM image of the test area was acquired on the 14th of September 1994. Using the equation in (4-8) to (4-11), the sun's position was calculated. The azimuth of the sun at 10:02 a.m. is $127^{\circ}25'$, and the altitude angle is $42^{\circ}30'$.

Using the DEM and equation (4-6), $\cos\theta$ was calculated for every pixel of the image. When $\cos\theta$ takes a negative value, it corresponds to a shadowed area and therefore the $L_{\lambda T1}^{GB}$ can be assigned the value 0. The equation in (4-5) becomes:

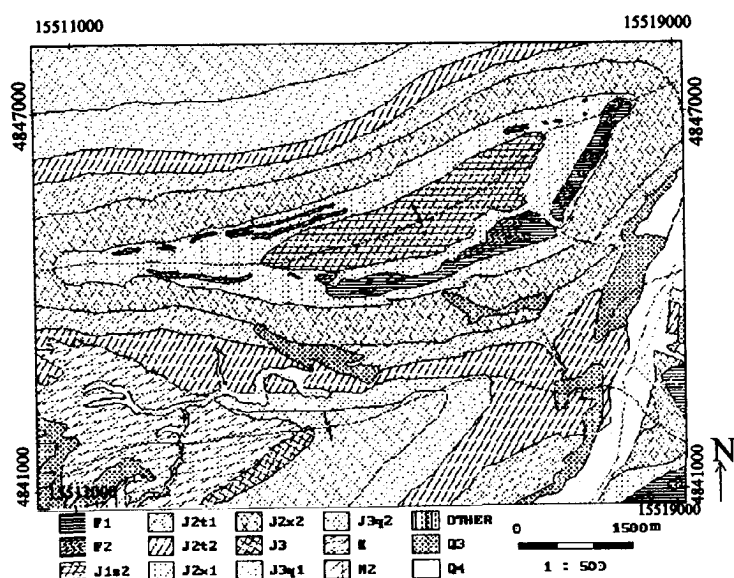


Figure 4-5 Geological map of Kelazha area



Figure 4-6. The simulated solar heating image. The brightness of the image represents the incident radiation from the sun with respect to the azimuth and altitude angles and the topography.

$$L'_{\lambda s} = \begin{cases} L_{\lambda s} \cos \theta & \text{if } \cos \theta > 0 \\ 0 & \text{if } \cos \theta \leq 0 \end{cases} \quad (4-18)$$

$L_{\lambda T1}^{GB}$ can be stretched from the initial values between 0 and 1.0 to 0 to 255. The pixel values are then distributed within the whole dynamic range of the video monitor and the difference in radiance becomes much clearer. The simulated radiance image is shown in Figure 4-6. Brightness indicates the strength of solar radiance with the high value.

4.4 Results

A portion of the TM band 6 image, which was geometrically corrected to correspond to the DEM shown in Figure 4-3, is shown in Figure 4-7. Many coal fires were occurring according to the field investigations and the geological interpretation. Pixels with the highest values (stronger thermal radiance) correspond either to fires or to ground surfaces facing the sun.

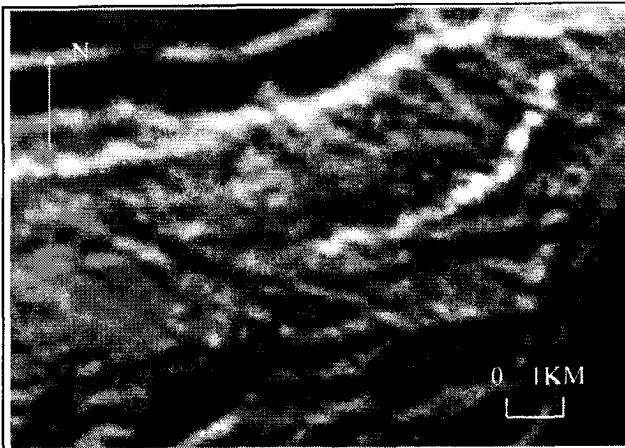


Figure 4-7. Geometrically corrected Landsat-TM image acquired on September 14, 1994, which covers the same areas as Figure 4-5 and Figure 4-6.

The image was obtained by subtracting the simulated illumination image (Figure 4-6) from the TM band 6 image (Figure 4-7) and is provided in Figure 4-8. Most of the pixels on the image that have the strongest solar illumination become dim, and pixels located in coal fire areas remain bright.

The geometrically corrected airborne nighttime thermal infrared image of the same area obtained on the 30th of July 1992 is shown in Figure 4-9. According to field investigations and image interpretation, the brighter areas

found on Figure 4-8 are highly correlated to those found on Figure 4-9, as expected.

4.5 Discussion

4.5.1 The effect of solar heating history

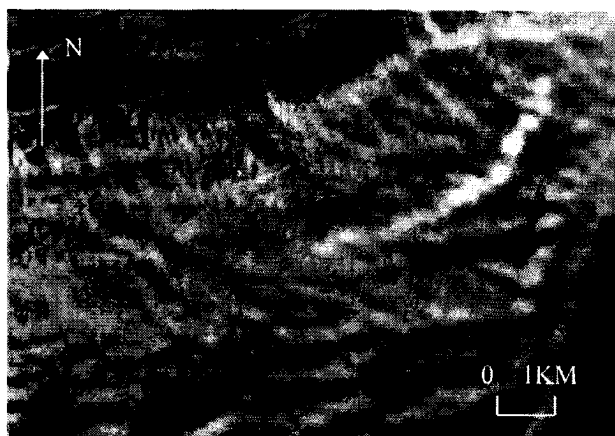


Figure 4-8. The resultant image of subtracting the simulated one from Landsat-TM band 6. Note the coal fire areas have been enhanced.

In Figure 4-8, there are still some brighter areas that do not correspond to coal fires. The surface temperature is also affected by the length of the solar heating. Figure 4-10 shows the variation of temperature from 06:00 hours to 18:00 hours on three main types of rock: sandstone, coal layer, and shale. It is clear that from 08:00 to 10:00 hours, heat is

accumulated and the temperature of all rock types rises rapidly. Therefore, the longer the exposure to sunlight in the morning, the higher the temperature of the ground surface (Guan, 1989).

In Figure 4-8, all the bright areas without coal fires are located on special hillsides where the ground surface can get sunlight from 05:50 hours (time of sunrise on the 14th of September 1994 at latitude 44° and longitude 87°) such as point A in Figure 4-11 (a). In some other points, such as point B in Figure 4-11 (b), the sun shines only from 08:30 (the verification of the azimuth and altitude angle of the sun is shown in Figure 4-12). Consequently, at the time of satellite overpass, point A had already been illuminated by the sun for nearly four hours, whereas point B had only been getting less than two hours of sunshine. In addition the temperature at point A is higher than that at point B. So, if the time of exposure to sunlight had

been taken into account, the resulting simulated image would be more accurate

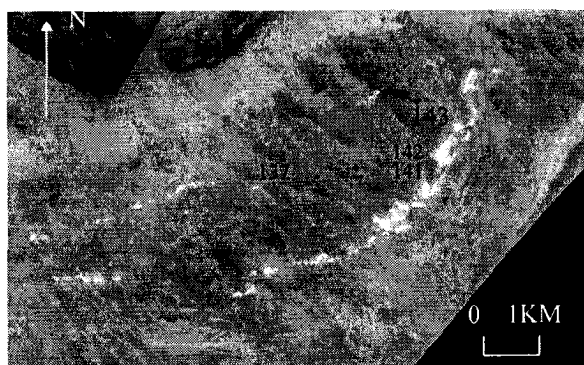


Figure 4-9 The geometrically corrected airborne night time thermal infrared image scanned on July 30, 1992, which was merged from two flight lines. The white spots on the image are the fires which were proved by the field work.

4.5.2 The precision of the DEM

Equation 4-13 and 4-14 indicate that the elevation of the surrounding pixels determines the value of aspect and slope angle of a given pixel. Tests show that if the DEM is poor in precision, then there must be some confusion on the simulated radiance image.

Also, it is extremely difficult to digitize every contour line in very steep areas and some were omitted. DEMs produced from stereoscopic SPOT images should have higher quality.

4.5.3 Other effects

Singh's (1984) research shows that on the ocean surface, the emissivities at wavelengths between 11 and 12 μm are affected by wind speed. The topography of land is more complicated than that of the ocean.

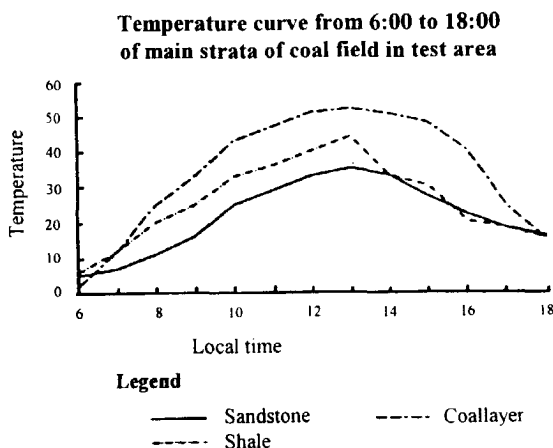


Figure 4-10. Temperature curves of three main rocks from the test area.

Mannstein (1994) showed that in mountainous regions, slope winds blowing parallel to terrain gradient transfer heat from higher temperature areas to cooler areas within the valley atmosphere. Furthermore, regional scale winds blowing across the ground surface in a given direction usually lead to the surface facing the direction being much cooler than adjacent mountain slope, even if it directly faces the sun. In Figure 4-7, several brighter areas where there are no coal fires are located in the same position facing the same direction and are most probably affected by wind.

Mannstein (1994) pointed out that thermal inertia ($\text{wm}^{-2}\text{k}^{-1}\text{s}^{1/2}$)

quantifies the thermal behaviors. Water and humidity at the ground surface also

consume a certain quantity of heat because of water evaporation.

10	9	8
8	A	6
6	5	4

(a)

7	8	9
6	B	8
5	6	7

(b)

Figure 4-11. Two pixels and altitude values of their surrounding pixels. On (a) sunshine begins at 5:50 in the morning. On (b) sunshine begins at 8:35.

4.6 Conclusions

Surface temperature in coal fields is mainly related to such variables as solar radiation, terrain slope and aspect, ground heat, and coal fires. It is also

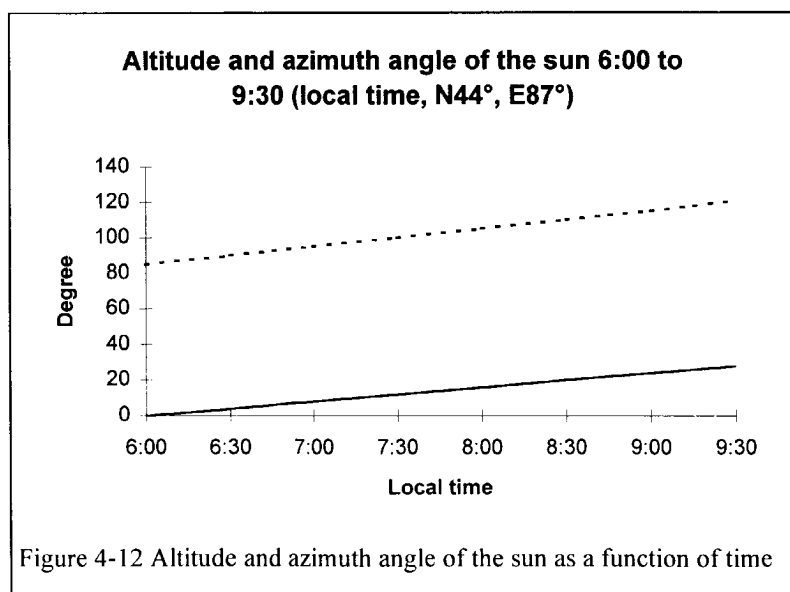


Figure 4-12 Altitude and azimuth angle of the sun as a function of time

related to parameters such as wind speed, atmospheric moisture, vegetation, albedo, emissivity, and thermal inertia. In test areas located in the dry mountainous regions of western China, vegetation is sparse and makes it relatively easy to conduct research and detect coal fires. It was found that there is good correlation between brightness level of TM image band 6 and the simulated illumination image. The coal fires, which could not be distinguished in the original TM image because of the effects of solar illumination, can be detected in the new adjusted image. If the effects of wind, inertia, and atmospheric moisture on surface had also been taken into account, the resulting image would be even more useful in detecting coal fires.

CHAPTER 5

Sub-pixel Coal Fire Detection and Surface Temperature Measurement from Landsat-5 TM Band 6 Data with Respect to the Spatial Resolution*

ABSTRACT

On the basis of the method of converting the radiance from thermal remote sensing data into radiant temperature, this chapter presents a method to evaluate the capability of Landsat TM thermal data for the detection of sub-pixel coal fires with respect to their sizes and temperatures. This method can also be used for the temperature estimation of coal fire areas of sub-pixel size, with the knowledge of the fire size being provided by airborne thermal scanner data or field survey data.

5.1 Introduction

Coal fires are a main geological hazard in many coal fields around the world. They not only cause loss of coal resources, but also damage the mining facilities and pollute the environment by the release of noxious gases such as CO₂, CO, NO, SO₂, etc. Subsidence of the ground surface and landslides are also major consequences of underground coal fires.

Remote sensing data acquired in the thermal infrared region of the electromagnetic spectrum provide a data source for the detection of the thermal anomalies caused by the coal fires. Airborne thermal infrared data have been widely used for coal fire detection (Slavecki 1964, Fisher and Knuth 1968, Ellyyett and Fleming 1974, Greene and Moxham 1969, Guan

* This chapter has been published as:

Xiangmin Zhang, J. L. Van Genderen and S. B. Kroonenberg, 1997, A method to evaluate the capability of Landsat-5 TM band 6 data for sub-pixel coal fire detection. *International Journal of Remote Sensing*, VOL. 18, NO. 15, 3279-3288.

1984,1989, Bhattacharya et al 1991, 1994, Zhang et al 1995, Cassells and van Genderen 1995). They have proven to be very useful for fire detection because of their high spatial and temperature resolution. The thermal infrared data from Landsat TM have recently been used for coal fire detection (Mansor et al. 1994, Saraf et al. 1995, Prakash et al. 1995, Zhang et al. 1995) and monitoring (Mansor et al. 1994).

Field work has shown that an individual coal fire is, sometimes, much smaller than the IFOV (Instantaneous Field Of View $120\text{m} \times 120\text{ m}$) of the Thematic Mapper Channel 6 on board Landsat-5. In order to monitor the coal fires, we need to know what size of coal fire can be detected by the Landsat TM thermal channel data. Several authors reported the detection of small intense sources of heat such as gas flares, straw burning, steel works and forest fires by means of NOAA AVHRR channel 3 data (Muirhead and Cracknell 1984,1985; Matson and Dozier 1981; Chuvieco and Martin 1994). Robinson (1991) summarized the use of mid-infrared data for detection of fires occupying a fraction of a percent of a pixel and the methods of calculating the size and temperature from multi-channel IR measurements. He used a method to calculate the saturation temperature of NOAA AVHRR band 3 data and to estimate the detectable biomass fires of AVHRR band 3 data by assuming background and detection threshold. Compared to biomass fires, coal fires are much more stable (spreading speed less than 15 m per year) and have lower temperatures and an area of smaller size. Because of the relatively low background temperatures, the integrated pixel temperatures calculated from the Landsat TM data are normally much lower than the temperature of the coal fire area. Based on Robinson' paper (1991) on AVHRR thermal data, we have adapted this method to evaluate the capability of Landsat TM band 6 data for the detection of sub-pixel coal fires with respect to their size and temperature. With the knowledge of the size of the coal fires, the temperature of the coal fire areas can also be estimated.

5.2 Detection of coal fires

Detection, according to The Shorter Oxford English Dictionary, is defined as exposure and revelation of what is concealed. Detection of coal fires therefore aims to distinguish the characteristics of the coal fires from the surroundings. Remote sensing data from the visible, near infrared and shortwave bands sometimes can also be used for the detection of the reflectance and radiance

characteristics of the coal fires (Reddy et al. 1993). The airborne or space borne thermal data are used to detect the temperature anomalies of the coal fires which are direct indicators of the underground coal fires. Landsat -5 TM thermal data record the surface radiance within the 10.4-12.5 μm spectral range. The data provide information about radiant temperatures which are determined by kinetic temperature and the emissivity of surface materials. The reflectance of the solar radiation is negligible within this wavelength band. Solar heating is a main factor in the natural heating process. During the day time, the surface temperatures are increasing and make the coal fire areas difficult to be detected. The variation of the surface temperatures caused both by topography or by surface heterogeneity also make coal fire detection difficult. When the temperatures of coal fires are high enough, the thermal anomalies are obvious in the remote sensing data if the spatial resolution is suitable. The spatial resolution of the sensor limits the capability of the data for the detection of the coal fires. The detection of a coal fire means that a coal fire causes a mixed pixel anomaly, and this anomaly can be distinguished from the surroundings. If the coal fire does not occupy a whole pixel the temperature should, then, be higher than for a full pixel fire to cause such a thermal anomaly. A coal fire in the thermal remote sensing data, if it can be detected, its DN(Digital Number) should be larger than the background DN plus a constant. One can derive the background DN from the statistical average of the remote sensing data. The variation of the surface temperature and the heterogeneity can be expressed as the standard deviation (σ) of the thermal remote sensing data. A simple way to select the constant is the trial and error method in the known fire area(Saraf et al. 1995). The standard deviation or two times of the standard deviation can be taken as the constants.

5.3 Methods

5.3.1 Radiance conversion and temperature derivation from TM 6 data

The Landsat-5 TM thermal channel acquires data within the 10.4-12.5 μm wavelength band with a ground resolution of 120m \times 120 m. The radiant temperature can be calculated by using the following method (Markham and Barker 1986). The radiance can be converted from the Digital Numbers of the Landsat-5 TM band 6 data.

$$L_{\lambda} = L_{\min} + \frac{L_{\max} - L_{\min}}{255} \times DN \quad (5-1)$$

where $L_{\min} = 0.1238 \text{ mWcm}^{-2}\text{sr}^{-1}\mu\text{m}^{-1}$ and $L_{\max} = 1.56 \text{ mWcm}^{-2}\text{sr}^{-1}\mu\text{m}^{-1}$ are the minimum and maximum of the radiance recorded by the Landsat-TM channel 6. The Landsat-5 (P-tape) TM data from the ground station are radiometrically calibrated so that there is a linear relation between radiance and the corresponding digital numbers (DNs) (Mansor et al. 1994). Planck's equation expresses the relation between the spectral radiance and the radiant temperature.

$$L_{\lambda} = \frac{\varepsilon C_1 \lambda^{-5}}{\pi [\exp(\frac{C_2}{\lambda T}) - 1]} \quad (5-2)$$

where $C_1 = 3.742 \times 10^{-16} \text{ Wm}^2$, $C_2 = 0.0144 \text{ mK}$, λ is wavelength in metres, ε is the emissivity of the object. From equation (5-2), the radiant temperature can be expressed as

$$T = \frac{C_2}{\lambda \ln[\frac{\varepsilon C_1 \lambda^{-5}}{\pi L_{\lambda}} + 1]} \quad (5-3)$$

For the Landsat-5 TM band 6 data, in the absence of an atmospheric contribution of attenuation, the radiant temperature is,

$$T = \frac{K_2}{\ln(\frac{K_1}{L_{\lambda}} + 1)} \quad (5-4)$$

Where $K_2 = 1260.56 \text{ K}$ and $K_1 = 60.776 \text{ mWcm}^{-2}\text{sr}^{-1}\mu\text{m}^{-1}$

5.3.2 Concept of sub-pixel detection

The temperature from formula (5-4) represents the average temperature of an area of IFOV (120m×120m) of Landsat-5 TM thermal data. To evaluate the capability of the Landsat-5 TM band 6 data for the detection of coal fires, let us assume an area equal to the size of the IFOV of TM band 6 which is partially occupied by

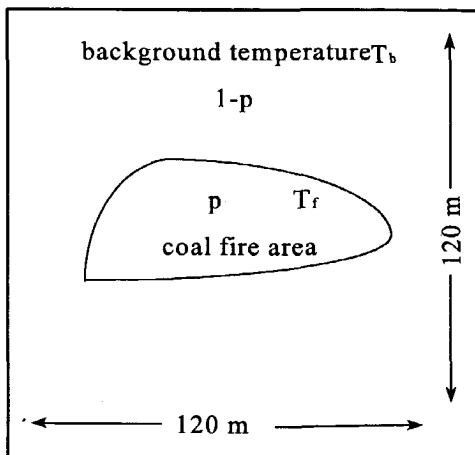


Figure 5-1. A coal fire partially occupies an area of IFOV of Landsat Thematic Mapper thermal channel

the coal fire area (p) with temperature of T_f . The other area is the background area ($1-p$) with temperature of T_b . The fire area has a higher temperature than that of the background $T_f > T_b$. The radiance of the mixed pixel area (L_m) is the contribution of both the fire and the background area which can be expressed as (Matson and Dozier 1981).

$$L_m = L_b(1-p) + pL_f \quad (5-5)$$

L_f and L_b are the radiance of the coal fire and background respectively. From Equation (5-5), one can derive the radiance of the fire area:

$$L_f = \frac{(L_m - L_b)}{p} + L_b \quad (5-6)$$

Inserting Equation (5-6) into (5-4), the temperature of the fire area can be derived.

$$T_f = \frac{K_2}{\ln \left(\frac{K_1}{\left(\frac{L_m - L_b}{p} + L_b \right)} + 1 \right)} \quad (5-7)$$

This formula can be used to evaluate the size and temperature of the coal fire partially occupying one pixel area of Landsat TM for a given scene. In other words, the formula expresses the relation between the temperature (T_f) and size (p) of a coal fire which caused a detectable thermal anomaly (L_m) from a background (L_b).

For a given scene of Landsat TM thermal data the L_m can be derived from the DN value of a pixel with a coal fire by Equation (5-1). The background DN is assumed as the average pixel value in a subarea in this paper. The L_b can then be derived from the background DN.

Let us assume $\Delta L = L_m - L_b$ which represents the radiance contrast between a mixed pixel and a background pixel. Equation (5-8) is derived from (5-7)

$$\Delta L = \frac{pK_1}{\exp \left(\frac{K_2}{T_f} \right) - 1} - pL_b \quad (5-8)$$

If one considers a single parameter, the assumption is made that all other parameters are fixed. On this basis, the following analysis can be made.

If L_b increases, ΔL decreases,

If p increases, ΔL increases,

if T_f increases, ΔL increases,

The first assumption means that a higher background temperature makes the pixel with a coal fire difficult to detect from the background pixels. The second assumption means that a large coal fire is easy to detect. The third one suggests that a fire with higher temperature is easy to detect.

5.4 Results

5.4.1. Capability for detection of a sub-pixel coal fire.

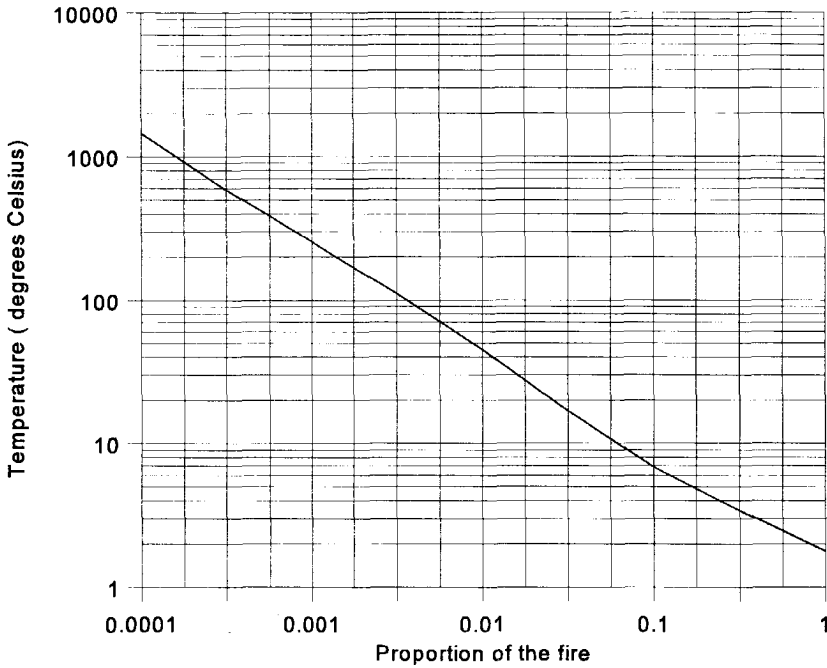


Figure 5-2. Proportion and temperature of a coal fire which causes a minimum increase from background. The pixel values without and with a coal fire are assumed as 88 and 89. Every point in the solid line represents one combination of temperature and size of a coal fire partially occupying an IFOV area.

For a given scene of Landsat-5 TM band 6 data, equation (5-7) can be used to evaluate the capability of TM data of band 6 for the detection of a coal fire which only occupies part of the pixel. A coal fire with a certain size and a certain high temperature can be detected in Landsat TM data. To accomplish this, two things need to be considered; one is the signal contributed by the coal fires (the intensity of the thermal anomaly), the other is the background

temperature and its variation. First we will consider the simplest case.

5.4.1.1 Case 1. Sensitivity of Landsat -5 TM band 6 data for the detection of coal fires

Here we suppose the background temperature is always the same. An area of $120\text{m} \times 120\text{m}$ of the same size as IFOV is partially occupied by a coal fire with temperature of T_f . The proportion of the coal fire within the IFOV is p . All emissivities of the ground objects are assumed as 1. If the pixels are without a fire they will have the same value in the Landsat TM data (DN_b) and have the same radiance (L_b). A pixel with a fire which can be theoretically detected must be at least 1 greater than the background digital number (DN_b). For instance, the background DN is assumed as 88 (equal to 1.26°C), the DN value of a pixel with a fire should, at least, be 89. The Equation of (5-7) then becomes

$$T_f = \frac{1260.56}{\ln\left(\frac{60.776}{(0.00563/p) + 0.61943} + 1\right)} \quad (5-9)$$

Giving a p , one can obtain a T_f . Figure 5-2, drawn by giving a series of p values in equation (5-9), shows the relation between temperature and proportion of a fire which partially occupies a pixel. Here the detection means that the coal fire causes a minimum change (1 pixel value increase) in the Landsat TM data with a background temperature of 1.26°C ($DN=88$). According to the field thermal survey, temperatures of the fire areas are normally lower than 500°C (Rosema et al. 1993). So if the area of a coal fire occupies less than 0.042% of the IFOV (about 6m^2), it cannot theoretically be detected by Landsat TM band 6 data. For a pixel fully occupied by underground coal fires, the surface temperature should be 0.5°C higher than what in the background pixel.

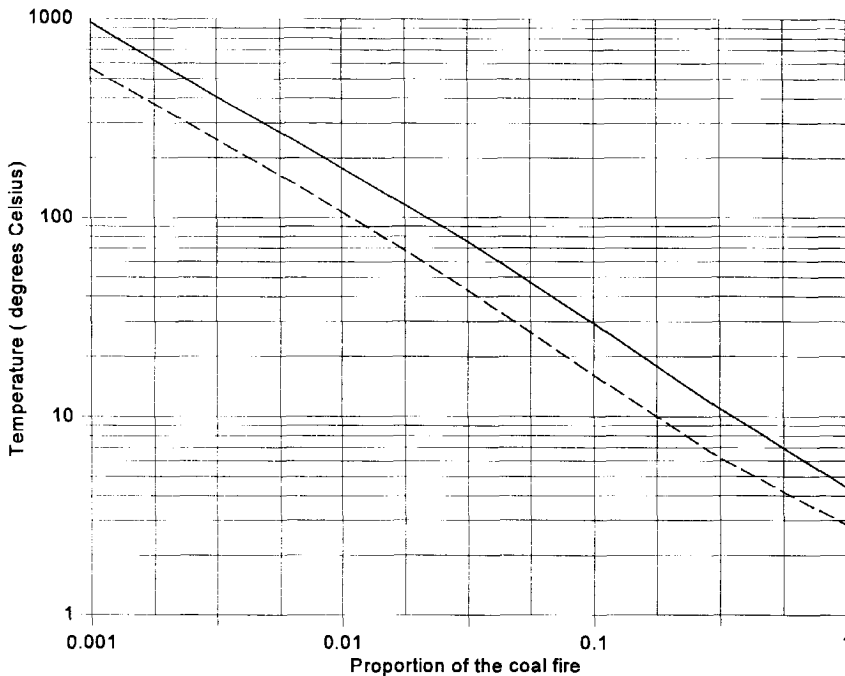


Figure 5-3. Proportion and temperature of coal fires which cause thermal anomalies (DN=91/dashed line, DN=94/solid line) from the background (DN=88).

5.4.1.2 Case 2. A practical detection

For coal fire detection using Landsat TM band 6 data, the statistical characteristics of the data, such as the average and standard deviation should be taken into account. For the night time data, the average value in a subarea (for instance, the coal bearing strata area) are supposed to represent the background temperature. The standard deviation expresses the variation of the surface temperature caused by the surface heterogeneity and coal fires etc.

One scene of night-time Landsat TM Band 6 data, acquired on the 7th of April 1995, has been used for the study. The test area is located in the Toutunhe area, some 30 km SW of Urumqi, the capital city of Xinjiang, China. Airborne thermal scanner data in this area are available and two field

surveys were carried out in the area during 1994 and 1995 to verify the coal fires detected by the airborne thermal scanner data and Landsat-5 TM thermal data. The average DN in the coal strata area is 88 which is taken as background DN_b. In this TM data DN=94 was selected by a trial and error method as the threshold of those coal fires causing unambiguous thermal anomalies. The standard deviation of the data in the study area is 2.86. The threshold of 94 can be also taken as the average plus twice the standard deviation.

The relation between the temperature of a coal fire and its proportion is showed in Figure 5-3. Every point in the line shows up a combination of temperature and size of a coal fire which all cause the same result of a thermal anomaly as DN=94 on the background DN=88. From Figure 5-3 we see that a coal fire with temperature of 500 °C should be larger than 0.25% (36 m²) of the IFOV to be exclusively detected in the night time data of 7 April 1995. The dashed line in Figure 5-3 shows the combination of the coal fire causing a thermal anomaly of DN=91 in the same background. These kinds of thermal anomalies in the night time data are recognizable but not all of them are caused by the coal fires. This value of DN is selected from background DN plus the standard deviation.

5.4.2 Calculation of high temperature coal fires with sub-pixel size by TM band 6 data

With the calibration of the Landsat-5 TM band 6 data, one can calculate the minimum and maximum pixel integrated temperature from equation (5-1) and (5-3). The pixel values of 0 and 255 from channel 6 data correspond to the lowest and highest apparent radiant temperatures that can be detected by the thermal channel, -69°C and +68 °C respectively. Surface objects with pixel integrated temperatures higher than +68 °C will be saturated. An individual coal fire is normally smaller than the IFOV of Landsat TM channel 6. Temperatures derived from the Landsat TM band 6 data are normally much lower than the real temperatures of the coal fire areas because of the low background temperature and the low resolution of the remote sensing data. With the help of equation (5-7), we can also calculate a coal fire area with temperatures higher than 68°C but only partially occupying the pixel when the proportion of the fire area is known.

Airborne thermal infrared scanner data are available of the study area. Data with a spatial resolution of $7.5\text{m} \times 7.5\text{m}$ were acquired for the purpose of detection of the underground coal fires. Two reference temperatures were set before flight for the calibration of the surface temperatures. Because the flight mainly concentrated on the detection of the areas of the underground coal fires, the lower reference blackbody temperature (BB1) is slightly lower than the average surface temperature in order to detect the details of the surface features. The higher reference temperature was set as the minimum temperature of the coal fires on the basis of the field

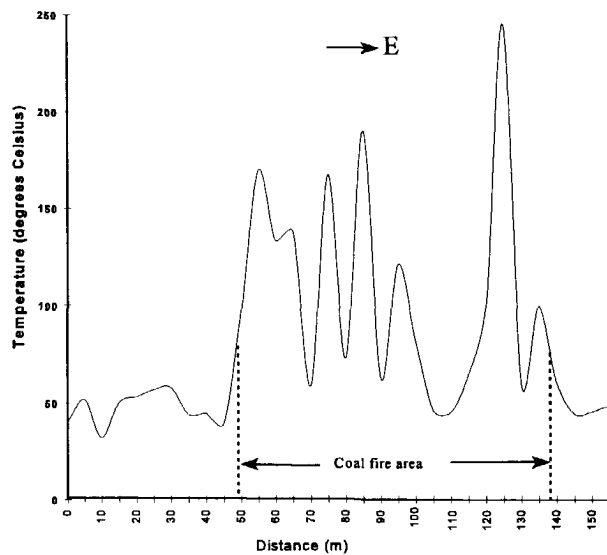


Figure 5-4. Along-strike temperature survey of coal fire 137 (measured from 2:00 to 4:00 pm on 16 August 1995)

temperature survey in order to reveal, to the largest extent possible, underground coal fires. In that case the coal fire areas are nearly all saturated and easy to be detected. But the real temperature of the fire area which is higher than the higher reference blackbody temperature (BB2) can not be calculated by these data anymore.

In the airborne thermal data (daytime) one coal fire is saturated by two pixels. The BB2 of day time airborne thermal scanner data is $38.2\text{ }^{\circ}\text{C}$. From the airborne data we know that the pixel-integrated temperature for the two saturated pixels exceeds $38.2\text{ }^{\circ}\text{C}$. In the Landsat TM data the same fire causes a thermal anomaly of one pixel ($120\text{m} \times 120\text{m}$). The data were interpolated into $30\text{m} \times 30\text{m}$ resolution, so we can see a 14-pixel (should be 16) thermal anomaly. Because the neighbouring pixels are cold in the airborne data, we can take the two pixels as fires and assume that the surroundings are cooler background. So the fire area is $2 \times 56.25\text{ m}^2$. The proportion of the fire in the

IFOV of TM band 6 is $p=2 \times 7.5 \times 7.5 / 120 \times 120$. The background temperature of the area can be derived from the neighboring pixels $DN_{\text{background}}=88$ from the Landsat-TM thermal data. The DN of mixed pixel with coal fires is 94. The temperature of the coal fire area which only partially occupies a pixel of Landsat TM thermal data can then be calculated by means of Equation (5-7).

$$L_m = 0.1238 + [(1.56 - 0.1238) / 255] \times 94 = 0.65322 \quad (5-10)$$

$$L_b = 0.1238 + [(1.56 - 0.1238) / 255] \times 88 = 0.61943 \quad (5-11)$$

$$p = 7.5 \times 7.5 \times 2 / 120 \times 120 = 0.0078125 \quad (5-12)$$

$$T_f = 214.2 \text{ } ^\circ\text{C} \quad (5-13)$$

In order to convert the apparent or the brightness temperature into the kinetic or true temperature of the surface, the emissivity of the surface must be known. We select the emissivity as 0.97 for the sandstone, shale and the burnt rocks (Li 1985, Salisbury and D'aria 1992).

$$T_f = \epsilon_\lambda^{1/4} T_K \quad (5-14)$$

Then the true surface temperature (T_k) is 215.8°C .

Another example is from coal fire 137 which is situated in the northflank of the Kelazha anticline. This coal fire spreads along the strike of the coal seam and is shallow. It extends about 90 m long and 2.5 m wide. The occurrence of the coal seam is $345^\circ \angle 83^\circ$. During the field work in August 1995, a thermal survey profile was made with 5-metre intervals of each measurement point by using a portable pyroelectric infrared thermal radiometer. Figure 5-4 shows the results of the thermal survey. The area of coal fire 137 is about 225 m^2 . Coal fire 137 is a rather isolated fire which we can clearly distinguish from other fires. In the airborne thermal scanner data ($7.5\text{m} \times 7.5 \text{ m}$ resolution) coal fire 137 made four pixels saturated. In the night-time TM data ($120\text{m} \times 120 \text{ m}$) of the 7th of April 1995, coal fire 137 shows up as thermal anomalies in two adjacent pixels with $DN=91$. The background pixel value is 88. As the two pixel values are the same, we assume fire 137 was equally included in two IFOV areas of Landsat TM channel 6. In this case the proportion p of the coal fire

137 within an IFOV is 0.008. The calculated temperature of the coal fire No. 137 is 127.5 °C. This temperature is close to the field temperature survey. From Figure 5-4 the average temperature of the fire area is 119 °C.

5.5 Conclusions

We have presented a method to evaluate the theoretical and practical capability of Landsat TM thermal data for the detection of coal fires with respect to temperatures and sizes. The background temperature, the quality of the Landsat data (cloud coverage), and the significance of the coal fires are the factors which determine the detectability of the coal fires. Given that field thermal survey data have shown that the temperatures of coal fires range from 17-500° C, coal fires less than 0.25% (36 m²) of an IFOV of Landsat TM band 6 cannot exclusively be detected from the night time data of the 7th of April 1995. The results show that Landsat TM night-time thermal data are suitable for regional coal fire investigation. However, for early detection of coal fires with a relatively small size and low temperature, Landsat TM night-time data are still too coarse in spatial resolution. With the knowledge of the size of a sub-pixel coal fire provided by airborne thermal infrared scanner data or field survey data, the temperature of the coal fire can be estimated.

CHAPTER 6

Spatial Analysis of Thermal Anomalies from Airborne Multi-spectral Data*

ABSTRACT

Based on the field thermal measurements, thermal anomalies caused by coal fires can be grouped into 3 categories, low-amplitude (up to 20 °C above the background), medium-amplitude (20-120 °C), and high-amplitude (above 120 °C). Night-time airborne thermal scanner data acquired in the 8-12.5 μm wavelength region of the electromagnetic spectrum clearly shows coal fires and background areas. However, the disadvantage for the night-time data is saturation at medium and high amplitude areas. In the daytime 8-12.5 μm image, medium amplitude thermal anomalies can be detected, which represent partial underground coal fires with partial solar heating of non-burning coal seams and black shale with higher emissivity. Daytime thermal infrared data acquired in the 3-5 μm wavelength region provide information both from the spectrally reflected solar radiation and radiation from high-amplitude surface thermal anomalies of the underground coal fires. To reduce the effects of the spectrally reflected solar radiation, the data acquired in 0.61-0.69 μm wavelength region were used to adjust the 3-5 μm data. The new image shows the enhanced high-amplitude thermal anomalies of the underground coal fires. Three kinds of data have been fused to integrate the background, low, medium, and high-amplitude thermal anomalies, which are highly correlated to the field thermal measurements. On the basis of spatial patterns of thermal anomalies and the underground coal fire spreading models set up through field observations, the spreading direction of underground coal fires are inferred. Comparing daytime and night-time 8-12.5 μm data, the solar heated coal seams were detected as areas that may have the occurrence of high-risk coal fires occurring in the future. This is because the temperatures measured in the field were close to the critical point of the spontaneous combustion of coal.

* This chapter has been submitted for publication as:

Xiangmin Zhang, J. L. van Genderen, S. B. Kroonenberg, 1998, Spatial analysis of thermal anomalies from airborne multi-spectral data, *International Journal of Remote Sensing* (submitted).

6.1 Introduction

Coal fires are one of the main hazards in the coal field areas in the northern part of China. In the Xinjiang Weiwuer Autonomous Region of Northwest China, 42 out of 88 coal mines and coal production bases suffer from coal fires. According to statistics, the total area affected by active coal fires is 111 km² (Kang et al. 1993), and the annual losses of coal resources are estimated to be 10-20 million tons in this region alone (Kang et al. 1993). In addition, coal fires also cause environmental and safety problems. And for efficient extinguishing of the coal fires, early detection and detailed information about the underground coal fires are needed.

Thermal infrared data from satellites, especially from Landsat-5 channel 6, (10.4- 12.5 μm) have been proven to be very useful to this end (Mansor et al. 1994, Zhang et al. 1995, 1997, Cassells et al. 1995, 1996, van Genderen et al. 1996, Prakash et al. 1995a, 1995b). However, in mountainous areas the detection of underground coal fires is complicated by the non-uniform solar heating of the terrain. To remove the non-uniform effects of solar heating, a DEM can be used for modeling the solar incidence angle (Zhang et al. 1995, Wan and Zhang 1996a, 1996b). Night-time TM data are more useful (Genderen et al. 1996) for detection, but are not routinely available. On the other hand, due to the low spatial resolution of the TM thermal data (120m \times 120m) the best night-time TM thermal data can not detect a coal fire less than 50 m² despite high temperature anomalies (Zhang et al. 1997). Thus airborne data for detailed detection are still needed for planning fire fighting activities. For the early detection and prevention of coal fires, the monitoring of very tiny hot spots with very high temperatures (120-300 °C and above) is necessary. However, no satellite thermal data or short-wave infrared data with sufficient spatial resolution are presently available.

Therefore, special airborne campaigns are usually carried out to obtain night-time (pre-dawn) thermal infrared data for the detection of surface anomalies above underground coal fires (Slavecki 1964, Ellyett and Fleming 1974, Fisher and Knuth 1968, Greene and Moxham 1969, Bhattacharya et al. 1991, 1994, Guan 1984, Huang 1991). In this paper we present a methodology that includes some results about the integration of night-time and daytime airborne thermal infrared data (8-12.5 μm) with

43°46'00" N

87°07'00" E

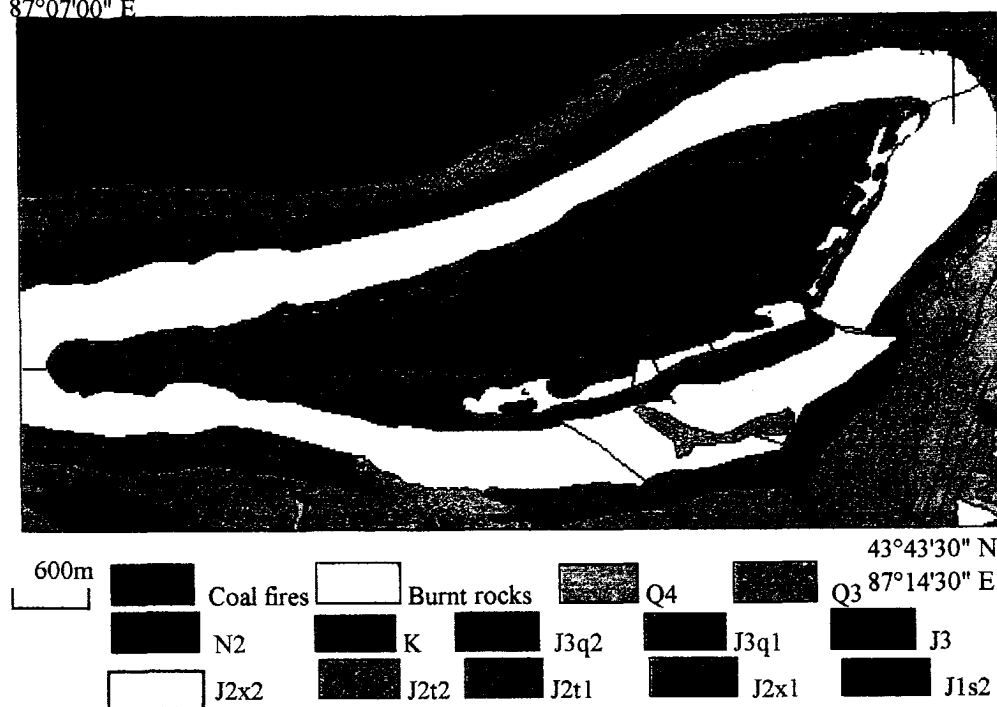


Figure 6-1 Geological map of study area.

daytime 3-5 μm data for the detection of different types of thermal anomalies of the underground coal fires. This image fusion approach maximizes the use of airborne data for detection and analysis of the thermal anomalies.

6.2 Field data

The study area is located 35 km Southwest of Urumqi, the capital city of the Xinjiang Weiwer Autonomous Region in Northwest China. It is a transition zone of the Tianshan Mountain fold belts and the Junggar Basin. It consists of Jurassic strata folded into an anticline 8 km long and 2 km wide (Figure 6-1). The coal seams that suffer from spontaneous combustion belong to the middle Jurassic Xishanyao group. Large areas underlain by burnt rock adjacent to former coal seams show that spontaneous combustion of coal seams has already been going on during a major part of the Quaternary (Zhang et al. 1998c). Three coal seam layers are burning at present, with thickness of 20m, 6m, and 2m, respectively, from the bottom to

the top. Most of these seem to have started by natural causes, independent of coal mining activities.

6.2.1 Coal fire spreading models

To understand the spatial distribution of coal fires and the nature of the thermal anomalies, it is necessary to discuss why fires that propagate themselves underground. Natural coal fires always start at the outcrop of a coal seam with a certain thickness. A coal seam of several meters thick that has burned out, shrinks to an ash layer of only several centimeters in thickness. Therefore, deep cracks develop and eventually the roof of the coal seam collapses. The cracks and the collapsed areas, together with the highly porous burnt overburden rocks then act as a chimney which promotes the

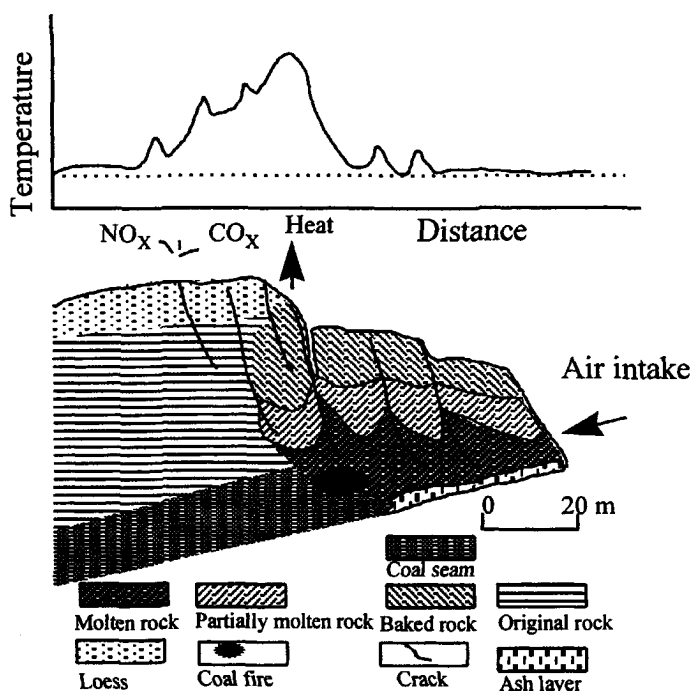


Figure 6-2a. Deepening model of coal fire

access of oxygen further underground. In this way a coal fire that started at the surface outcrop proceeds deeper and deeper underground in the dip

direction. The thermal pattern developing at the surface is dependent upon the size, depth, and the nature of heat transfer to the surface by conduction and convection.

Based on the field observations, we have developed three coal fire spreading models, namely the deepening model, lateral spreading model, and upwards model. A conceptual deepening model of underground coal fires is shown in Figure 6-2a. The thick coal seam with slight or medium dip angles tends to burn down in the direction of the dip, usually with a collapse above the coal seams which act as chimneys. Once the outcrop coal fires connect to the underground mining tunnels or the mine fires reach the surface by cracks, collapse, or fractures, the ventilation system changes and makes the thermal patterns of the coal fires more complex (Figure 6-2b). When the coal seam is steeply dipping, the coal fires starting at the outcrop move along one or two of the strike directions within a certain depth as showed in Figure 6-3 (lateral spreading model). Normally the spreading speed of coal fires is faster in the strike direction (5-15 m/year) (Kang et al. 1991, 1993; Bustin & Mathews, 1982, 1985) than in the dip direction (1-3m/year) (Kang et al. 1993; Ellyett and Fleming 1974), especially when the coal seams are steeply dipping. When there are several coal layers, coal fires may develop from one lower coal seam to an upper one (upwards model). In the area of coal fires No. 141, 142, and 143 in the south wing of the Kelazha anticline the coal fires are upwardly spreading from the 20 m coal seam to the 6 m coal seam and even to the 2 m seam.

6.2.2 Field thermal survey

In extensive field campaigns in 1994 and 1995, surface temperatures were measured in the coal fire areas by using a portable Pyroelectric Infrared Thermometer Model ER-2008 manufactured by the Japanese company National. Ten thermal profiles and one grid were made. The distance between the measurements was 5 meters and in total about 700 temperature measurements were taken in the area of Kelazha anticline. Two of the profiles were measured in the north flank of the anticline and the rest are in the area of coal fire No. 141, 142, and 143. To study the coal fire spreading, three of the ten thermal profiles were measured along the dip direction of the coal seams and the remaining seven along the strike direction. On the basis of field observations and surface temperature measurements, the width

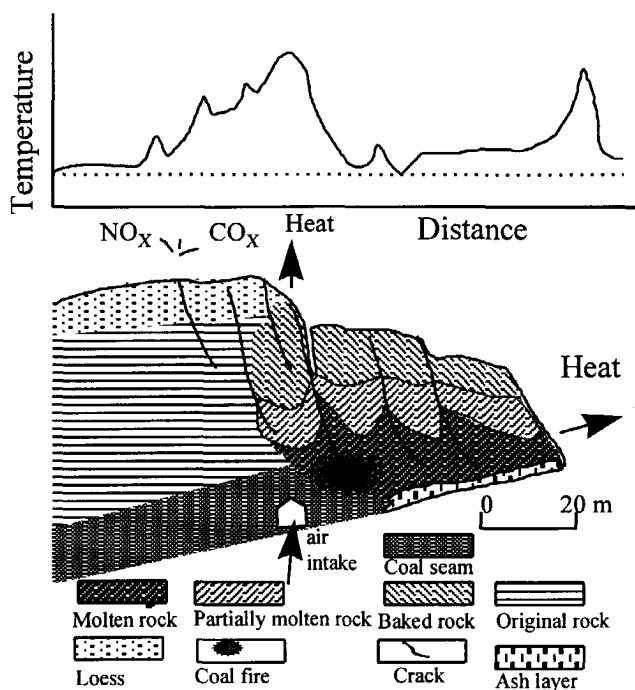


Figure 6-2b. Deepening model of coal fire connected with underground mining tunnels.

thermal anomalies above the underground coal fire areas were classified into three groups (Figure 6-4): 1) Low-amplitude thermal anomalies without significant changes in texture and color have surface temperatures of up to 20 °C higher than the background. These thermal anomalies are the largest among the three; 2) medium-amplitude thermal anomalies with leakage of tarry substances, haloes of sulphur crystals, micro-cracks, and holes in the surface. They are usually 20 to 120 °C above the background temperature; and 3) high-amplitude thermal anomalies above the sublimation point of sulphur where we observe salmiac deposition, molten rock, and big cracks and collapse holes that have temperatures of about 120 °C to over 300 °C. The highest temperatures were typically located at hill tops over active coal fires, apparently because the higher topographic elevation ensures a longer chimney system to supply the fire with oxygen.

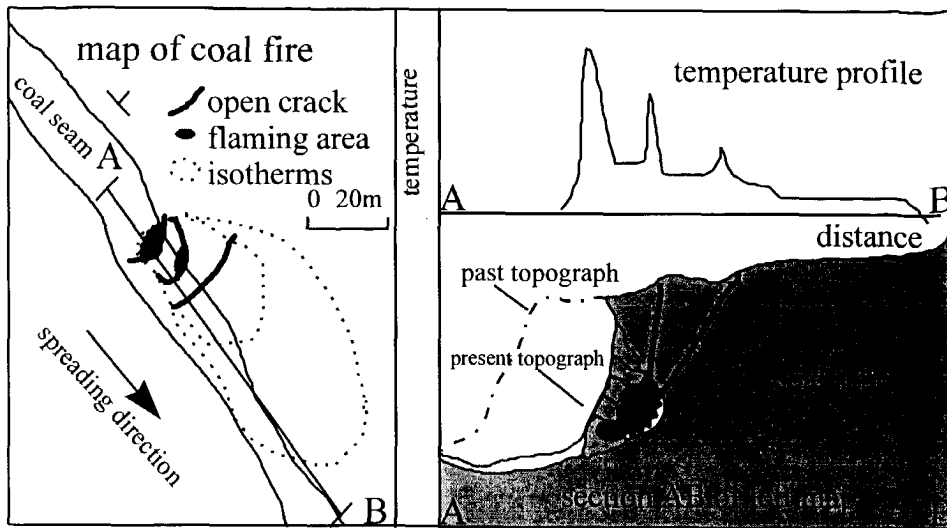


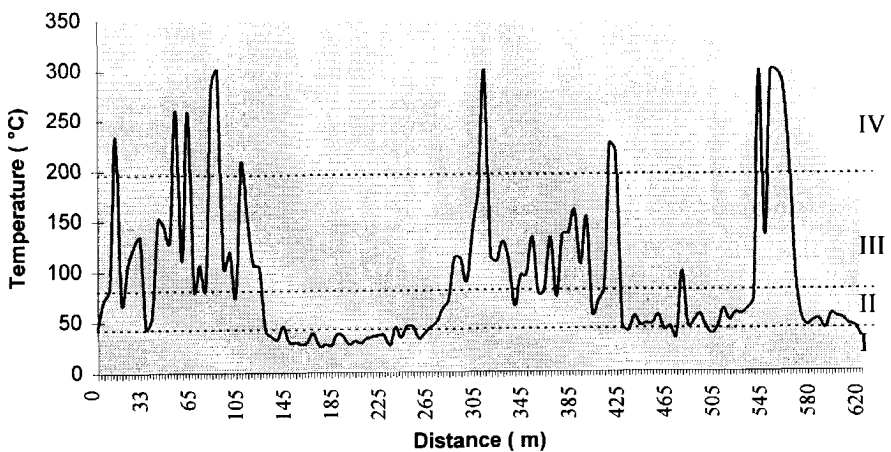
Figure 6-3. Lateral spreading model of coal fire.

The width of individual high-amplitude thermal anomalies usually does not surpass a few meters.

Generally we can use the spatial thermal pattern to determine the spreading direction of underground coal fires. This pattern consists of low, medium, and high-amplitude thermal anomalies that induce the spreading direction from the high-amplitude hot spots to the medium and low-amplitude areas, or from the high or medium-amplitude belt to the wider lower-amplitude thermal anomaly areas. Combining the thermal IR imagery with the coal fire spreading models, the spreading direction of the underground coal fires can be determined (cf. Fig. 6-5f discussed below).

6.2.3 Airborne thermal data

A flight campaign was carried out in our study area in July-August 1992. The flying height was 3500 m. Onboard the aircraft was a Chinese-made Airborne Multi-spectral Scanner and an airborne survey camera (of RC-10). The camera took color infrared aerial photographs. The scanning rate of the Multi-spectral Scanner is 20 lines/second and the Instantaneous Field Of View (IFOV) is 3 mrad. The data were digitally recorded on CCTs. The night-time flight took place on July 30th, 1992 at predawn (5:00-7:30 am) and



I-- background temperature II-- low-amplitude thermal anomalies
 III—medium-amplitude thermal anomalies IV—high-amplitude thermal anomalies

Figure 6-4. Field along-strike measurement of temperature profile of coal fires no. 141, 142 and 143 (measured at noon time of 17 August 1995).

only thermal infrared data from the 8-12.5 μm (band 6) was acquired (Figure 6-5a). On the basis of the surface temperature surveys, the two internal blackbody reference temperatures for the night-time flight were chosen as $\text{BB1}=11.5^\circ\text{C}$ and $\text{BB2}=20.2^\circ\text{C}$. The daytime flight was carried out on August 7th, 1992 at approximately mid-day (1:28-2:43 pm). Thermal infrared data were acquired in both the 8-12.5 μm wavelength (band 6) (Figure 6-5b) and the 3-5 μm wavelength (band 5) (Figure 6-5c). The blackbody reference temperatures for the daytime band 6 were $\text{BB1}=17.5^\circ\text{C}$ and $\text{BB2}=37.3^\circ\text{C}$. Data were also acquired from another four channels working in visible and near infrared wavelength similar to the corresponding Landsat TM bands. These bands consisted of: Band 1 (0.45-0.51 μm); Band 2 (0.53-0.61 μm); Band 3 (0.61-0.69 μm) (Figure 6-5d); and Band 4 (0.69-0.77 μm).

6.3 Image processing

To analyze the spatial characteristics of the coal fires, four images were used: 1) night-time thermal infrared images of 8-12.5 μm (night-time band 6) (Figure 6-5a); 2) daytime thermal infrared image of 8-12.5 μm (daytime band 6) (Figure 6-5b); 3) daytime thermal infrared image of 3-5 μm (daytime band 5) (Figure 6-5c); and 4) one of daytime visible bands. In this study we used

the band 3 image (Figure 6-5d). These images were first co-registered. For the daytime short thermal infrared data of band 5 from 3-5 μm wavelength, visible band 3 was used to remove the component of the spectrally reflected solar radiation (Figure 6-5e). The coal fire thermal anomalies in three images, namely the night-time band 6 data, daytime band 6 data, and the adjusted daytime band 5 data, were extracted by setting a threshold, respectively. By using the night-time thermal infrared band 6 data as a background, the thermal anomalies extracted from different images were integrated into a single one (Figure 6-5f).

6.3.1 Geo-registration

The daytime band 3 data from 0.63-0.69 μm were geo-referenced to a topographic map at the scale of 1:25,000. The rest of the data were then co-registered to this image. For daytime data such as daytime band 6 and band 5, the accuracy of the co-registration is less than one pixel according to the accuracy of the transformation algorithm and to the on-board co-registration. The accuracy of the co-registration of night-time band 6 data with the daytime data depended on the algorithm used and on the selection of the location and numbers of control points. The accuracy of the resulting co-registered images was within 2 pixels. To keep the original pixel Digital Number (DN), the nearest-neighbor resampling method was used.

6.3.2 Adjustment of daytime band 5 data

The signals on the daytime band 5 data are a mixture of the radiation mainly from:

- 1) spectrally reflected solar radiation by the surface
- 2) spectrally reflected solar radiation by the atmosphere between the sensor and the surface
- 3) the surface thermal radiation

Item 2 is uniform for all the pixels in the image. For detection purposes we can neglect it. However, we need to separate items 1 and 3. Acquisition of band 5 data during a night-time flight may bypass the problem of reflected solar radiation, but the disadvantage of such an image is the poor information of the background. For the data available in this study, we overcame this

problem by combining band 5 data with a data set from a visible band, namely band 3, acquired from 0.61-0.69 μm wavelength. Within the wavelength of band 3, the data represent the spectral reflected solar radiation. The surface thermal radiation is negligible.

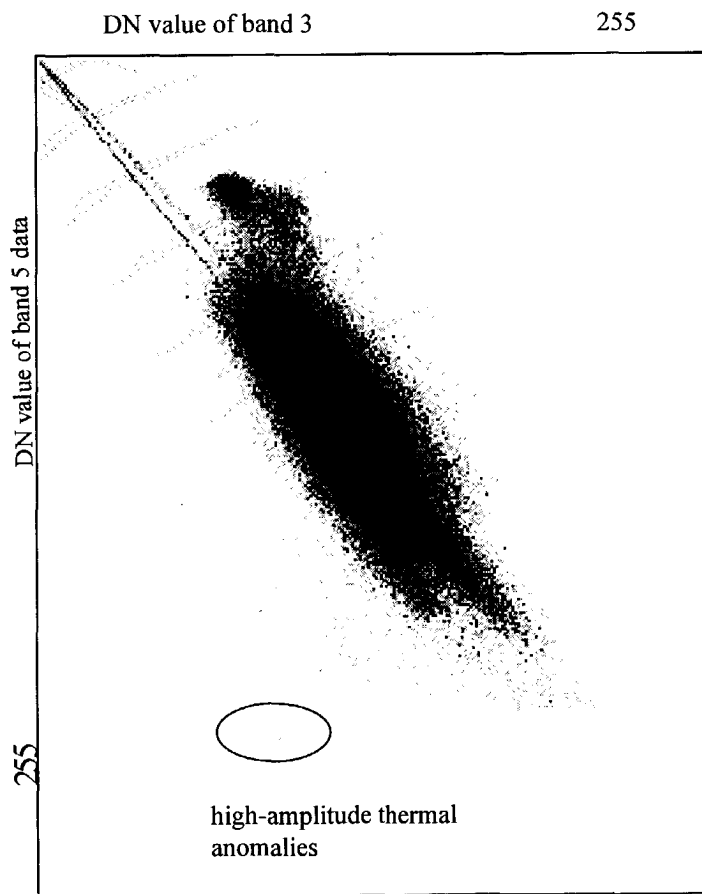


Figure 6-6. Scatter map of daytime band 3 and band 5 data.

A histogram scatter map was created and shows the high correlation between the daytime scanner data from 0.61-0.69 μm (band 3) and the daytime thermal data from 3-5 μm (band 5). The correlation coefficient is 0.935. This high coefficient of the two bands indicates the similar reflectance characteristics of the ground objects within both wavelength regions of 0.61-0.69 μm (band 3) and 3-5 μm (band 5). From the scatter map (Figure 6-6),

one can see the different characteristics of reflectance for water bodies in the two images. The characteristics of the coal fires in the scatter map can also be seen as areas that have a high DN number in band 5. An adjusted new image was created by subtracting the band 3 image from band 5. The background of the new image is very dark. Figure 6-5e is the subtracted image with stretch processing. One of the most significant characteristics of Figure 6-5e is that this image reveals many small bright areas which represent the intensive coal fire areas. On this image the part of the signal from the reflected solar radiation is suppressed and the thermal radiation parts enhanced. The hot spots in the coal fire areas correspond very well to the field survey results (around coal fire 137, 141, 142, 143). Some hot spots on the original band 5 images, which are located in areas with high reflectance, are not so clear, whilst in the new image they are clearly visible. Compared to the nighttime thermal image acquired from 8-12.5 μ m (band 6) in daytime, the areas of the hot spots are much smaller.

6.3.3 Thresholding

The thermal anomalies from the remote sensing data are derived by setting a threshold. There are three ways to select the threshold: 1) trial and error (Saraf et al. 1995; Prakash et al. 1995a); 2) exclusion; and 3) statistical (Zhang et al. 1997). For the first method, field measurement results are used. The second method gives a threshold to select the coal fire areas which excludes all pixels outside the coal-seam areas. Care should be taken in the nearby village areas of Liuhuanggou where some objects such as a cement factory are hotter than the underground coal fires areas. The statistical method provides the threshold on the basis of the statistical data of the sub-image, such as average and standard deviation. In this study we use the average DN plus two times the standard deviation as the threshold which is quite close to the threshold set by the exclusion method. For the night-time thermal infrared scanner data, the threshold set of the DN by the exclusion method is 182/181.

6.3.4 Integration

In order to make an integrated image depicting different thermal anomaly intensities, several temporal images were used. The first one is an image with pixel DN=1 representing low-amplitude thermal anomalies derived from

night-time band 6 (Figure 6-5a) using threshold 182/181 and pixel DN=0 for the other areas. The second image has two DNs: DN=2 for the areas of medium-amplitude thermal anomalies from daytime band 6 (Figure 6-5b) by using threshold 203/202; DN=0 is the background areas. For the third temporal image, DN=4 was assigned to represent the high-amplitude thermal anomalies from the adjusted daytime band 5 data (Figure 6-5c), and DN=0 the background. Fusing the three temporal images together, a new image was formed with possible DN values from 0 to 7. (actually, seven different kinds of thermal anomalies can be distinguished). For simplification, these have been grouped into 4 categories: DN=1,2,3 and larger than 4. By means of a color look-up table these have been represented in white, blue, green, and red. A logical calculation method was used to replace the pixels with DN=0 in the fourth temporal image with the night-time band 6 image. This resulted in Figure 6-5f.

6.4 Results and Discussion

6.4.1 Thermal anomalies from different data

Night-time airborne thermal infrared images are good for the detection of the underground coal fires. Acquisition at night-time can get the best temperature contrast between the fire areas and the background areas. On the other hand, the setting of the two blackbody reference temperatures are also very important. The lower blackbody reference temperature was selected slightly lower than the background temperatures to reveal details of the terrain information on the image. The higher reference temperature was selected in accordance with the low-amplitude thermal anomalies. As we see in Figure 6-5a, the white spots represent the coal fire areas. For the locating of the coal fires this is ideal data. However, one of the disadvantages of the data is that most of the "white" areas have saturated pixel values. Therefore, it is impossible to analyze the thermal pattern of different types of thermal anomalies. Figure 6-8 is a profile along the coal fire No. 141 to 143. The thick line represents the DN values in the night-time thermal data. The thin line represents the field temperature measurement showed in Figure 6-4. The flat top of the thick line shows the saturation at medium and high-amplitude areas. The higher setting of the blackbody temperatures of the daytime data made the data more suitable for the detection of the medium and high thermal

anomalies, while the low-amplitude thermal anomalies are easily confused by the solar-heated background.

As the emission peak of hot objects shifts towards shorter wavelengths, channels acquiring remote sensing data within shorter wavelength regions (3-5 μm) are more sensitive for higher temperature objects than those from the longer wavelength (8-12.5 μm). The high-amplitude thermal anomalies can therefore be revealed by the band 5 data. The different thermal pattern can be seen in images Figure 6-5f., and Figure 6-7 which is an enlarged area of coal fire No. 141, 142, and 143. Most of the medium- and high-amplitude thermal anomalies lie within the low-amplitude thermal anomaly areas. This pattern corresponds to the deepening and upward models of the coal fires in the south flank of the anticline, where two to three rows of cracks with the high-amplitude thermal anomalies can clearly be detected. Figure 6-9 is a profile that shows the types of coal fires detected from the integrated image of Figure 6-7. The thick line indicates the types of thermal anomalies and the thin line indicates the temperature measurements showed in Figure 6-4. Comparing the three profiles of Figure 6-4, Figure 6-8, and Figure 6-9, one can find a good correlation among them. The high-, medium-, and low-amplitude thermal anomalies derived from the integrated images agree with the thermal anomalies measured in the field.

6.4. 2 Thermal anomalies detected only by daytime band 6 data of 8-12.5 μm and the prediction of the new coal fires

Generally speaking, the night-time band 6 data are more sensitive to thermal contrasts between the fire areas and the background. A thermal anomaly in the daytime band 6 data, if it is caused by a coal fire, should be also a thermal anomaly in the night-time band 6 data because of the higher BB temperature setting for the daytime flight. However, in Figure 6-5f we see some blue areas which are thermal anomalies revealed only by the daytime band 6 data, but absent in the night-time band 6 thermal data. These areas cannot be active coal fire areas. Field observations and thermal radiometer measurements have shown that these areas correspond with areas of strongly solar heated coal

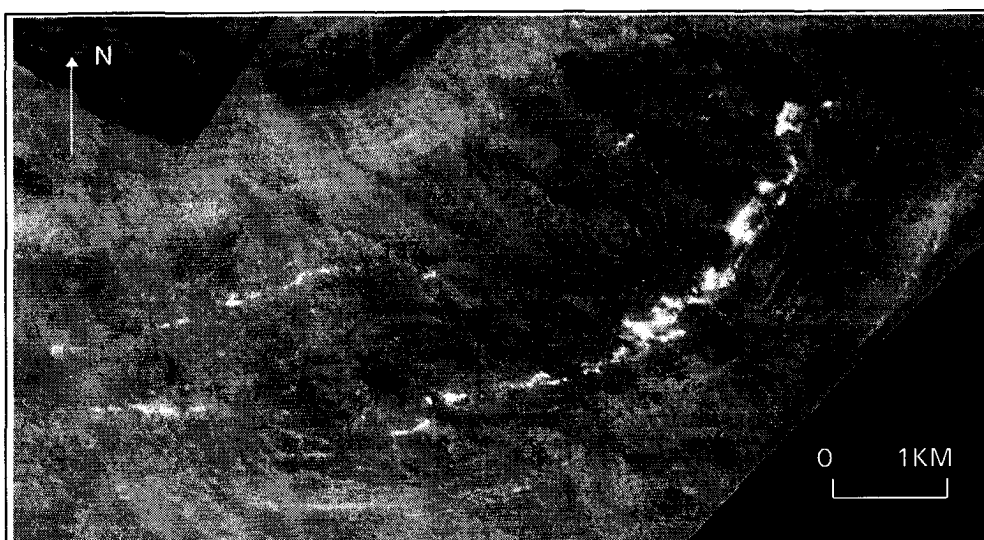


Figure 6-5a: Mosaic night-time thermal multi-spectral infrared scanner data of 8-12.5 μm (band 6). The white areas show the thermal anomalies caused by underground coal fires.

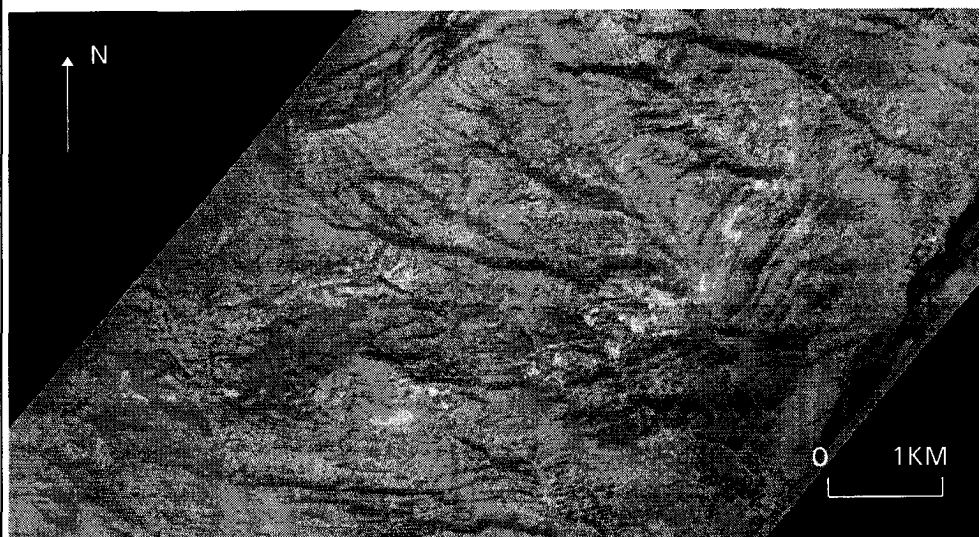


Figure 6-5b. Daytime thermal multi-spectral infrared scanner data of 8-12.5 μm (band 6). The white areas, which are smaller than those in Figure 6-5a due to the higher setting of BB reference temperatures, show the thermal anomalies caused by underground coal fires.

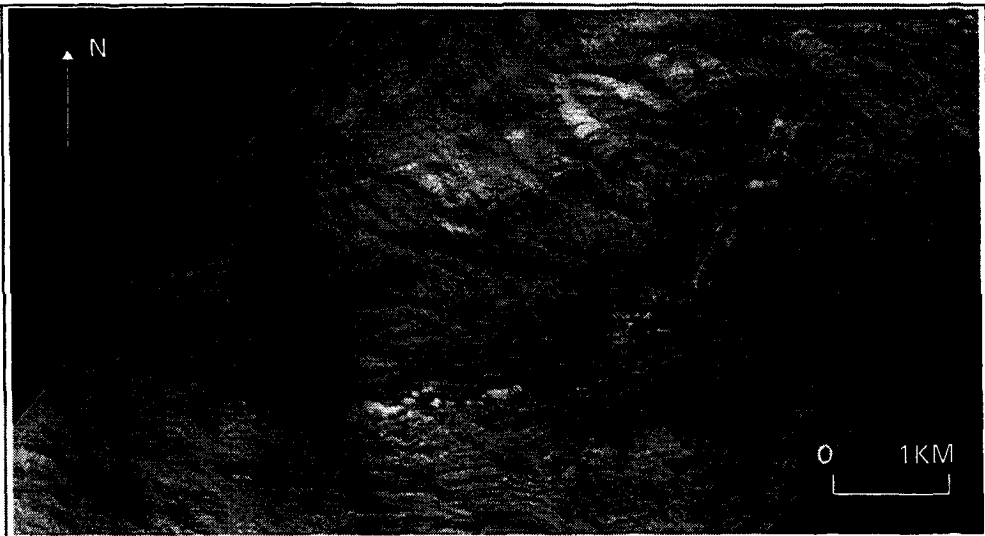


Figure 6-5c. Daytime thermal multi-spectral infrared scanner data of 3-5 μm (band 5).

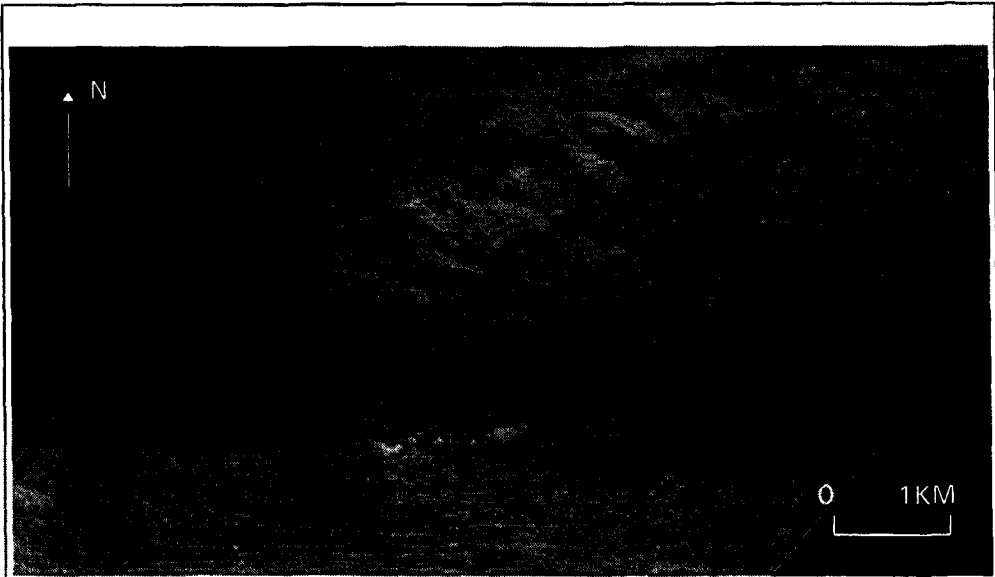


Figure 6-5d. Visible band image of 0.63-0.69 μm (band 3).



Figure 6-5e. Image generated by subtracting band 3 from band 5 with stretch processing.

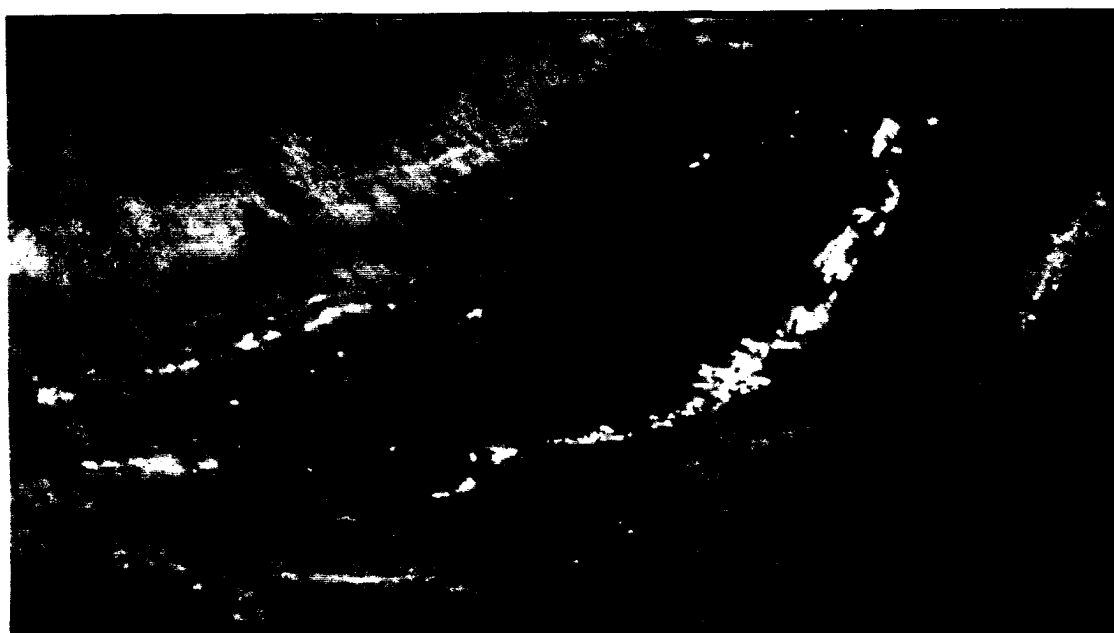


Figure 6-5f. Integrated image of night-time and daytime band 6 data, band 5 and band 3 data.



Figure 6-7. Sub-image of Figure 6-5f showing the coal fires No. 141, 142 and 143 and the location of the profiles.

coal seams or black shale outcrops. The highest surface radiation temperature measured for the solar heated coal seam and black shale outcrops reached 75 °C(Figure 6-10). This temperature is close to the critical temperature for second stage spontaneous combustion of coal (Bannerjee 1985). One can infer that those areas with thermal anomalies detected only from the daytime

thermal scanner data are those areas with a high risk for starting new coal fires caused by solar heating. Therefore, we can use remote sensing data for the prediction of the coal fires in coal seam outcrop areas.

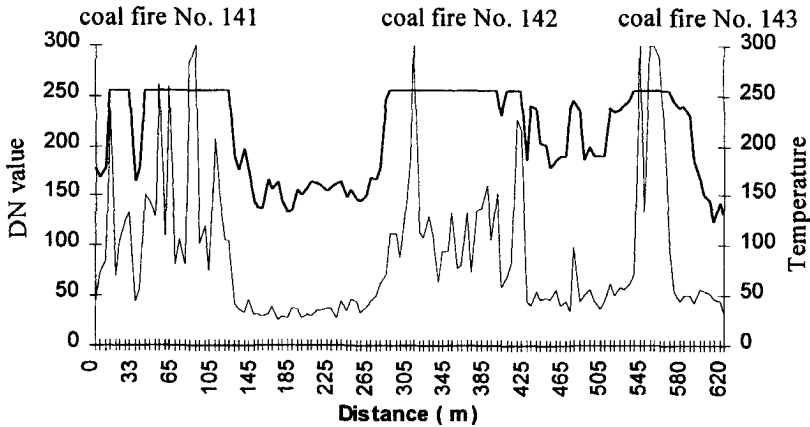
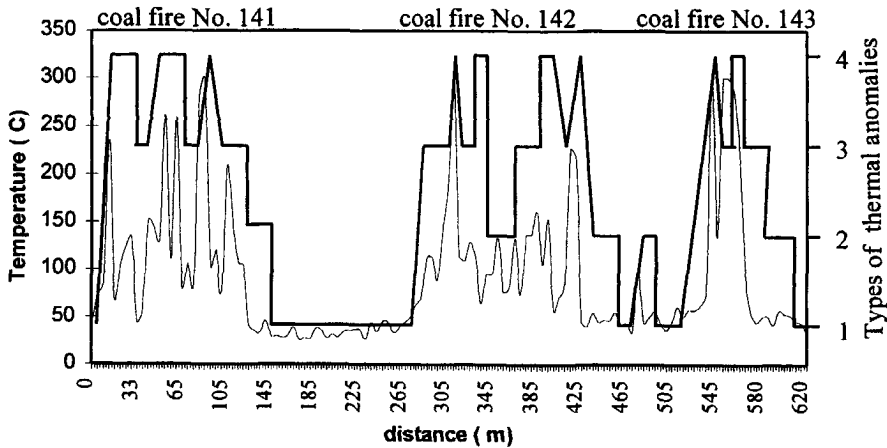


Figure 6-8. Profile derived from night-time thermal image of figure 6-2a. The thick line represents the DN values in the night-time thermal data. The thin line represents the field temperature measurement shown in Figure 6-4.



- 1-background
- 2-low intensity thermal anomalies
- 3-medium intensity thermal anomalies
- 4-high-intensity thermal anomalies

Figure 6-9. Profiles derived from Figure 6-7. The thick line indicates the types of thermal anomalies. The thin line indicates the temperature measurements shown in Figure 6-4.

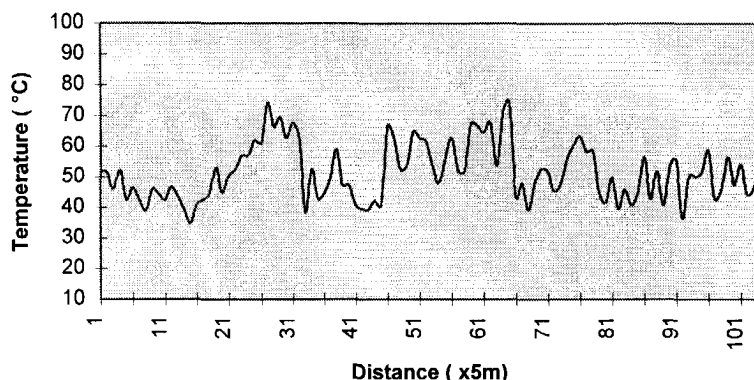


Figure 6-10. Field temperature measurement along coal seam and black shale in the north flank of the Kelazha anticline (measured at 14:00-16:00 August 16, 1995).

6. 5 CONCLUSIONS

(1). Integration of multi-spectral airborne thermal data acquired at different times and wavelengths can provide more detailed information about underground coal fires than any single source.

(2). Night-time thermal infrared remote sensing data with a lower setting higher blackbody reference temperature are very useful for distinguishing the fire areas and the background areas. However, different types of thermal anomalies can not be distinguished from each other in this data. The integrated image provides all four types of thermal anomalies found by the thermal measurements.

(3). Short wavelength thermal infrared airborne data (3-5 μm) adjusted by a visible band (band 3) are very sensitive to high-intensive hot sources such as the cracks and vents of the underground coal fires.

- (4). Spatial thermal patterns from the integrated image provide information on types and spreading directions of underground coal fires.
- (5). Daytime thermal infrared data (band 6) can be used for the detection of the medium amplitude thermal anomalies of underground coal fires.
- (6). Using a combination of daytime and night-time thermal data, it is possible to predict where new surface coal fires are most likely to occur.

CHAPTER 7

Multi-sensor Data Fusion for Coal Fire Monitoring*

ABSTRACT

The spontaneous combustion of coal causes widespread underground coal fires in several countries, including to a great extent China. These coal fires cause serious environmental, economic, and safety problems. In northern China, the coal fires occur within a region stretching 5,000 km east-west and 750 km north-south. Remote sensing therefore provides an ideal tool for monitoring this environmental hazard over such a large and remote area. As part of a research project to detect, measure, monitor, and extinguish these coal fires, this paper describes a remote sensing based multi-sensor data fusion methodology for detecting the underground fires. The methodology is based on fusing a variety of satellite-based image types (optical, thermal, microwave) together with airborne data (optical and thermal infrared) and ancillary data sources such as geological and topographic maps, etc. The results of the remote sensing data fusion are presented using pixel, feature, and decision based fusion approaches.

7.1 Introduction

The spontaneous combustion of coal is a common problem in many coalfields throughout the world. Those in the United States, Australia, and India have been extensively studied (Fischer and Kunth 1968; Ellyett and Leming 1974; and Prakash, et al. 1995a, 1995b respectively). However, these coal fires almost fade into insignificance compared to the size, extent, and amount of coal lost by coal fires in northern China. Remote sensing satellite data studies have shown that coal fires occur from NW to NE China in a belt stretching 5,000 km east-west and 750 km in north-south direction (Guan, 1984, 1989). Figure 1-1 shows a location map indicating the main coal fields where underground coal fires occur. The annual losses

* This Chapter will be published as:

Xiangmin Zhang, C. J. S. Cassells and J. L. van Genderen, 1998, Multi-sensor data fusion for the detection of underground coal fires, *Geologie en Mijnbouw*, vol 77 (in press).

are estimated at 100 million tons of coal (Rosema, et al. 1995). In 1987, the ITC was invited by the Chinese Ministry of Coal Industry to study this problem using remote sensing techniques. For the past ten years, researchers from ITC and the Chinese partners have studied the use of almost all satellite derived data types, as well as various airborne techniques to detect, measure, and monitor the underground coal fires in numerous regions of northwest China. These have included the provinces of Shanxi, Gansu, and Shaanxi, and the autonomous regions of Inner Mongolia, Ningxia, and Xinjiang (Zhang, et al. 1995; Cassells and Genderen 1995; Cassells, et al. 1996; Genderen, et al. 1996).

What these studies, and the majority of the published literature on the detection of underground coal fires show, is that several satellite and airborne sensors can partially detect such fires. This depends, however on certain conditions such as size and depth of the fire, relief, time of the data acquisition, prevailing weather conditions, time of the year, etc.

Realizing that each sensor and its associated image/data type only partially detects the coal fires, the objectives of the research described in this paper are to fuse the data, feature, or information extracted from each individual sensor source in order to have a more complete, robust, and reliable result on the location of the coal fires. For example, in optical imagery, the burnt rock above the coal fire often displays a unique spectral signature as the baked rocks have a different reflectance to the natural overburden. Optical imagery does not indicate, however, if there is presently a fire or if the burnt rock is caused by a paleo coal fire (coal fires are known to have occurred in the area due to spontaneous combustion since Pleistocene time, Zhang, et al. 1998c). Similarly, thermal infrared data from satellites can identify hot spots which could be underground coal fires only under certain conditions. Hence, the methodology of the multi-sensor data fusion in this paper suggests that by using multiple sensors simultaneously, more reliable data will result in the location of the coal fires than would be possible by using them independently.

7.2 Remote sensing data used for analysis of underground coal fires

Underground coal fires can cause a series of changes at the land surface. These include: an increase in temperature, emission of smoke, color changes of caprock, formation and deposition of new materials at the surface (e.g. sulphur, salmiac deposits), and land cracking and subsidence of the surface. These changes at the surface are used by the various remote sensing platforms and sensors as indicators of sub-surface fires.

Smoke and thermal anomalies are considered to be direct indicators as they can be seen clearly and directly on air photos and thermal infrared imagery respectively. Short-wave infrared can also detect coal fires directly if the thermal anomalies caused by the fire have a temperature higher than 160 °C (Zhang, et al. 1997).

The other indicators cited above, such as spectral reflectance changes in the caprock, land subsidence, etc., are referred to as indirect indicators of such surface coal fires because these characteristics cannot by themselves indicate if an underground coal fire is still burning or stopped burning in Pleistocene (Zhang, et al. 1998c). The following paragraphs provide the results of single-sensor detection techniques to find underground coal fires. This will be followed by a description of the newly developed multi-sensor data fusion approach, together with a discussion of the results and benefits.

7.2.1 Aerial photography

Aerial photography is very useful for studying underground coal fires. Figure 7-1 is an example of a color-infrared aerial photograph. On this image, all the cracking and land subsidence can be clearly observed. Together with the unique spectral reflectance of the burnt caprock, these features indicate the presence of an underground coal fire. In particular, a stereoscopic 3-D study of the aerial photographs using optical magnification can provide detailed information on the geological structures and the coal seam outcrops, etc.

A limitation of aerial photography is that it is relatively expensive to acquire on a regular basis for monitoring purposes, and especially so for an area of

5000×750 kms. In addition, the large number of photographs that would need to be interpreted would further make aerial photography prohibitive.



Figure 7-1. Extract from a color infrared aerial photograph of an underground coal fire area, taken 7th August, 1992. Note the distinctive color of the burnt rock (yellowish orange color). Immediately adjacent to the central area of burnt rock can be seen an extensive area of land subsidence, indicated by the long parallel cracks in the land surface.

7.2.2 Airborne Thermal Infrared data

This well-established technique has been used to detect underground coal fires since 1963. In 1964, Slaveki used it to detect coal fires in Pennsylvania (U.S.). Since then it has been used successfully to detect and measure sub-surface coal fires in many countries (Greene and Moxham 1969; Bhattacharya and Reddy 1994; Zhang et al. 1995; Guan 1989). Daytime data is often acquired in both the thermal-infrared windows of 3-5 μm and 8-14 μm . Typically, the best results are obtained during a pre-dawn flight when thermal contrasts between the fire areas and the colder non-fire areas are strongest. The technique has also been used to detect the depth and direction of the coal fires underground (Saraf, et al. 1992, 1995; Cassells and Genderen 1995).

When using digital thermal infrared data it is important to set the two internal black-body reference temperatures at realistic figures. This is accomplished by using a lower and higher reference temperature for the two internal black-bodies in the thermal infrared scanner. These are then related to digital values ranging from 0 to 255. Any temperatures above the temperature of the higher black-body pre-set reference temperature will be saturated. This means no quantitative temperature analysis can be done, although for simple detection this is not a problem. In terms of large area coverage and costs, the same drawbacks mentioned in the above section for aerial-photography apply also. Hence in practice, these airborne techniques are mainly used for detailed studies of known coal fire areas which have been found by either satellite-based or field-based methods.

7.2.3 High Resolution Optical Satellite Data

Earth observation satellite imagery derived from Landsat TM, SPOT, and SOYUS satellites have been used to study coal fire areas. The six optical bands of Landsat TM with 30 meter resolution can, with suitable processing techniques, enhance the data to highlight the major areas of burnt caprock. The synoptic overview provided (180 \times 180 km) also greatly aids in studying the coal fields in their regional structural and tectonic settings. SPOT XS (three bands) at 20 meter spatial resolution has shown to be less useful than

TM, both in terms of area covered (only one tenth that of Landsat TM) and in the choice of spectral bands. SPOT Pan (10 meter spatial resolution), especially in stereomode is a useful tool. In addition, a Digital Elevation Model (DEM) can be produced, even for isolated areas of which there are no detailed maps, such as in many developing countries. The Russian SOYUS satellite images, provided in analog form, can be used in a similar way to color infrared aerial photographs with the added benefits of large area coverage and low cost. The spatial resolution is from 5 to 10 meters.

7.2.4 Satellite Thermal Infrared Data

There are currently four satellite systems with thermal infrared sensors onboard. The main data set used is the Landsat TM band 6 data which lies in the 10.4 to 12.5 μm region of the electromagnetic spectrum. Numerous authors have used this data source to detect underground coal fires (Bhattacharya et al. 1991, 1996; Mansor et al. 1994; Prakash et al. 1995a, 1995b; van Genderen et al. 1996; Wan & Zhang 1996a, 1996b). However, most authors have only used the daytime data acquired between 9.30 and 10.30 a.m. For the China coal fire research, the authors have also used multi-temporal night-time thermal infrared data from Landsat TM in addition to the daytime data, thus easing the removal of solar heating effects which occur in daytime imagery. Figure 7-2 is a night-time thermal infrared image taken by the Landsat TM satellite over the Kelazha coal fire area in northwest China on the 7th of April 1995. The red "hot spots" are the coal fires underground. However, as the spatial resolution of the thermal channel on Landsat TM is 120 m, very small or deep coal fires are often not detected. Next year the new Landsat 7 ETM (Enhanced Thematic Mapper) will be launched. The thermal sensor on this satellite will have a spatial resolution of 60 meters and should be able to detect much smaller coal fires than presently possible. The sixteen day repetitive cycle of Landsat makes this an ideal data source for routine monitoring of underground coal fires, both during day and night, and for checking the effectiveness of fire fighting and extinguishing activities being carried out. The Advanced Spaceborne Thermal Emission and Reflectance Radiometer (ASTER) due for launch in 1998 onboard EOS spans the 8-12 μm region with five contiguous bands (Kahle et al. 1996), thus enabling the possibility of multichannel split window thermometry at 90 m resolution.

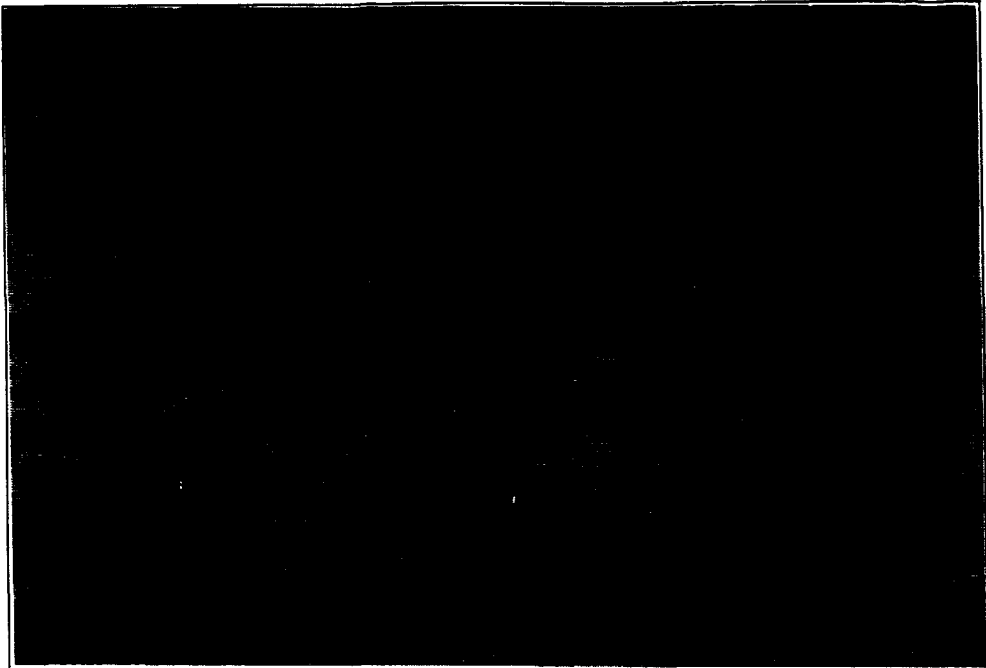


Figure 7-2. Night-time thermal infrared image acquired by the Landsat-TM over the Kelazha anticline coal fire area in Xinjiang region on 07/04/1995. The image has been color coded and density sliced. The areas in bright red indicate the location of underground coal fires.

In addition to Landsat, there are three other satellites acquiring data in the thermal wavelength bands. One is the NOAA-AVHRR (Advanced Very High Resolution Radiometer) which has several spectral bands in the thermal infrared region, e. g. channel 3 (3.55 to 3.93 μm), channel 4 (10.3 to 11.3 μm), and channel 5 (11.5 to 12.5 μm on NOAA-7, 9, 11, 12, 14). The spatial resolution varies from 1.1 km at nadir up to 8 km at the border of the image. This data source has been extensively studied and used for forest fire detection and for biomass burning at national, continental, and even global scales, as the data is acquired globally on a daily basis with both daytime and night-time data acquisition (Kaufman, et al., 1992; Kennedy, et al., 1994). The only published research to detect underground coal fires using NOAA-AVHRR data has been carried out by Mansor et al. (1994). They reported the potential capability of the AVHRR band 3 data to detect the subsurface coal fires in the Jharia coal field in India. They proposed that the good thermal contrast between the coal fire area and its surroundings in the night-time data leads to detection. The coal fires did not reveal any

significantly higher thermal anomalies in the other thermal bands of AVHRR (channel 4 and 5). They used a simple density slicing method to distinguish the coal fire areas. The size of the coal fire area detected was not mentioned in their paper. Our research on the use of NOAA-AVHRR thermal data for detecting underground coal fires in northern China provided no positive or reliable results to date.

The third satellite data source used for thermal anomaly detection was from the ATSR (Along Track Scanning Radiometer) sensor on board the ESA ERS-1 satellite. This operates in the thermal infrared wavelength centered at 11 and 12 μm (also at 3.7 μm in night-time mode) and has a spatial resolution of approximately one kilometer. To date the results for the test sites in China have been disappointing using the single-source processing and interpretation approach.

Another satellite system with a thermal sensor currently in orbit is the Russian RESURS-1, which has a spatial resolution half-way between Landsat and the other two systems mentioned above, namely 600 meters. Although an order for multitemporal data coverage of the China coal fire test area was placed in June 1996, no data have yet been received. Hence no evaluation as to its usefulness can be made as yet mentioned above, namely 600 meters. Although an order for multitemporal data coverage of the China coal fire test area was placed in June 1996, no data have yet been received. Hence no evaluation as to its usefulness can be made as yet.

7.2.5 Satellite Based Microwave Data

The European Space Agency's ERS-1 and ERS-2 satellites have on board a Synthetic Aperture Radar (SAR) sensor operating in the C band with a spatial resolution of approximately 25 meters. These two satellites were flown in a so-called "Tandem" model with one-day interval between data acquisitions. By using SAR interferometric techniques, a Digital Elevation Model (DEM) can be produced, and using differential interferometry, very small vertical land subsidence movements (in the order of centimeters) can be accurately measured. For a description of the concepts and applications of SAR Interferometry, see the paper by Gens and van Genderen 1996. As principal investigators to ESA, the authors have just acquired some imagery of the coal fire area in the Helanshan Mountains of Northern Ningxia Hui

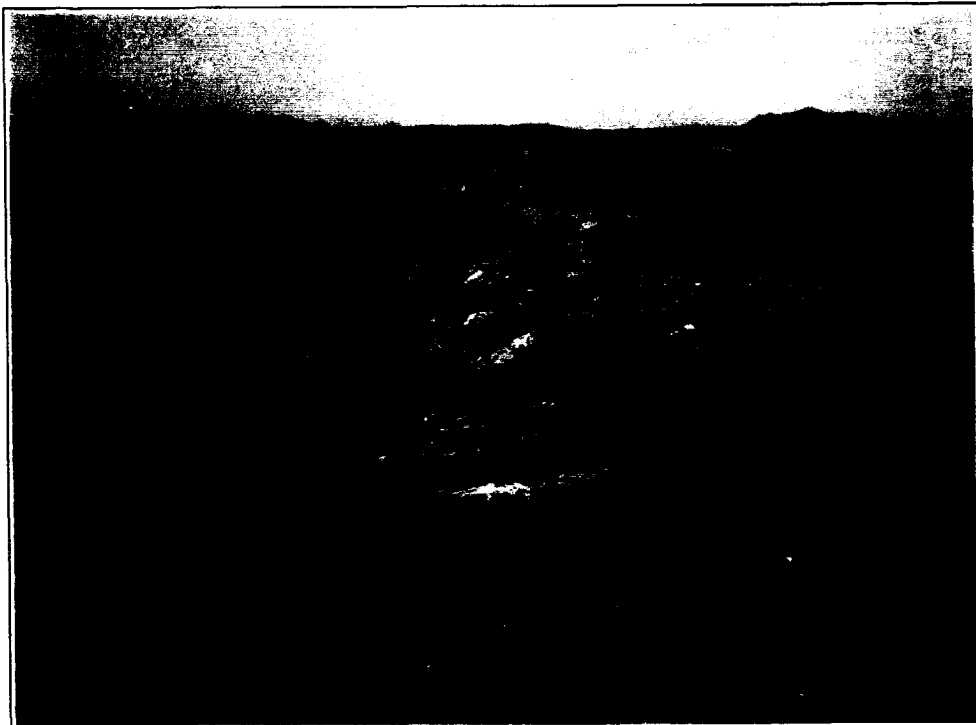


Figure 7-3a: Land subsidence occurring as a result of underground coal fires. The cracks are typically 20 centimeters to several meters wide, up to hundreds of meters long, and 10-20 meters in depth. The process is illustrated in figure 7-3b.

Autonomous region. These will be used to quantify land subsidence movements over the coming period. Figure 7-3a shows the land subsidence occurring in a coal fire area and Figure 7-3b describes the concept in diagram form.

7.3 Multi-sensor Data Fusion

Although the above section on single-sensor detection of coal fires has shown that many individual remote sensing systems provide some useful data for detecting underground coal fires, each data type only provides partial detection capability, and often only under certain circumstances. Hence, in order to develop a robust, reliable, and cost efficient methodology for operational use, a multi-sensor data fusion approach is required. It is the

objective of multi-sensor data fusion to integrate complimentary information in order to obtain more information than can be derived from single sensor data alone. There are three levels of fusion, namely pixel, feature, and decision based. Image fusion can be defined as “the combination of two or more different images to form a new image by using a certain algorithm” (van Genderen & Pohl, 1994; van Genderen, et al. 1994). Data or information fusion is a process whereby features are extracted and classified from both imaging and non-imaging data sources using probability theory to reinforce a common unambiguous interpretation of the features of interest, such as underground coal fires.

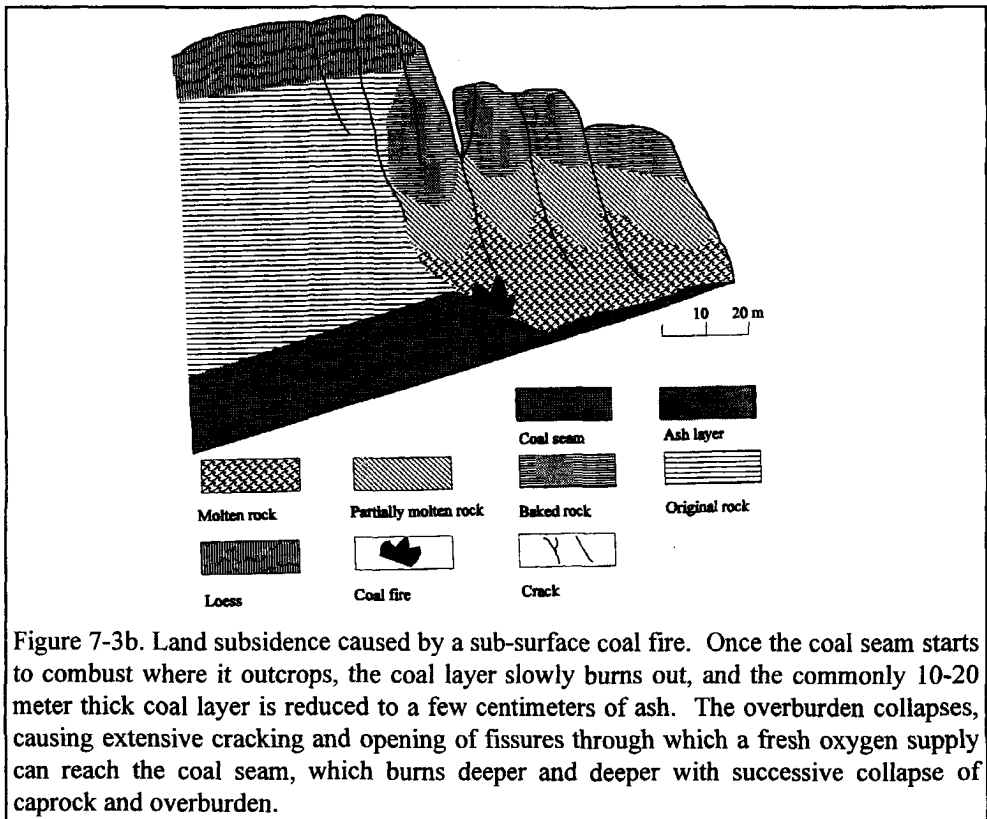


Figure 7-3b. Land subsidence caused by a sub-surface coal fire. Once the coal seam starts to combust where it outcrops, the coal layer slowly burns out, and the commonly 10-20 meter thick coal layer is reduced to a few centimeters of ash. The overburden collapses, causing extensive cracking and opening of fissures through which a fresh oxygen supply can reach the coal seam, which burns deeper and deeper with successive collapse of caprock and overburden.

These concepts are explained schematically in Figures 7-4, 7-5, and 7-6. The simplest case is depicted in Figure 7-4, where one can combine

different images to produce a new one, on which the underground coal fires are more reliably and easily detected.

7.3.1 Pixel-based data fusion

An example is given in Figure 7-7a, where band 3 of a SPOT XS multispectral optical image, band 5, and band 6 of Landsat TM have been combined to form this new image on which the location of the coal fire areas is clearly identifiable. Of course, by using this pixel-based fusion approach, each individual image must be accurately geometrically corrected so that the two images co-register to sub-pixel accuracy. Parameters such as pixel size, orbit inclination, etc. must be corrected for prior to fusion. In the case of the image displayed in Figure 7-7a, band 6 of Landsat TM and band 3 of SPOT were resampled to 30 meters. The color composite image then is generated by assigning red, green, and blue to TM band 6, TM band 5, and SPOT band 3, respectively. The resulting image (Figure 7-7a) clearly depicts the burnt rock areas (yellowish-green belt in the middle of the image) as well as the coal fire areas (the red spots).

7.3.2 Feature-based data fusion

Figures 7-8a and 7-8b show other examples of feature-based fusion as input to an overall Multi-Sensor Data Fusion System. Figure 7-8a is a combination of a color infrared photograph digitalized by a scanner and a thermal infrared image. In the color infrared photograph shown in Figure 7-1, the cracks and the burnt rocks (yellow colors in the image) caused by the underground coal fires are clearly visible. In the thermal infrared image only the thermal anomalies of the active coal fires are detectable. The two images were first geocoded, then the thermal infrared image was resampled to match the scanned photograph. The areas with a pixel value larger than 200 in the thermal infrared image were taken as fire areas. To minimize the confusion of the detailed terrain features in Figure 7-1, the areas except the "features" of thermal anomalies in the thermal infrared image were excluded for the fusion. Only the "features" of active coal fires are fused to the color infrared photograph. Considering the relationship between the thermal anomalies, burnt rocks, and the cracks, the spreading direction of the underground coal fires can then be derived. By integrating information from the DEM with the position of the outcrop of the burning coal seam

(taken from the image), the depth of the coal fires can be estimated by using the Dip-Angle model (Saraf, et al., 1995, Cassells and Genderen, 1995, Peng, et al., 1997).

It is suggested by one of our authors to use the differences in the color of the burnt rocks on the color infrared photographs to distinguish the burnt rocks caused by the active coal fires and by paleo fires. The burnt rocks caused by paleo coal fires are normally deep yellow and those related to the active coal fires are light yellow. This is because light-colored minerals such as sulphur and salmiac are easily weathered. In Figure 7-8a, the paleo coal fire at Louzhuangzi (Zhang, et al., 1998c) at the top center of the image (deep yellow in color) can easily be distinguished from the active coal fires associated with thermal anomalies.

7.3.3 Decision-based data fusion

Figure 7-8b has been made use of the airborne night-time thermal infrared data from which all subsurface coal fires have been extracted by the setting of a threshold, marking them in red, and subsequently draping the results over the DEM to produce the image. Now the interpreter can study the influence of the slope, aspect, altitude, and relief on the occurrence and distribution of underground coal fires; this is an important aspect for coal fire prevention and subsequent monitoring systems.

By using fusion techniques, the thermal anomalies derived from the multispectral and multi-temporal data can be combined. The spatial characteristics of the thermal anomalies and the underground coal fire spreading direction can then be analyzed (Zhang et al. 1997b).

In our case, we used the pixel based fusion approach to enhance the burnt rock and active coal fire areas. If the coal fire features were detectable, the feature based fusion approach was taken to analyze the spatial relationship of the direct and indirect indicators of the coal fires. Decision based fusion makes it possible to analyze the spatial characteristics of the coal fires of different intensity. One of the drawbacks of pixel-based fusion is the increase in noise of the background area. Comparing Figure 7-7a and Figure 7-7b, the fused image of Figure 7-7a is less detailed in the background terrain areas.

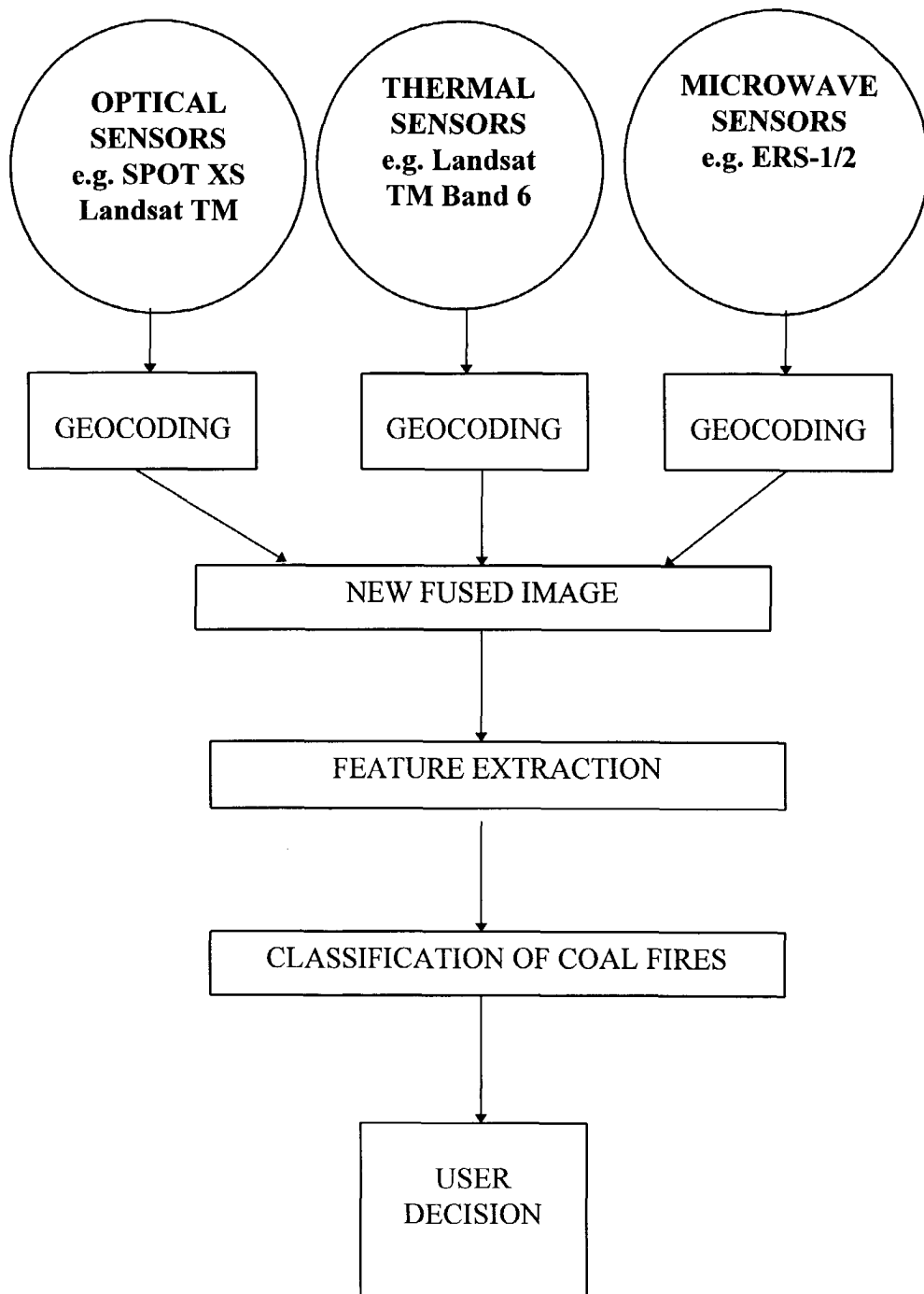


Figure 7-4. Pixel-based image fusion for detection of underground coal fires.

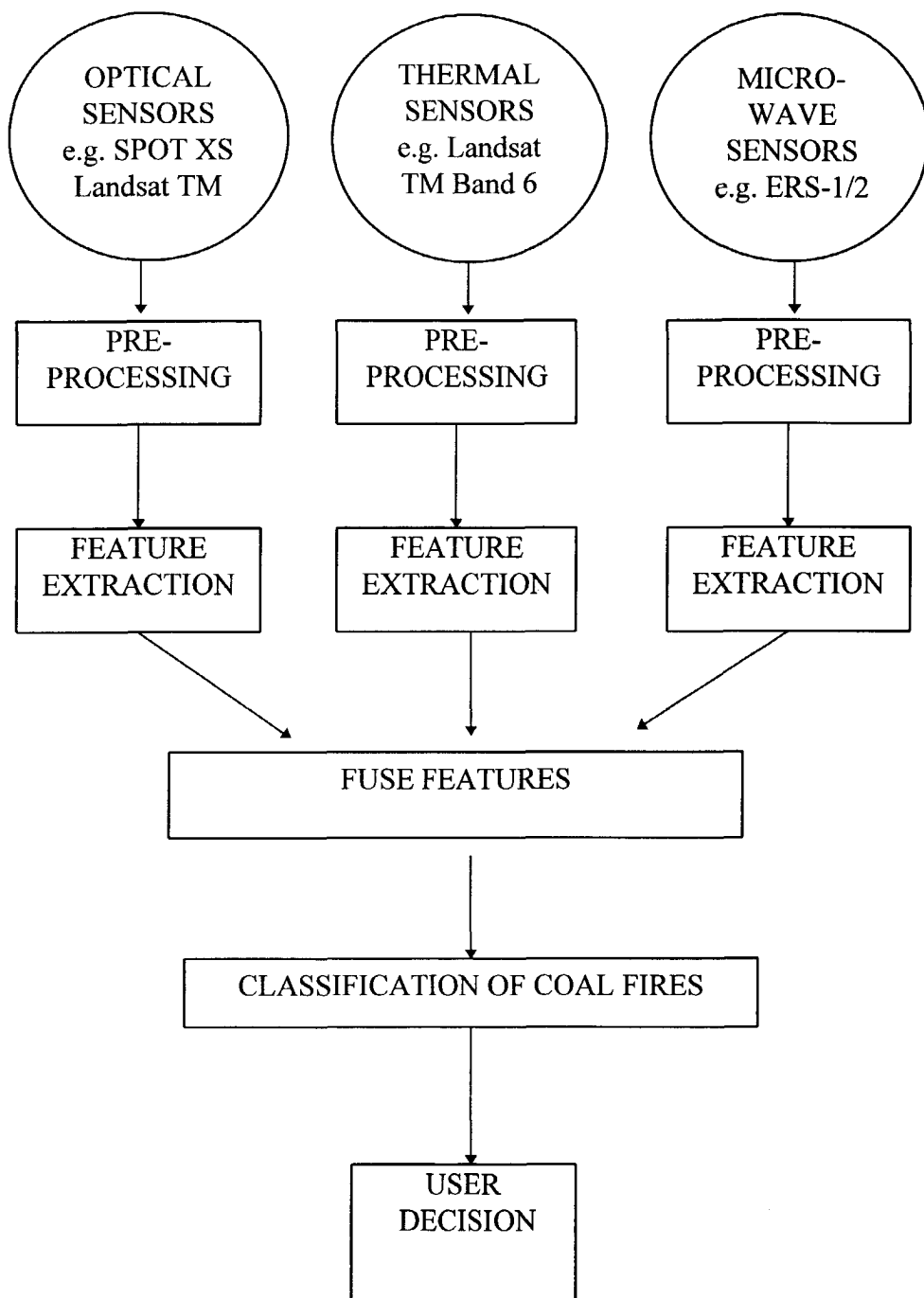


Figure 7-5. Feature-based data fusion for detection of underground coal fires.

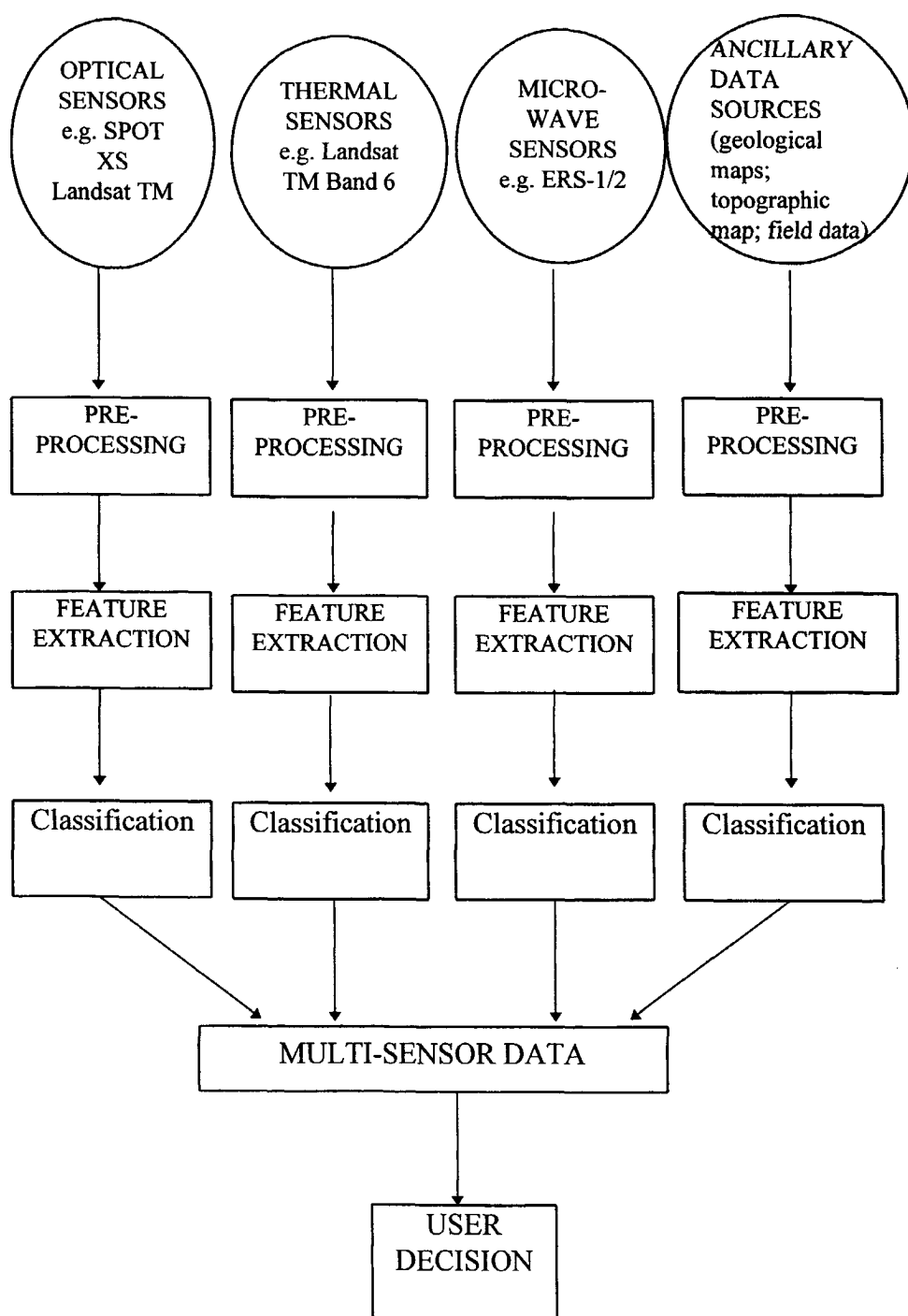


Figure 7-6. Decision-based information fusion for detection of underground coal fires.

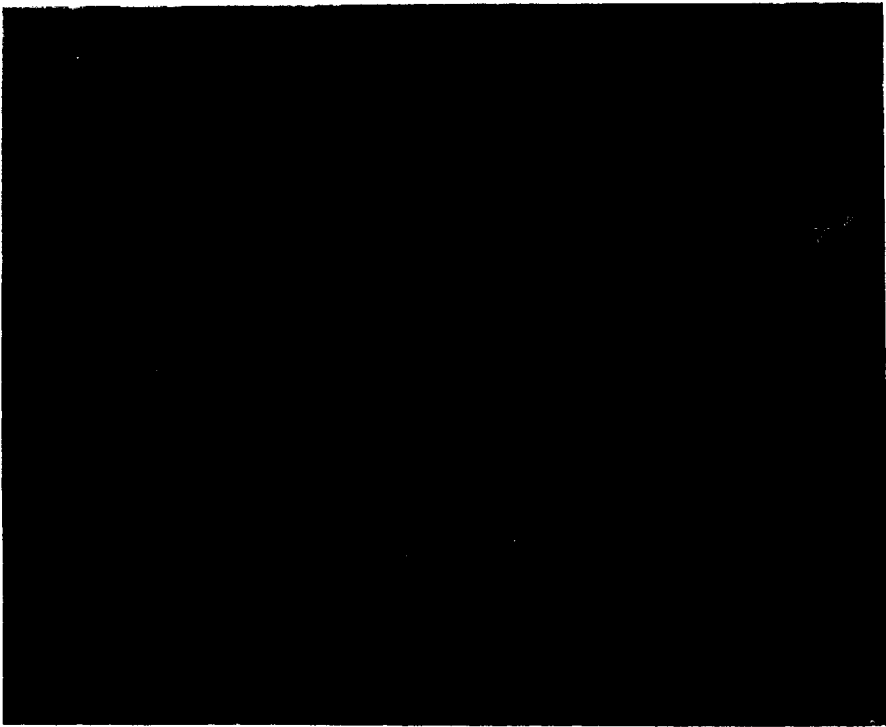


Figure 7-7a. Fused optical-thermal image of an underground coal fire in northwest China. Note that the image highlights the underground fire areas while maintaining the excellent spatial structural details inherent in the optical data.

Thus, by using the techniques and approaches described in Figures 7-4 to 7-6, an overall integrated Multi-Sensor Data Fusion System is developed. This is explained in diagrammatic form in Figure 7-10 that shows a three level fusion system. The first level uses the very inexpensive NOAA-AVHRR data which provides daily global coverage together with data from the VEGETATION sensor on-board SPOT-4 (from 1998) and from the thermal channel of ERS-1 ATSR. Data from the RESURS-1 satellite's thermal channel with a spatial resolution of 600 m will also be used once available. From these sources a weekly or monthly analysis of new hot spots or areas of burnt rock can be obtained. By overlaying this on a coal geological map of the area all "false alarms" can be filtered out (e. g hot spots not occurring near coal bearing areas). Then, at the second level of detail, the medium resolution Landsat TM daytime and night-time optical

and thermal infrared data are used to more accurately confirm the coal fires detected in level 1 and to delineate and measure their size and extent. Other data sources for the second level in the near future are from ETM+ and ASTER. The Enhanced Thermal Mapper (ETM+) on board Landsat-7 due for launch in 1998 will offer a 60 m spatial resolution thermal band and improved radiometric calibration. The Advanced Spaceborne Thermal Emission and Reflectance Radiometer (ASTER), which will be launched in 1998, spans the 8-12 μm region with five contiguous bands (Kahle et al. 1996) enabling the possibility of multi-channel split window thermometry at 90 m resolution. In addition to the thermal infrared coverage, ASTER offers three visible and near infrared channels (0.52-0.60, 0.63-0.69, 0.76-0.86) at 15 m resolution and six short wavelength infrared channels (1.6-1.7, 2.145-2.185, 2.185-2.225, 2.235-2.285, 2.295-2.365, and 2.36-2.430 μm) at 30 m resolution. At the third level of data and information fusion, detailed airborne surveys using color infrared and thermal infrared (daytime and

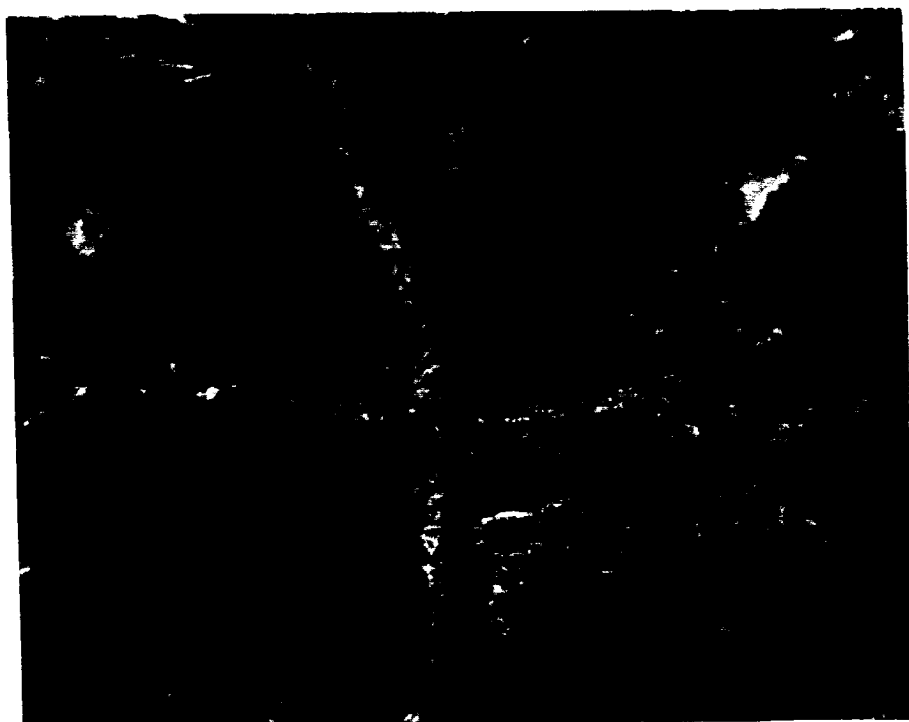


Figure 7-7b. Color composite SPOT band 3, 2, 1 with Red, Green and Blue.



Figure 7-8a. Feature-based image fusion for the detection of the coal fires with respect to the thermal anomalies from the thermal infrared image and the cracks from the color infrared photograph.

night-time imagery) data, together with ancillary data such as DEM'S, field measurements, and land subsidence measurements from INSAR etc., are used to make an overall classification of the size, depth, and direction of the coal fires. All these data and information are put into in a GIS for use in the operational monitoring system.



Figure 7-8b. Airborne thermal infrared image data draped over and co-registered with the DEM to create a 3-D perspective view. Such products assist in the study of underground coal fires as they show precisely the influence of slope, aspect, altitude, etc. on the distribution of the coal fires. This particular view is looking in an east-Northeast direction.

On the basis of this information system, fire-fighting plans can be drawn up together with a fire prevention plan, as today, most local coal fires are caused by mining activities and not only by natural spontaneous combustion. The whole system can then be used in a multi-temporal mode by regular updating of the remote sensing inputs.

7.4 Conclusions

An increasing number of earth observation satellites provide data for detecting underground coal fires, each covering a different portion of the electromagnetic spectrum at different spatial, temporal, and spectral resolutions. For the full exploitation of such increasingly sophisticated multi-source data, advanced analytical or mathematical data fusion techniques need to be developed. As each individual data source only provides part of the information required for decision making, the types of pixel, feature, and decision level fusion techniques discussed in this paper can contribute greatly to the detection of underground coal fires. The main benefits and results obtained so far are explained in Table 7-1. Using the

Multi-Sensor Data Fusion approach described in this paper for the detection of underground coal fires is expected to result in an improved system reliability. As the multiple satellites and sensors used for the detection of underground coal fires have a certain inherent redundancy, it will be less critical in the future if one satellite or sensor were to fail. This will simplify the investments that the Chinese Ministry of Coal Industry needs to make in order to set up an operational coal fire detecting, measuring, monitoring, and extinguishing system.

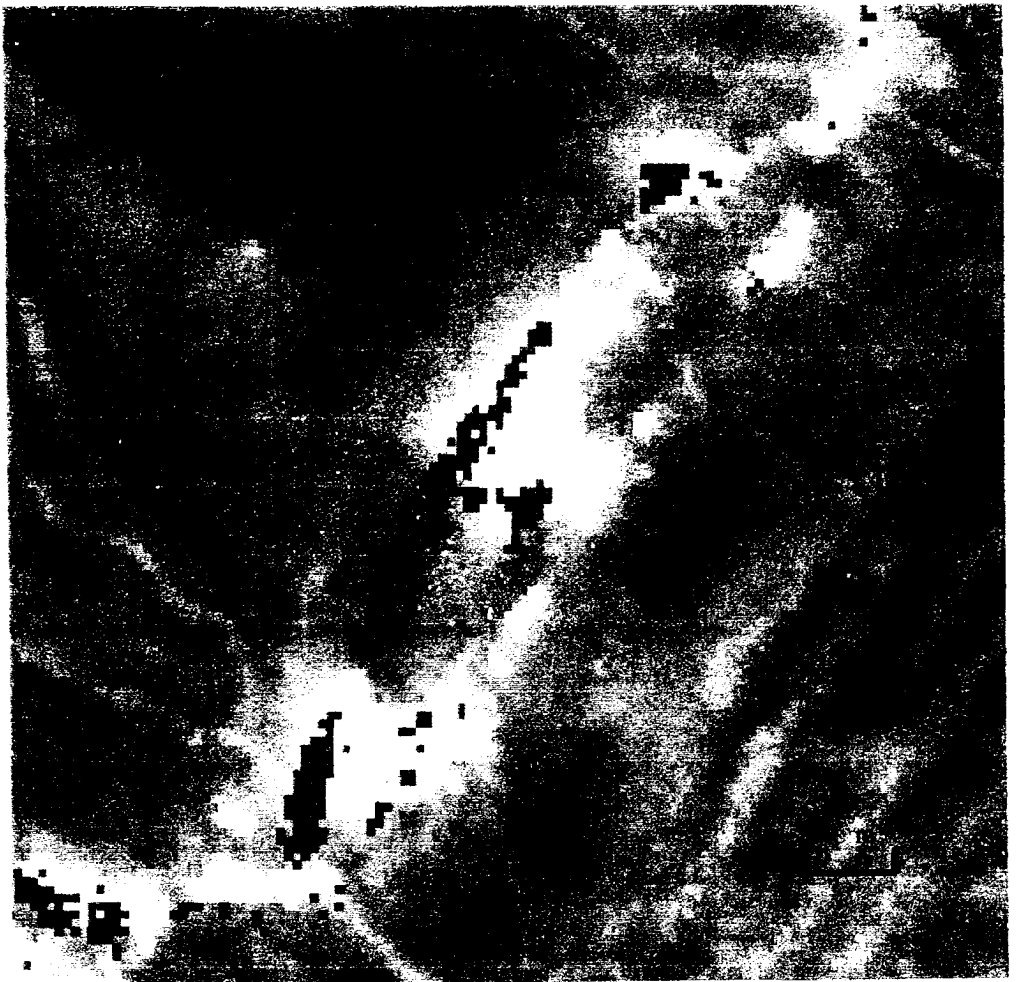


Figure 7-9. Decision-based image fusion for the detection of different intensive coal fires. The red areas represent the most intensive coal fire areas which are derived from the 3-5 μm data. The green areas represent the mid-amplitude coal fire areas derived from the day-time thermal infrared data of 8-12.5 μm . The white areas are the low-amplitude coal fires derived from the night-time thermal infrared data of 8-12.5 μm data. The blue areas are the intensively solar heated areas.

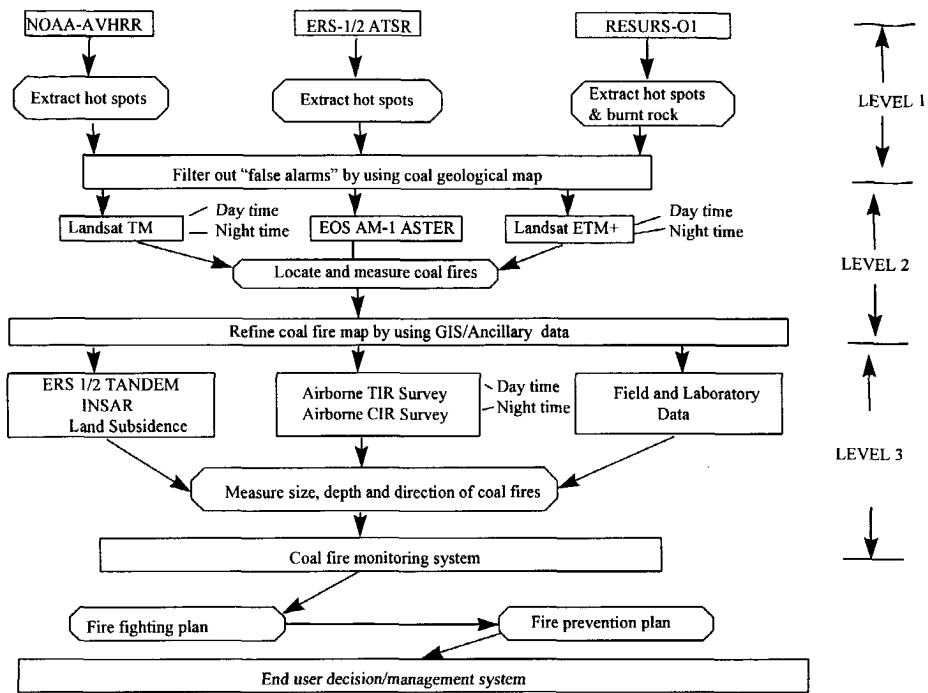


Figure 7-10. A three-level Multi-Sensor Data Fusion System developed by ITC to study location, size, depth, etc. of underground coal fires for monitoring and management purposes.

Table 7-1 Table showing the result and benefits of multi-sensor data fusion for the detection of underground coal fires.

Results	General Advantages	Operational Benefits
<ul style="list-style-type: none"> • Robust operational performance 	one sensor can continue to contribute information, while others are unavailable or lack coverage of the coal fire areas	<ul style="list-style-type: none"> - allows continued operation - increases possibility of detecting coal fires
<ul style="list-style-type: none"> • Enhanced spatial resolution 	pixel fusing low and high resolution data can "sharpen" images	<ul style="list-style-type: none"> - aids interpretation and detection of fire areas
<ul style="list-style-type: none"> • Enhanced temporal coverage 	by using multiple satellites, the time between image acquisitions is reduced. Enhances likelihood that an image is acquired under ideal conditions	<ul style="list-style-type: none"> - day/night, all weather capability - increased possibility of underground coal fire detection
<ul style="list-style-type: none"> • Enhanced spectral coverage 	combining optical, thermal, and microwave sensors increases chance of detecting coal fires. Also less vulnerable to atmospheric/weather/day-night effects	<ul style="list-style-type: none"> - increases classification accuracy - allows continuous operation
<ul style="list-style-type: none"> • Increased confidence 	each sensor type and image sources helps confirm detection of underground coal fires; reduces number of false alarms	<ul style="list-style-type: none"> - increased classification accuracy
<ul style="list-style-type: none"> • Improved detection 	multisensor data fusion increases the chances of the underground coal fires being detected	<ul style="list-style-type: none"> - more reliable classification - higher accuracy
<ul style="list-style-type: none"> • Reduced Ambiguity 	joint information from multiple data sources reduces the number of alternative hypothesis about whether a feature is really a coal fire or not	<ul style="list-style-type: none"> - faster decision making - increased reliability of the results

REFERENCES

- Anuta, P. E., 1976, Digital registration of topographic data and satellite MSS data for augmented spectral analysis, *Proceeding of the 42nd convention of the American Society of Photogrammetry*, pp. 180-87.
- ARSC, 1989, Delineation of the burnt rock in Xinmin area, Shenfu coal field, China. *Internal Report*, p.25 (In Chinese).
- ARSC, 1993, Report on investigation of coal fires in Northwest of China, *Internal Report* 56 p. (in Chinese).
- Banerjee, S.C., 1985, Spontaneous combustion of coal and mine fires, A. A. Balekema, Rotterdam, p. 18.
- Bartolucci, L. A. Chang M., Anuta P. E. and Graves M. R., 1988, Atmospheric effects on Landsat TM thermal infrared data. *IEEE Transactions on Geosciences and Remote Sensing*, 26(2), 425-435.
- Bhattacharya, A. and Reddy, S., 1994, Underground and surface coal mine fire detection in India's Jharia coal field using airborne thermal infrared data. *Asian-Pacific Remote Sensing Journal*, Vol.7, No.1, 59-73.
- Bhattacharya, A., Reddy, S. and Mukherjee, T., 1991, Multi-tier remote sensing data analysis for coal fire mapping in Jharia coalfield of Bihar, India. *Asian Conference on Remote Sensing, Singapore*, Vol. I, pp. P-22-1 to P-22-6.
- Bhattacharya, A., Reddy, C.S.S. and Manoj Dangwal, 1996, Coal mine fire inventory and monitoring in Jharia coalfield, Bihar, India, using thematic mapper thermal IR data. *Proceedings of the Eleventh Thematic Conference and Workshops on Applied Geologic Remote Sensing*, Las Vegas, USA, 27-29 February 1996.
- Bo, M., 1981a, Study on Quaternary system in Xinjiang, *Collection of Papers on Quaternary and Glacial Geology in Xinjiang*, 159-162 (in Chinese).
- Bo, M., 1981b, Study on the Characteristics of neotectonic movements in Xinjiang, *Collection of Papers on Quaternary and Glacial Geology in Xinjiang* pp. 223-225 (in Chinese)
- Boll, J., Thewessen, T. J. W., Meijer E. L and. Kroonenberg S. B., 1988, A simulation of the development of river terraces. *Z. Geomorphologie* 32: 31-45.
- Borland, 1994, *Borland C++*, version 4.0.

- BRSC, 1993, Report on investigation of coal fires in North China, *Internal Report*, 49 p. (in Chinese).
- Bustin, R. M. and Mathews, W. H., 1982, In situ gasification of coal, a natural example: history, petrology, and mechanics of combustion, *Canadian Journal of Earth Sciences*. vol. 19, p. 514-523.
- Bustin, R. M. and Mathews, W. H., 1985, In situ gasification of coal, a natural example: additional data on the Aldridge Creek coal fire, South-eastern British Columbia, *Canadian Journal of Earth Sciences*. vol. 22, p1858-1864.
- Bureau of Geology and Mineral Resource of Xinjiang-Uygur Autonomous region, 1993, Regional Geology of Xinjiang Uygur Autonomous Region, *Geol. Mem Series I*, Number 32, pp. 783-841 (in Chinese).
- Callison, R. D. and A. P. Cracknell, 1984, Atmospheric correction to AVHRR brightness temperatures for waters around Great Britain, *International Journal of Remote Sensing*, vol. 5, No. 1, pp. 185-198.
- Carroll, A. R., Graham, S. A., Hendrix, M. S., Ying, D. and. Zhou, D., 1995, Late Paleozoic tectonic amalgamation of northwestern China: sedimentary record of the northern Tarim, northwest Turpan and southern Junggar basin. *Bull. Geol. Soc., Amer.* 107: 571-594.
- Cassells, C. J. S., Genderen, J. L. van., 1995, Thermal modelling of underground coal fires in Northern China. *Remote Sensing in Action, Proceedings of the 21st Annual Conference of The Remote Sensing Society*, 11-14 September, 1995, Southampton. Remote Sensing Society, pp. 544-551.
- Cassells, C. J. S., Genderen, J. L. van and Zhang X. M., 1996, Detection and measuring underground coal fires by remote sensing - *Proc. 8th Australasian Remote Sensing Conference*, Canberra, March, 1996: vol 2, 90-101.
- Chen, W., 1992, Digital image processing application for coal fire remote sensing investigation, *Remote Sensing for Land & Resources*, vol 12, no 2. pp 21-24 (in Chinese).
- Chuvieco, E. and Martin, M. P., 1994, Global fire mapping and fire danger estimation using AVHRR images, *Photogrammetric Engineering & Remote Sensing*, vol 60, no 5, 563-570.
- Crippen, R. E., 1989, A simple spatial filtering technique for the Cosmetic removal of scan line noise from Landsat TM p-type imagery, *Photogrammetric Engineering & Remote Sensing*, vol. 55 no. 3, pp. 327-331.

References

- CSIRO and MPA (Australia), 1992, *The MicroBRIAN resource manuals*, version 3.
- Dave, J. V. and Bernstein R., 1982, Effect of terrain orientation and solar position on satellite-level luminance observations. *Remote Sensing of Environment*, 12, pp. 331-348.
- De Boer, C. B., Van Hoof, A. A. M., Zhang X. M., Kroonenberg S. B., Dekkers M. J., 1997, Native iron in baked sediments due to spontaneous underground combustion of coal seams. ESG Congress, Vienna, *Annales Geophysicae*, 1997, Suppl. I to Vol 15, C111.
- Dozier, J., 1981, A method for satellite identification of surface temperature fields of subpixel resolution. *Remote Sensing Environment*, 11, pp. 221-229.
- Ellyett, C. D. and Fleming, A. W., 1974, Thermal infrared imagery of the burning mountain coal fire. *Remote Sensing of Environment*, Vol.3, No.1, PP.79-86.
- ERDAS, 1988, *ERDAS user's guide*, version 7.3, release 21 October. American Elsevier Publishing Company, Inc..
- Fan, W. T., 1997, Coal Geology Newspaper, 2 July 1997, No. 559, p1. (in Chinese)
- Feng, F., 1990, Boundary identification for burnt coal seams in Xinmin spontaneous combustion district of Shenfu coalfield, Shaanxi, *Proceeding of 11th Asian Conference on Remote Sensing*, Nov.15-21,1990, Guangzhou, China.
- Fisher, W. J and Knuth W. M., 1968, Detection and delineation of subsurface coal fires by aerial infrared scanning, *Geol. Soc. America Special Paper* 115, pp. 67-68.
- Genderen, J. L. van , Cassells, C. J. S. , and Zhang, X. M., 1996, The synergistic use of remotely sensed data for the detection of underground coal fires - *International Archives of Photogrammetry and Remote Sensing*, vol. XXXI, part 7: 722-727.
- Genderen, J. L. van, Cracknell, A. P., Konecny, G., and Sieber, A., 1994, Synergy of remotely sensed data: A European scientific network in the field of remote sensing - *Proceedings of First ERS-1 Pilot Project Workshop*, Toledo, Spain, 22-24 June 1994, sp-365 (Paris: European Space Agency): 229-234.
- Genderen, J. L. van, and Pohl, C., 1994, Image fusion: issues, techniques and application. 'Intelligent image fusion' - *Proceedings EARSeL Workshop*, Strasbourg, France, 11 September 1994.

- Gens, R. and Genderen, J. L. van., 1996, SAR interferometry - issues, techniques, applications - *International Journal of Remote Sensing* 17 (10): 1803-1835.
- Greene, G. W., and Moxham, R. M., 1969, Aerial infrared surveys and borehole temperature measurements of coal mine fires in Pennsylvania - *Proceeding of the 6th ERIM Symposium on Remote Sensing of Environment*, University of Michigan, Oct.13-16: 517-525.
- Guan, H. Y., 1963, On the Yaojie burnt rocks, *Proceedings of Shaanxi Young Scientists Conference, China*: 212-226 (in Chinese).
- Guan, H. Y., 1984, The research of coal bed thermal IR radiation. *Proceedings of the Seminars on Remote Sensing for Geological Applications*, PP.535-547.
- Guan, H. Y., 1989, Applications of remote sensing techniques in coal geology, *Acta Geologica Sinica*, Vol. 2, No. 3: 254-269.
- Guan, H. Y., Genderen, J. L. van., and Schalke, H. J. W. G., 1996, Study and survey on the geological hazards of coal fire in North China. *Abstracts 30th International Geological Congress*, vol 1, 458.
- Holben, B. N., & Justice, C. O., 1979, Evaluation and modeling of the topographic effect on the spectral response from nadir pointing sensors. NASA TM 80305, Goddard Space Flight Center, Greenbelt, Maryland, USA.
- Holben, B. N., & Justice, C. O., 1981, An examination of spectral band ratioing to reduce the topographic effect on remotely sensed data. *International Journal of Remote Sensing*, 2, 115.
- Hong, L., Qi, G. Y., Lu, S. A., Zhong, H., Qiao, L. Y., Wu, Z. A., 1989, Introduction to Quaternary Geology in Xinjiang, *Collection of Papers on Quaternary and Glacial Geology in Xinjiang*, pp. 36-58 (in Chinese).
- Huang, H. & Zhao, Z., 1981, Classification and characteristics of Quaternary in Xinjiang, *Collection of Papers on Quaternary and Glacial Geology in Xinjiang*, pp. 166-169 (in Chinese).
- Huang, Y. F., Huang, H., Chen, W., and Li, Y. X., 1991, Remote sensing approaches for underground coal fire detection. Presented at the *Beijing International Conference on Reducing of Geological Hazards*, PP.634-641.
- Hughes, P. A., McComb, T. J. L., Rimmer, A. B., Turver, K. E. and Rodgers, M. L. B., 1993, A mathematical model for the prediction of

- temperature of man-made and natural surfaces. *International Journal of Remote Sensing*, Vol.14, No.7, PP.1383-1412.
- ITC, 1993a, *ILWIS 1.4 user' manual*, first edition.
- ITC, 1993b, *ILWIS 1.4 tutorial*.
- ITC, 1992, *Urban ILWIS workshop manual*.
- Justice, C. O., Wharton S. W., and Holben, B. N., 1981, Application of digital terrain data to quantify and reduce the topographic effect on Landsat data, *International Journal of Remote Sensing*, vol. 2, no. 3, 213-230.
- Kahle, A.B., Palluconi, F. D., Hook, S. J., Realmuto, V. J. and Bothwell, G., 1991, The Advanced Spaceborne Thermal Emission and Reflectance Radiometer (ASTER). *International Journal of Imaging Systems Technology*, 3, 144-156.
- Kang, G., 1991, Study on the application of techniques of aerial remote sensing to Shenfu coal field of Jurassic system, *Proceeding of the Eighth Conference on Geologic Remote Sensing*, Denver, Colorado, USA, April 29-May 2, 1991 pp. 719-727.
- Kang, G. F., Zhang, Q. S. and Lei, X. W., 1993, Coal fire investigation report of northern part of China (Northwest Area), *ARSC internal report*, Xian, China, 93 p. (in Chinese).
- Kaufman Y. J., Setzer A., Ward D. Taner D., Holban B.N., Menzel P., Pereira M. C. and Rasmussen, R. 1992 Biomass burning airborne and spaceborne experiment in the amazons (base-a) - *Journal of Geophysical Research*, 97:14581-14599.
- Kawata, Y., Ueno, Sueo and Kusaka, Takashi., 1988, Radiometric corrections for atmospheric and topographic effects on Landsat MSS images. *International Journal of Remote Sensing*, Vol.9, No.4, pp.729-748.
- Kennedy, P. J., Belward A. S. and Gregoire, J. M., 1994, An improved approach to fire monitoring in west Africa using AVHRR data - *International Journal of Remote Sensing*, 15(11): 2235-2255.
- Knuth, W. M., Fisher, W. Jr. and Stingelin, R.W., 1968, Detection, delineation and monitoring of subsurface coal fires by aerial infrared scanning. *Geographer HRB-Singer, Inc., A Subsidiary of the Singer Company*, State College, Pennsylvania, pp. 877-881.
- Li, D. X., 1985, Applied study of airborne remote sensing in Taiyuan coalfield, China, *Internal Report*, Remote Sensing Centre of Ministry of Coal Industry, Xi'an, China, pp 3-10 (in Chinese).

- Lillesand, T. M., and Kiefer, R. W., 1994, *Remote sensing and image interpretation*, John Wiley & Sons Inc.
- Liu, J. G., and Moore, J. M., 1997, Simulated higher spatial resolution Landsat thermal image, *Proceeding of the Twelfth International Conference and Workshop on Applied Geologic Remote Sensing*, Denver, Colorado, 17-19, November 1997, vol I, pp182-189.
- Lourens, L. J., Antoarakou, A., Hilgen, F. J., Van Hoof, A. A. M., Vergnaud-Grazzini, C. and Zachariasse, W.J., 1996, Evaluation of the Plio-Pleistocene astronomical time scale. *Paleoceanography* 11: 391-413.
- Mansor, S. B., Cracknell, A. P., Shilin, B. V. and Gornyi, V. I., 1994, Monitoring of underground coal fires using thermal infrared data. *International Journal of Remote Sensing*, 15(8), pp. 1675-1685.
- Marc, P. Stoll., 1994, Potential of remote sensing in the thermal band for global change. NATO ASI Series, Vol. I24, *Remote Sensing and Global Climate Change*, Edited by Robin A.Vaughan and Arthur P. Cracknell, pp.393-404.
- Markham, B. L., 1985, The Landsat sensor's spatial responses. *I.E.E.E. Transaction on geoscience and Remote Sensing*, 23, 864-875.
- Markham, B. L. and Barker, J. L., 1986, Landsat MSS and TM post-calibration dynamic ranges exoatmospheric reflectance and at-Satellite temperatures. *EOSAT Landsat Tech. Notes(Aug.)*, pp. 3-8.
- Matson, M., Dozier, J., 1981, Identification of subresolution high temperature sources using a thermal infrared sensor. *Photogrammetric Engineering and Remote Sensing*, 47(9), pp. 1311-1318.
- Microsoft., 1994, *Visual C++*, version 1.0.
- Molnar, P., Brown, E. T., Burchfiel, B. C, Deng, Q. D., Feng, X. Y, Li, J., Raisbeck, G. M., Shi, J. B., Wu, Z. M., Yiou, F. and You, H. C., 1994, Quaternary climate change and the formation of river terraces across growing anticlines on the North Flank of the Tien Shan, China. *American Journal of Geology*, 102:583-602.
- Mukherjee, T., Bandyopadhyay, T. K. and Pande, S. K., 1991, Detection and delineation of depth of subsurface coalmine fires based on an airborne multispectral scanner survey in a part of the Jharia Coalfield, India. *Photogrammetric Engineering & Remote Sensing*, 57(9), pp. 1203-1207.

- Muirhead, K., and Cracknell, A. P., 1984, Identification of gas flares in the North Sea using satellite data, *International Journal of Remote Sensing*, Vol. 5, No.1, 199-212.
- Muirhead, K., and Cracknell, A. P., 1985, Straw burning over Great Britain detected by AVHRR, *International Journal of Remote Sensing*, 1985, Vol. 6, No.5, 827-833.
- Nilsson, T., 1983, *The Pleistocene*. Reidel, Dordrecht, 651 pp.
- Oppenheimer, C., Rothery, D. A., Pieri, D. C., Abrams, M. J. and Carrere, V., 1993, Analysis of airborne visible/infrared spectrometer (AVIRIS) data of volcanic hot spots. *International Journal of Remote Sensing*, Vol.14, No.16, pp. 2919-2934.
- Peng, W. X., Genderen, J. L. van, Kang, G. F., Guan, H. Y., Tan, Y. J., 1997, Intergrated modeling for estimating the depth of underground coal fires, *TERRA NOVA the European Journal of Geosciences* (in press).
- Peng, X. and Zhang, G., 1989, Tectonic features of the Junggar basin and their relation with oil and gas distribution. in: K.J. Hsü (ed.), *Chinese sedimentary basins*. Elsevier, 17-31.
- Prakash, A., Saraf, A. K., Gupta, R. P., Dutta, M. and Sundaram, R. M., 1995a, Surface thermal anomalies with underground fires in Jhahra coal mine, India. *International Journal of Remote Sensing*, 16(12), pp. 2105-2109.
- Prakash, A., Sastry, R. G. S., Gupta, R. P., Saraf, A. K., 1995b, Estimating the depth of burned hot feature from thermal I.R. remote sensing data, a conceptual approach. *International Journal of Remote Sensing*, 16(13), pp. 2503-2510.
- Prakash, A., Gupta, R. P. and Saraf, A. K., 1997, A Landsat TM based comparative study of surface and subsurface fires in the Jharia coalfield, India, *International Journal of Remote Sensing*, 1997, vol 18, no, 11, 2463-2469.
- Qiao, Z., 1981, Quaternary strata in Urumqi and Toutunhe river area, *Collection of Papers on Quaternary and Glacial Geology in Xinjiang*: pp. 176-183, (in Chinese).
- Ramlu. M. A., 1991, *Mine disasters and mine rescue*, A. A Balkema / Rotterdam.
- Reddy, C. S. S., Srivastav, S. K., and Bhattacharya, A., 1993, Application of thematic mapper short wavelength infrared data for the detection and monitoring of high temperature related geo-environmental

- features, *International Journal of Remote Sensing*, Vol 14: 3125-3132.
- Rees, W. G., 1990, *Physical Principles of Remote sensing*, Cambridge University Press.
- Ricotta, C., and Avena, G. C., 1997, The influence of meteorological conditions and topographic parameters on the beech forest microclimate of Simbruini Mountains, central Italy, *International Journal of Remote Sensing*, vol, 18, no. 3, 505-516.
- Robinson, J. M., 1991, Fire from space: Global fire evaluation using infrared remote sensing, *International Journal of Remote Sensing*, vol. 12, no. 12, 3-24.
- Rothery, D. A., Francis, P. W. and Wood, C. A., 1988, Volcano monitoring using short wavelength infrared data from satellites. *Journal of Geophysical Research*, 93, pp. 7993-8008.
- Rozema, A., Genderen, J. L. van and Schalke, H. J. W. G., 1993, Environmental monitoring of coal fires in north China. *Project Identification Mission Report*, BCRS 93-29, 24 pp.
- Rozema, A., A., --, Mathematical model formulation of the thermal behavior of bare soils, based on heat and moisture transfer, *NIWARS publication*, No. 11.
- Salisbury, J. W., and D'aria, D. M., 1992, Emissivity of terrestrial materials in 8-14 μm atmospheric window, *Remote Sensing of Environment*, 42, 83-106.
- Saraf, A. K., Gupta, R. P. and Anishkumar, 1992, Remote sensing technique in underground fire detection in coal mines of Jharia. *Proceedings of ICORG-92 on Remote Sensing Application & GIS: Recent Trends*.
- Saraf, A. K., Prakash, A., Sengupta, S., and Gupta, P., 1995, Landsat TM data for estimating ground temperature and depth of subsurface coal-fire in Jharia coalfield, India. *International Journal of Remote Sensing*, 16, 2111-2124.
- Schmal, D., 1987, A model for the spontaneous heating of stored coal, *Ph.D thesis*, Technology University of Delft, Delft, The Netherlands.
- Schneider, W., 1996, The coal-bearing Jurassic at the southern margin of the Junggar basin, Xinjiang. *Geowissenschaften* 14: 285-287.
- Schott, John R., 1989, Image processing of thermal infrared images. *Photogrammetric Engineering and Remote Sensing*, 55(9), pp. 1311-1321.

- Seitzer, A. W. and Verstraete, M. M., 1994, Fire and glint in AVHRR's channel 3: a possible reason for the non-saturation mystery, *International Journal of Remote Sensing*, vol 15, no.3, 711-718.
- Singh, S. M., 1984, Removal of atmospheric effects on a pixel by pixel basis from instruments on satellite, The Advanced Very High Resolution Radiometer(AVHRR). *International Journal of Remote Sensing*, 5, pp. 161-183.
- Singh, S. M., 1994, Effect of surface wind speed and sensor view zenith angle dependence of emissivity on SST retrieval from thermal infrared data, ATSR, *International Journal of Remote Sensing*, vol. 15, No. 13: 2,615-2,625.
- Slavecki, R. J., 1964, Detection and location of subsurface coal fire. *Proceedings of the Third Symposium on Remote Sensing of Environment*. Oct. 14-16, 1964, pp. 537-547, University of Michigan, Michigan.
- Sondreal, E. A. and Ellman, H. C., --, Laboratory determination of factors affecting storage of North Dakota Lignite, RI, 7887, US Bureau of Mines.
- Strahler, A. H., Logan, T. L., and Bryant, N. A., 1978, Improving forest cover classification accuracy from Landsat by incorporating topographic information, *Proceedings of the 12th International Symposium on remote sensing of the Environment*, vol., 2, Manila, Philippines, pp. 927-956.
- Strahler, A. H., Logan, T. L., and woodcock, C. E., 1979, Forest classification and inventory system using Landsat, digital terrain, and ground sample data, *Proceeding of the 13th International Symposium on Remote Sensing of the Environment*, vol. III, Ann Arbor, Michigan, U.S.A., pp. 1541-1555.
- Tyráček, J. 1994, Stratigraphical interpretation of the paleomagnetic measurements of the porcellanites of the Most basin, Czech Republic. *Vestník Českégeologického ústavu* 69, 2: 83-87.
- Veldkamp, A., 1992, A 3-D model of Quaternary terrace development, simulations of terrace stratigraphy and valley asymmetry: a case study in the Allier terraces (Limagne, France). *Earth Surface processes and Landforms*, 17: 487-500.
- Veldkamp, A. and Vermeulen, S. E. J. W., 1989, River terrace formation, modelling and 3-D graphical simulation. *Earth Surface Processes and Landforms*, 14: 641-654.

- Vinogradova, L. P., Surnatchev B. A. and Terpigorava, E. A., 1972, How gas in seams affects heating and susceptibility to spontaneous combustion, *Ugol* 1972, No. 9.
- Wan, Y. Q. and Zhang, X. M., 1996a, Using a DTM to reduce the effect of solar radiance on Landsat TM thermal IR images and detection coal fires, *Asian-pacific Remote Sensing and GIS Journal*, Volume 8, Number 2, pp. 65-72.
- Wan, Y. Q. and Zhang, X. M., 1996b, Using DTM to improve the accuracy of detecting coal fires with thermal infrared images, *Remote Sensing of Environment China*, vol. 11, no.4, pp 248-254, (in Chinese).
- Wan, Z. and Dozier, J., 1989, Land surface temperature measurement from space: physical principles and inverse modeling. *IEEE Transaction on Geoscience and Remote Sensing*, 27, pp.268-278.
- Watson, K., 1975, Geologic applications of thermal infrared images. *Proceedings I.E.E.E.*, 63, 128-137.
- Yang, K., Lu, J., Lin, K. Y., Lan, Y. C, Sun, J. B., 1988, *Principles and methodology of Remotely sensed images*, China mapping press, 526 pp. (in Chinese).
- Zhang, X. M., Cassells, C., and Genderen J. L. van, 1998a, Multi-sensor data fusion for the detection of underground coal fires, *Geologie & Mijnbouw*, Vol 77 (in press).
- Zhang, X. M., Genderen, J. L. van and Kroonenberg S. B., 1997, A method to evaluate the capability of Landsat-5 TM band 6 data for sub-pixel coal fire detection, *International Journal of Remote Sensing*, Vol. 18, No. 15, 3279-3288.
- Zhang, X. M., Genderen, J. L. van and Kroonenberg S. B., 1998b, Spatial analysis of thermal anomalies from airborne multi-spectral data, *International Journal of Remote Sensing*, (submitted).
- Zhang, X. M., Koopmans, B. N., and Wan, Y. Q., 1995, Detection of spontaneous combustion of coal in northern China, using thermal remote sensing data. *Proceedings of International Space Congress*, Bremen, Germany, May 23-25th, 1995, pp 2-10.
- Zhang, X. M., and Kroonenberg, S. B., 1996., Pleistocene coal fires in Xinjiang, northwest China. *Abstracts 30th International Geological Congress*, pp. 457.
- Zhang, X. M., Kroonenberg, S. B. and Boer, C. B. de., 1998c, Pleistocene coal fires in Xinjiang, Northwest China, *TERRA NOVA the European Journal of Geosciences*.(submitted).

References

- Zhang, Y. and Tang, X., 1994, Coal petrology application for liability of coal to spontaneous combustion, *Coal Geology and Exploration*, Vol 22, No 4, pp 21-24, (in Chinese).

References

CURRICULUM VITAE

Xiangmin Zhang was born on November 30, 1965 at Yuanshi, Hebei, P. R. China. He received a Bachelor of Engineering degree in Geology from the Hebei Institute of Geology, Xuanhua, Hebei, in 1986. From 1986 to 1989 he studied Structural Geology in Xi'an Institute of Geology, Xi'an, China and earned his degree of Master of Science in 1989. He worked at Aerophotogrammetry & Remote Sensing Bureau of China Coal (ARSC), Xi'an, China from 1989 to 1994 as an assistant Engineer and an Engineer. He started his Ph.D research at International Institute for Aerospace Survey and Earth Sciences (ITC), Enschede, the Netherlands in July 1994. He is the author and co-author of a number of scientific articles. He is married and has a son.

